NEUTRON SCATTERING AND QUANTITATIVE MODELING OF MAGNETIC EXCITATIONS IN FRUSTRATED MATERIALS

A Thesis Proposal
Presented to
The Academic Faculty

By

Xiaojian Bai

In Partial Fulfillment
of the Requirements for the Degree
Doctor of Philosophy in the
School of Physics

Georgia Institute of Technology

December 2019

NEUTRON SCATTERING AND QUANTITATIVE MODELING OF MAGNETIC EXCITATIONS IN FRUSTRATED MATERIALS

Approved by:

Dr. Martin Mourigal, Advisor
School of Physics
Georgia Institute of Technology

Dr. Edward H. Conrad
School of Physics
Georgia Institute of Technology

Dr. D. Zeb Rocklin
School of Physics
Georgia Institute of Technology

Dr. Glen Evenbly
School of Physics
Georgia Institute of Technology

Dr. Angus P. Wilkinson
School of Chemistry & Biochemistry
Georgia Institute of Technology

Date Approved: October 24, 2019

道可道，非常道

Acknowledgments

I am deeply indebted to my parents and my wife, Dai, for the constant support over the years. They give me will and energy to overcome obstacles and pursue an interesting and fulfilling life.

I am deeply indebted to Martin, my Ph.D. adviser, for teaching me to quantum magnetism and neutron-scattering. I am very fortunate that the fate took interesting turns and led me to Martin. He is a constant source of inspiration and imparted me with a high standard of scientific conduct. He provide me with all the resource and every opportunity to pursue interesting science, and treat me with care and respect, for which I am forever grateful.

I would like to thank Joe and Zhiling who opened doors for me to new research possibilities. Joe taught me how to interpret and analyze diffuse scattering data. Zhiling taught me how to make samples. It would be simply not possible for me to have done or be doing many things in this exciting journey without their help.

I would like to thank Yiran, Luwei, Jeremy and Marcus for being great friends and peers. Our daily interaction creates a warm and relaxing environment that I feel comfortable and uplifting. I cherish very much these few years of accompany and all the fun times that we had.

TABLE OF CONTENTS

Acknowledgments iv

List of Tables viii

List of Figures ix

Summary xvii

Chapter 1: Introduction 1

1.1 Effective Spin Models 1

1.2 Material Synthesis 7

1.3 Structural Characterization 11

1.4 Thermodynamic Measurement 14

1.5 Neutron Scattering 17

1.6 Data Analysis 22

1.7 Overview of Research Projects 26

1.8 Publication list 30

Chapter 2: Magnetic Excitations of the Classical Spin-Liquid $MgCr_2O_4$ 31

2.1 Introduction 31

2.2 Methods 34

2.3 Modeling of energy-integrated data 35

2.4 Modeling of energy-resolved data 38

2.5 Discussion 40

Appendices 42

2.A Single-crystal sample 42

2.B Data folding and symmetrization 43

2.C Reverse Monte-Carlo analysis 44

2.D Details of SCGA fittings 46

2.E Hexagonal spin-cluster model 49

2.F Linear spin-wave theory calculations 52

2.G Spin dynamics for different exchange models 54

2.H Mean-field calculations 60

Chapter 3: Hybridized Quadrupolar Excitations in Triangular Ising Magnet FeI_2 62

3.1 Introduction 62

3.2 Methods 68

3.3 Modeling of energy-integrated data 70

3.4 Modeling of energy-resolved data 73

3.5 Discussion 77

Appendices 79

3.A Powder X-ray diffraction measurements 79

3.B Data symmetrization 81

3.C Elastic cuts of neutron-scattering data 83

3.D Ground-state constraints of exchange parameters 84

3.E Self-consistent Gaussian approximation 86

3.F Generalized spin-wave theory 90

3.G GSWT fitting of inelastic neutron-scattering data 91

3.H Symmetry analysis of exchange Hamiltonian 95

Chapter 4: Spin Dynamics Simulations 97

4.1 Introduction 97

4.2 Methods 98

4.3 Benchmark 102

4.4 Application 106

Chapter 5: Outlook 111

References 113

LIST OF TABLES

1.1 Summary of all compounds that I am studying or have studied in the category of their characteristic structural features. Materials that I synthesized are colored blue, all of which are made in the single crystal form. 27

2.D.1 Values of the best fitting parameters for $MgCr_2O_4$. The Weiss temperature is computed from $\theta_{\rm W} = (6J_1 + 12J_2 + 6J_{3a} + 6J_{3b})S(S+1)/3$ with $S = 3/2$. 46

2.E.1 Lattice harmonics entering the instantaneous structure factor in $\mathcal{S}(\mathbf{Q}) = 2/3 \sum_i \langle \mathbf{S}_0 \cdot \mathbf{S}_i \rangle f_i$ and $f_i = \sum_{\mathbf{R}_i} \cos(\mathbf{Q} \cdot (\mathbf{R}_0 - \mathbf{R}_i))$. The level of neighbors is indexed by i. 51

2.G.1 Values of the exchange parameters and fitting results. The reduced χ^2 confirms that the set of parameters, F4, obtained from fitting the energy-integrated quantities and bulk magnetic susceptibility also best reproduces inelastic neutron data. Moreover, the intensity scale I_0 is close to 1, indicating that the calculation for this set of parameters correctly captures the ratio of inelastic to elastic spectral weight. 55

3.A.1 Structural parameters determined from Rietveld refinement of powder X-ray diffraction data. 79

3.E.1 The best SCGA fitting parameters of diffuse-scattering data. 86

3.G.1 The best GSWT fitting parameters of inelastic neutron-scattering data. . . . 93

LIST OF FIGURES

1.1 Eigenvalues of reduced density matrix constructed from the ground state of a Heisenberg spin chain of 7 sites and a random state in the Hilbert space of the chain. 6

1.2 Various crystals grown using the flux method and the Bridgman method. YbOCl, NdOCl, DyOCl and ErOBr were grown using corresponding trihalides as flux at Georgia Tech. Crystals of DyOCl appear in the form of flat squares and long needles. FeI_2 was grown using the Brigman furnace at PARADIM. $NaMnCl_3$, $KMnCl_3$ and $CsMnCl_3$ were grown from motionless Brigman method at Georgia Tech. 9

1.3 Rietveld refinement of PXRD pattern of FeI_2 (top) and calculated patterns without preferred orientations (bottom). 12

1.4 Three distinct low-temperature heat capacity behaviors in $K_2PbCu(NO_2)_6$, DyOCl and ErOBr. The red data in $K_2PbCu(NO_2)_6$ and DyOCl panels are C_p/T and the blue data are the entropy change obtained from integrating C_p/T. 15

1.5 Schematic plot of neutron scattering experiments. The incoming neutron has wave-vector of $\mathbf{k}_i$ and the outgoing neutron has wave-vector of $\mathbf{k}_f$. The momentum transferred from the neutron to the sample is $\mathbf{Q} = \hbar\mathbf{k}_i - \hbar\mathbf{k}_f$ due to the momentum conservation law. 17

1.6 A "compound map" as function of effective spatial dimension and internal dimension of the spin. 26

2.1 (a) The pyrochlore lattice of Cr^{3+} ions (red spheres) in $MgCr_2O_4$ and definition of exchange interactions up to third neighbors. Note that J_{3a} and J_{3b} span the same distance but are not equivalent by symmetry. (b) Contour plot of the goodness of fit χ^2 between calculations and neutron (blue solid lines) and bulk susceptibility (green dashed lines) measurements. FN exchange interactions J_2 and J_{3a} are fixed on a grid with J_1 and J_{3b} fitted at each grid point. The choice of $J_2 \pm J_{3a}$ as plotting axes highlights the nearly equivalent spin structure factors obtained for $J_2 = J_{3a}$. Spin correlations are calculated using the self-consistent Gaussian approximation (SCGA) at $T = 20$ K. The red star is the best overall fit. (c) Momentum dependence of $I_0(\mathbf{Q}) = F(|\mathbf{Q}|)\mathcal{S}(\mathbf{Q})$ and $I_1(\mathbf{Q}) = F(|\mathbf{Q}|)\mathcal{K}(\mathbf{Q})$ along several paths of the Brillouin zone (BZ) at $T = 20$ K, and comparisons with SCGA predictions for NN (dashed black line) and FN (solid red line) models. For the NN model, $J_1 = 38$ K. (d-e) Selected slices across $I_0(\mathbf{Q})$ and $I_1(\mathbf{Q})$ for fixed momentum transfer along the $(0, 0, l)$ and $(0, -l, l)$ directions, respectively, and comparison between NN and FN models calculated using the SCGA. Throughout, white rings are masked aluminum background lines. In (c)–(e), only $E_i = 80$ meV data are shown, but both 40 meV and 80 meV data were included in fits. 35

2.2 Magnetic excitation spectra of $MgCr_2O_4$ at $T = 20$ K measured with incident neutron energy $E_i = 40$ meV, and comparison with linear spin-wave theory (LSWT) calculations for our FN model. (a) Momentum-energy slices through $g^2S(\mathbf{Q}, E)$ along different paths, comparing data (left column) and FN model (right column). (b) Cuts at constant energies $\bar{E} \pm 0.2$ meV through the data (gray circles) and FN model (red lines), where $\bar{E}$ is labeled on each plot. The intensity is multiplied by $\bar{E}$ and offset by 4/sr/Cr for clarity. (c) Energy dependence of the experimental (colored circles) and modeled (colored lines) dynamical structure factor at selected momenta, normalized to the energy transfer $E_0 = 2$ meV. (d) Slices at constant energies $\bar{E} \pm 0.2$ meV through the data (left column) and the FN model (right column) in the (h, k, k) plane. Throughout, blank space is due to kinematic constraints on the scattering, and the extra intensity at $(4, 0, 0)$ arises from a strong nuclear Bragg peak and its associated acoustic phonon. 38

2.3 (a) Sets of ordering wavevectors $\boldsymbol{\kappa}$ with nearly-degenerate energies represented in the Brillouin zone as colored surfaces. The pink surface shows wavevectors with energies within $\sim 0.5\%$ of the global energy minimum for the FN interaction parameters of $MgCr_2O_4$. The blue lines shows wavevectors with energy equal to the global energy minimum for the macroscopically-degenerate phases represented by a blue dashed line in the phase diagram. (b) Mean-field phase diagrams of our FN Heisenberg model as a function of J_2 and J_{3a}, showing results for $J_{3b} = 0$ (left) and $J_{3b} = 0.0085 J_1$ (right). Phases with different ordering wavevectors $\boldsymbol{\kappa}$ are shown in different colors. Special phases (dashed lines) correspond to a macroscopic number of ordering wavevectors with degenerate energies. They emerge from $J_{3a} - J_2 = 0$ (yellow line), which corresponds to the NN model, to form two half-planes corresponding to $J_{3a} - J_2 = \mp J_{3b}$ (green and blue lines). 40

2.A.1 Picture of the single-crystal mount used in our experiments 42

2.A.2 Elastic line of our single-crystal mount showing nuclear Bragg peaks with positions and intensities compatible with the $Fd\bar{3}m$ space-group. 42

2.B.1 Graphical representation of the momentum-space folding procedure used to symmetrize our data. 43

2.C.1 Stereographic projections of the distribution function of spin orientations for (a) $MgCr_2O_4$ spin configurations determined from RMC refinement to single-crystal diffuse-scattering data, and (b) entirely random spin configurations. The distribution functions reveal no evidence for spin anisotropy in $MgCr_2O_4$. The $\mathbf{x}$, $\mathbf{y}$, and $\mathbf{z}$ axes are defined locally such that $\mathbf{z} \in \frac{1}{\sqrt{3}} \langle 111 \rangle$ is parallel to the local three-fold axis of the Cr^{3+} site, and the local $\mathbf{x} \in \frac{1}{\sqrt{6}} \langle 112 \rangle$ and $\mathbf{y} \in \frac{1}{\sqrt{2}} \langle 110 \rangle$ axes are mutually perpendicular and in the plane perpendicular to $\mathbf{z}$. 45

2.D.1 Contour plots of fitting parameters as a function of J_2 and J_{3a}. The red star indicates the best fit, determined from the goodness of fit for the 40 and 80 meV neutron data at 20 K and bulk susceptibility data between 20 K and 400 K [Figure 2.1(b)]. 47

2.D.2 Temperature dependence of bulk magnetic susceptibility of $MgCr_2O_4$. The red dots are data collected at 0.1 Tesla during cool down. The blue curve is the calculation using SCGA at the best fitting parameters listed in Table 2.D.1. The green curve is the Curie-Weiss fit of the data between 200 K and 400 K, yielding a Weiss constant of 405 K. 48

2.E.1 Spin correlations as a function of distance. The red circles are obtained from Monte Carlo simulations at 20 K for the best fitting parameters. The blue triangles are calculated using SCGA up to 10th neighbors, which show excellent agreement with MC results. The yellow diamonds are correlators for the hexagonal spin-cluster model. All the correlators beyond the third nearest neighbor are zero. Both signs and relative strength of the first three correlators from this model resemble those of our microscopic FN model. . 50

2.G.1 Overview of all the exchange parameters used in LSWT calculations. 54

2.G.2 Calculated inelastic spectra along the path $(4,0,0) \rightarrow (2,0,0) \rightarrow (0,0,0) \rightarrow (2,2,0) \rightarrow (2,0,0)$. 56

2.G.3 Calculated inelastic spectra along the path $(4,0,0.5) \rightarrow (2,0,0.5) \rightarrow (0,0,0.5) \rightarrow (2,2,0.5) \rightarrow (2,0,0.5)$. 57

2.G.4 Calculated inelastic spectra along the path $(4,0,1) \rightarrow (2,0,1) \rightarrow (0,0,1) \rightarrow (2,2,1) \rightarrow (2,0,1)$. 58

2.G.5 Calculated inelastic spectra along the path $(4,0,1.5) \rightarrow (2,0,1.5) \rightarrow (0,0,1.5) \rightarrow (2,2,1.5) \rightarrow (2,0,1.5)$. 59

3.1 Illustration of two-magnon bound states in ferromagnetic spin-1 chain and preview of the hybridization mechanism via anisotropic exchange interactions. (a) The ground state and three types of doubly-excited states. The three local states of a spin ($S^z = +1, 0, -1$) are represented by a up-blue-arrow, green-dot and red-down-arrow, respectively. The system lowers its energy by forming bound states of two free single-spin excitations. In particular, the exchange two-magnon bound state gains (TMBS) energy of $-J$ (two adjacent green-dots) and the single-ion bound state (SIBS) gains $2D$ (one red-down-arrow). For a spin-1 system, the energy of SIBS does not depend on D, therefore remain unchanged while all the other excitations, including the single-magnon ($\Delta E = -2J + D$), are pushed up in energy if D is increased. For a sufficiently large D, the SIBS could appear as the lowest-energy mode in the spectrum. (b) The effects of different terms in the Hamiltonian on the excitation spectrum. The easy-axis single-ion anisotropy splits three degenerate local states of spin-1, giving a doubly-degenerate ground state. The Heisenberg exchange interaction induces a collective magnetic ordering at low temperature and further split the ground-state doublet. The single-magnon excitation ($|+1\rangle \to |0\rangle$) becomes dispersive and its full energy-momentum dependence can be mapped out by neutron-scattering, while the SIBS ($|+1\rangle \to |-1\rangle$) remain localized and it is invisible in the conventional experimental probes due to vanishing dipolar matrix element $\langle +1|S^{\pm}|-1\rangle = 0$. Anisotropic exchanges create a new channel of interactions mixing the single-magnon band and SIBS. A hybridization gap is opened and the SIBS gains intensity and appears dispersive in the neutron-scattering measurements. 63

3.2 Structure, exchange pathways and single-ion properties of FeI_2 and an overview of the full inelastic neutron spectrum. (a) Crystal structure and interaction pathways of FeI_2, showing triangular layers of Fe^{2+} ions (orange spheres) and their binding with iodine atoms (purple spheres). (b) The local environment of Fe^{2+} ions, showing a perfect octahedral coordination by iodine atoms with $m\bar{3}m$ symmetry (left) and the weakly trigonal-distorted environment in FeI_2 with $\bar{3}m$ symmetry (right). White arrows indicate the direction of distortion. (c) Single-ion level diagram of the FeI^{2+} ion in FeI_2, showing a hierarchy of interaction energy scales including the dominant cubic crystal field ($\sim$1 eV), subleading spin-orbital coupling ($\sim$10 meV) and trigonal crystal field ($\sim$1 meV). (d) Energy dependence of the dynamical responses of Fe_2 along a high-symmetry path in the momentum space, showing inter-multiplet transitions at high energies, phonons from lattice dynamics at intermediate energies and magnetic fluctuations within $J = 1$ multiplet at low energies. The data is collected at 11 K with incoming neutron energy of 65 meV on SEQUOIA. To the left, it shows a momentum-integrated spectrum in general accordance with the single-ion diagram. . . 66

3.3 Magnetic Bragg peaks and paramagnetic neutron-scattering data of FeI_2. (a) Magnetic structure of FeI_2, showing a stacking of ferromagnetic plane (gray) in a up-up-down-down (blue-blue-green-green) sequence. (b) Elastic neutron-scattering data collected at 1.8 K on CORELLI, showing magnetic Bragg peaks from three equivalent magnetic domains related by 120° rotations. (c) Focused 3D overview of diffuse-scattering data collected at 11 K on SEQUOIA by integrating over energy transfer from 0 to 6 meV, showing intensity patterns consistent with the $m\bar{3}m$ Laue symmetry. (d) Extended diffuse-scattering data in the $(h, k, 0)$-plane at $l = 1/4$ and SCGA fits using the Heisenberg model (top); the same comparison for in the (h, h, l)-plane at $k = 0$. 70

3.4 Low-temperature inelastic neutron-scattering data of FeI_2 and GSWT fits using the anisotropic model. (a) Energy dependence of collective magnetic excitations of FeI_2 collected at 1.8 K on SEQUOIA along a high-symmetry path in the momentum space (left), showing a single-magnon band with several overlapping branches and a gaped single-ion bound state of equally bright intensity and strongly dispersive features. Calculated spin-wave spectrum using best fitting parameters of diffuse-scattering data (right), showing that only the single-magnon band is qualitatively captured. White dashed line indicates the energy of SIBS. The white arrows indicate symmetry equivalent positions in the reciprocal space with large disparity in intensity in the data, which can not be explained by a Heisenberg model with the Fe^{2+} form factor. (b) General spin-wave theory fitting of the inelastic spectrum using the anisotropic model, showing that all the details of both the single-magnon and SIBS are reproduced. (c) The comparison between the data and GSWT fitting for cuts in the out-of-plane direction. (d) Wave-vector dependence of magnetic excitations at selected energies (top panels) and GSWT calculations (bottom panels) using the best fitting parameters of the anisotropic model. Excellent agreements are achieved for cuts in the single-magnon band (4.2 and 4.0 meV) and in SIBS (2.5 meV). . 74

3.A.1 Room-temperature X-ray diffraction patterns of crushed single-crystals measured in a domed sample holder spinning at 16 RPM. The broad peak at $2\theta \sim 20^\circ$ is the background from the polycarbonate dome which keeps the sample from degrading during the measurement. Strong preferred orientation is present in the crushed crystals. 79

3.B.1 Comparison between the raw data ((a), (b)) and the symmetrized data ((c), (d)). The white lines are Brillouin zone boundaries of triangular lattice. . . 81

3.C.1 Elastic cuts of neutron-scattering raw data collected at 1.5K (left) and 11K (right) with incoming energy of 65meV. Three symmetry-equivalent cuts related by 120° rotation are shown for each dataset. The ring-like signals are from aluminum sample holder. Intensities at $(1, 0, 1)$ and equivalent positions are coming from structural domains which are 60° rotation from majority of the crystal. The fraction of minority domains estimated from integrated intensities is less than a few percent. Positions of magnetic Bragg peaks are consistent with reported propagation vectors $\mathbf{k} = (1/4, 0, 1/4), (0, 1/4, 1/4)$ and $(-1/4, -1/4, 1/4)$ [77], corresponding to three magnetic domains of the stripe ordering related by 120 degree rotation. The weak signals at $(1/4, 0, -1/4)$ and related positions are the magnetic Bragg peaks from the minority structural domains. 83

3.D.1 Various low-energy 3D stacking patterns with periodicity less than or equal to four. Positions of magnetic (blue squares) and nuclear Bragg peaks (red disk) of the ABCD and ADCB stacking are shown to the right of respective spin structures. The size of nuclear Bragg peaks is drawn in the scale of their relative intensities. By comparing with experimentally observed diffraction pattern, we find the ABCD stacking is realized in the FeI_2. The energies of ABCD, AACC and ADCB stacking do not depend on $J_0^{'}$ and $J_1^{'}$ and they would be degenerate if $J_{2a}^{'}$ and $J_{2b}^{'}$ were treated the same. 84

3.E.1 Comparison between SCGA calculation (blue triangles) with MC simulation (red circles) of SU(2) spins for the best fitting parameters of diffuse-scattering data. The good agreement is found for all spin correlations up to the phase transition. 86

3.F.1 (a) Length of dipole moment m in parameter space (θ, ϕ). Dark blue line: $SU(2)$ spin coherent state; Red dot: optimal fitting parameter. (b) Excitation spectrum in $SU(3)$ spin wave theory. Color scale: blue (red) refers to the weight of b_{i0} and $b_{i,-1}$ boson, respectively. 90

3.G.1 Progress of various quantities in the GSWT fittings - the tilting angle ((a)), the reduced χ^2 ((b)), the single-ion anistropy D ((c)) and the off-diagonal exchange $J_1^{z\pm}$ ((d)) which is responsible for the hybridization. 91

3.G.2 The high-symmetry path used in the GSWT fitting and the convention of reciprocal lattice vectors. The out-of-plane paths are indicated by black dots. 92

3.G.3 The comparison between the data and GSWT fitting for cuts in the out-of-plane direction. 94

4.1 Thermodynamic properties of the Heisenberg-spin XY model. 103

4.2 The dynamical structure factor of Heisenberg-spin XY model at 1.386K (0.9T$_c$), averaged over 200 initial conditions. 105

4.3 Thermodynamic properties of NN antiferromagneic Heisenberg model on a diamond-lattice. 106

4.4 The dynamical structure factor of the diamond-lattice system at 4K. 107

4.5 The dynamical structure factor of the diamond-lattice system at 20K. 108

4.6 The dynamical structure factor of the diamond-lattice system at 24K. 109

4.7 The dynamical structure factor of the diamond-lattec system at 30K. 110

5.1 (a) The crystal structure of $NaMnCl_3$. (b) Honeycomb layer of Mn^{2+} (purple spheres) mediated through chloride atoms (green spheres). (c) Temperature dependence of heat capacity at selected fields. The dashed lines indicate possible scaling behaviors of the heat capacity data. 112

SUMMARY

The basic theme of my Ph.D. research is understanding exotic magnetic phases of matter and investigate their collective low-energy excitations using neutron-scattering and quantitative modeling. In this thesis, I start with an attempt to answer a list of questions that I had in the beginning of my Ph.D. study, such as why we can use a simple effective model to describe this complex world, how to synthesize and characterize samples, how to analyze the data and find a good theoretical model and many more. There is no unique answer to these questions. I speak from experience and hope to provide a road map to whoever read my thesis and is interested in starting condensed matter research using neutron-scattering. Next, I present two material projects that I assume a major role. In both projects, high resolution single-crystal inelastic neutron-scattering data enables me and my collaborators to make significantly advances in understanding complex dynamical responses of magnetic materials. In Chapter 2, I present our study on a canonical frustrated magnet $MgCr_2O_4$ in the deep cooperative paramagnetic regime. In experiment, we observe a highly structured elastic scattering pattern with continuous excitation spectrum. Using analytic and computational methods, we reveal the highly correlated spin state is proximate to a "spiral spin-liquid" phase and the collective excitations are predominantly fast harmonic precessions of spin on a slow-varying disordered background. In Chapter 3, I present our study on an enigmatic compound with prior investigations dated back to 1970s - FeI_2. In experiment, we observe a bright and dispersive band with "quadrupolar" character, apparently at odds with the dipole selection rule. Using advance numerical techniques, we are able to fully account for this band via a novel hybridization mechanism involving off-diagonal symmetric exchange interactions. In Chapter 4, I introduce detailed implementations of spin dynamics simulations and application to a realistic diamond-lattice system. This technique provides a simple framework to study finite temperature and non-linear effects of complex magnetic materials and has increasingly been used to study disordered and strongly-correlated spin systems. I close this thesis in Chapter 5 with an outlook of future directions.

CHAPTER 1
INTRODUCTION

1.1 Effective Spin Models

The general purpose of condensed matter physics is to understand the microscopic ingredients guiding the physics of materials and the interactions that hold them together. To say that we understand certain physical phenomenon means that we have built a model to satisfactorily explain observations and experimental data, and through mathematical deduction predict things that have not been seen before. It is a futile effort attempting to find a ultimate and universal theory that dictates how everything works. All the models that we built inherently have their range of applicability, because they all presume some hypotheses. Predictions can only be as good as our assumptions. The more generic those hypotheses are, the more applicable models will be, but the more difficult it is for progresses to be made. For a set of hypotheses to be useful, it is necessarily restricted enough so that calculations are possible. We rely on careful comparison with the experimental data to validate our models and hypotheses. The breakdown of model is inevitable when hypotheses are no longer valid. This is not a bad thing per se, because it exposes our blank spots and pushes us to a deeper understanding of the world.

The fact that we can understand nature at all in spite of its enormous complexity is very strange [1]. What lies at the heart of this peculiarity is the separation of scales - length, time, and energy scales. Theoretical models that we build consist of physical degrees of freedom and interactions among them. Not every degree of freedom is active or relevant at the scale of experiments. All the dynamical processes that have much faster time scale and smaller length scale than the experiment only give rise to an average effect on the measurement. Anything that has much slower time scale and larger length scale can be viewed as static

and homogeneous. Temperature provides a natural energy scale. Degrees of freedom with interactions that are too large compared to $k_{\mathrm{B}}T$ freeze and drop out in the low energy effective description. Interactions that are too weak do not manifest themselves amid strong thermal fluctuations. Only interactions that are comparable with $k_{\mathrm{B}}T$ are responsible for experimental observations. Drastic simplifications can be made thanks to the separation of scales, which enable us to understand the world using tractable models. In another word, a problem become particularly hard if it involves many different scales, such as turbulence and protein folding.

My research effort is focusing on a class of materials called Mott insulators. The degrees of freedom include negatively charged electrons and positively charged nucleus, which are held together by the coulomb interaction in a periodic arrangement. In a Mott insulator, there is a competition between the tendency for electrons to be transferred from site to site in the lattice and the coulomb repulsion between electrons. When the repulsive interaction dominate, electrons are localized on each lattice site so that macroscopically the material is not electrically conductor. In addition to the electric charge, an electron also carries a spin degree of freedom which give rises to an atomic scale magnetic moment if not paired with another electron of opposite spin. Transition metal cations Cu^{2+}, Ni^{2+}, Co^{2+}, Fe^{2+} and Mn^{2+} are prime examples of magnetic species. The microscopic interaction between magnetic moments can be the same form as the one between two bar magnets, the dipole-dipole interaction. The interaction decays very quickly as r^{-3} where r is the distance between dipoles. For atoms with small moments such as Cu^{2+} (around $1.73\mu_{\mathrm{B}}$), it is much weaker than the "exchange interaction" modeled by the Heisenberg Hamiltonian

$$H = \frac{1}{2}\sum_{ij} J_{ij}\hat{\mathbf{S}}_i \cdot \hat{\mathbf{S}}_j \,, \tag{1.1}$$

where $\hat{\mathbf{S}}_i$ is quantum mechanical spin operators and J_{ij} is the interaction strength between spins which originates from the direct overlapping of electronic wave functions (direct

exchange) or the indirect overlapping (superexchange), are often on the order of 1 meV. It is called "Heisenberg", because the interaction is isotropic in spin-space, meaning it is the same for all components of the spin. Anisotropic interactions are possible as well and much more common in materials containing rare-earth elements. In that case, this spin Hamiltonian comes from integrating out the charge degrees of freedom with energy scale on the order of 1000 meV. In principle, one should be able to derive the form of interaction between spins and obtain the interaction strength starting from the Schrodinger equation, or making estimation from the density functional theory calculation. However in practice, the Heisenberg Hamiltonian and many other variants are treated as low energy effective model and the exchange constants are fitted from experimental data.

The Heisenberg Hamiltonian might look simple, but it is every bit as hard as any other quantum mechanical many-body problems. The basic quest is to obtain information about the ground state and low-lying excited state. Analytic results for its eigenstates and eigenvalues only exist in one-dimension. Generic quantum mechanical simulation becomes increasingly difficult, if not impossible, in two or three dimensions. The difficulty is sometime dubbed as "the curse of the dimension", namely the dimension of the Hilbert space grows exponentially as the number of spins. The resources needed for the exact diagonalization of the Hamiltonian with a macroscopic number of spins is clearly out of the question. However, as it turns out, the ground state and low-lying excitations are not some random states in the Hilbert space. They are usually states with very low quantum entanglement. A generic quantum state for a system of N spins with local dimension d can be represented as

$$|\psi\rangle = \sum_{\sigma_1,\sigma_2...,\sigma_N=1}^{d} C_{\sigma_1\sigma_2...\sigma_N} |\sigma_1, \sigma_2, ..., \sigma_N\rangle \tag{1.2}$$

using the tensor product of the local states $|\sigma_i\rangle$ as basis states, where i labels the site and the sum runs over the dimension of local Hilbert space. In the mean field approximation

the d^N coefficients are reduced to dN such that

$$|\psi\rangle = \sum_{\sigma_1,\sigma_2...,\sigma_N=1}^{d} C_{\sigma_1}C_{\sigma_2}...C_{\sigma_N}\,|\sigma_1,\sigma_2,...,\sigma_N\rangle$$
$$= \left(\sum_{\sigma_1=1}^{d} C_{\sigma_1}\,|\sigma_1\rangle\right)\left(\sum_{\sigma_2=1}^{d} C_{\sigma_2}\,|\sigma_2\rangle\right)...\left(\sum_{\sigma_N=1}^{d} C_{\sigma_N}\,|\sigma_N\rangle\right), \tag{1.3}$$

which singles out a class of states with no entanglement. Furthermore, instead of worrying about the quantum spin operators and their local basis states, we simply replace them with classical vectors, so that the Hamiltonian becomes a number; the energy of the system. At low temperatures, those vectors form long-range ordered 3D periodic arrays that minimize the energy, giving rise to Bragg peaks in the magnetic structure factor. The collective excitations are spin-waves, which for such systems can be understood as the normal modes of small deviations around the long-range ordered spin structure. There are many examples in which agreement of spin-wave calculations with experiments is impeccable. In other words, the zero entanglement approximation works extremely well for the most prominent features at low temperatures in many magnetic materials.

However, this approximation works poorly, or even fails completely, when the interaction among atoms shows any character of low dimensionality. All bulk solid state materials are three-dimensional, but the interaction between spins can be very anisotropic in space. It may be orders of magnitude stronger in certain directions or planes than others, resulting effectively in 1D or 2D systems over a wide temperature regime. Sometimes the inter-chain or inter-plane coupling is so weak that the system never show three-dimensional ordering down to ~ 100mK which is the lowest achievable temperature in a typical neutron scattering experiment. Most important experimental signatures showing the failure of the mean-field approximation are the lack of ordering and the appearance of exotic excitations due to the presence of strong quantum fluctuations. Accordingly, quantum entanglement among spins can no longer be ignored. In order to treat the system quantum mechanically we have to deal with the exponential blowup of the dimension of the Hilbert space. Focusing on 1D

systems, one sensible way to deal with this problem is to grow the system site by site and truncate the basis when it exceed the limit of computational resources. The basis in which we perform this truncation is very important. A natural choice seems to be the energy eigen-basis, keeping certain number of lowest energy states in every iteration. This idea can be traced back to Wilson's numerical renormalization group. However it turns to be of little success in dealing with generic quantum lattice problems. The correct choice became clear when Steven White invented the Density Matrix Renormalization Group (DMRG) approach in 1992 [2, 3]. We first need to divide the entire system into two subsystems, so called "system" and "environment", and grow both subsystems site by site. At each step, we obtain the ground state wave function of the entire system, $|\psi\rangle = \psi_{ij} |i\rangle |j\rangle$, where index i and j label the basis of the "system" and "environment" respectively. The reduced density matrix of the "system" is constructed by tracing out the "environment", $\rho_{\text{sys}} = \text{tr}_{\text{env}}(|\psi\rangle \langle\psi|)$. The eigenvalues of the reduced density matrix are the probability weight of the ground state on corresponding eigenvectors. As shown in Figure 1.1, when sorted in a descending order, they decay extremely fast, which means that only few states are needed to obtain a very good approximation. On the other hand, this does not work for a random state. The same construction results in a very long tail of slowly decaying probability weights. Another important take-away is found by looking at the "von Neumann entanglement entropy" defined by

$$S = -\sum_{\alpha} \omega_\alpha \log(\omega_\alpha) \tag{1.4}$$

where ω_α are the eigenvalues of the reduced density matrix. It is obvious from Figure 1.1 that the ground state has much less entanglement entropy than a random state. It was later shown that DMRG belongs to a family of algorithms based on the Matrix Product States (MPS),

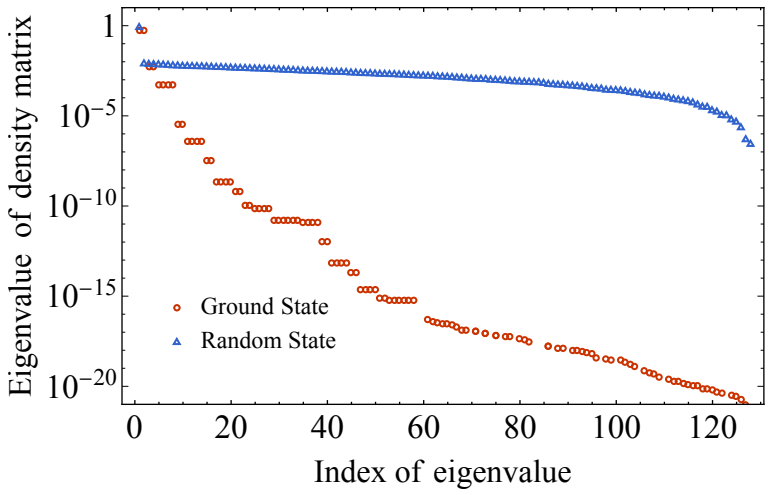

Figure 1.1: Eigenvalues of reduced density matrix constructed from the ground state of a Heisenberg spin chain of 7 sites and a random state in the Hilbert space of the chain.

$$|\psi\rangle = \sum_{\sigma_1,\sigma_2...,\sigma_N=1}^{d} \mathrm{tr}(C_{\sigma_1} \cdot C_{\sigma_2} \cdot ... \cdot C_{\sigma_N}) \, |\sigma_1, \sigma_2, ..., \sigma_N\rangle \ , \tag{1.5}$$

where C_{σ_i} is no longer a number but a matrix and the rank of the matrix is related to the degree of entanglement. This is a natural generalization of mean-field approximation to incorporate the entanglement in a controlled fashion. Again, the ground state is not just any random state and it has special properties. Given suitable parameterizations of the Hilbert space, efficient algorithms can be devised to extract information about the ground state and low-lying excitations.

1.2 Material Synthesis

As a experimental condensed matter physicist, I do not intentionally seek to discover new materials like a chemist would do. However, reading chemistry papers and making materials in the lab are indispensable part of my research. Millions of natural or synthesized materials are recorded in research papers, handbooks, and online databases [4]. Only a very tiny fraction of them have been investigated in depth by physicists. A lot of interesting physics is waiting to be discovered. As I will introduce in more details in the following sections, neutron-scattering is arguably the most powerful experimental tool for investigating both static and dynamical correlations of microscopic magnetic moments in materials. One significant restriction is the relative low flux of neutrons. To achieve a good signal to noise ratio given limited beam time, large single crystals of a few grams are necessary for a successful neutron-scattering experiment. Co-aligning a few small crystals is routine practice to increase the total mass of samples in the neutron beam.

Growing large single crystals is not an easy task. Sometimes it is simply impossible given the time and resources available. From my experience, materials that melts congruently in general has a higher chance of success to grow large single crystals. Congruent melting means that materials does not decompose or turn into something else when melting. A single crystals can usually be obtained by slow cooling from a liquid phase. It greatly increases the quality and size of crystals, if a large temperature gradient can be applied across the sample while it's cooling, so that some parts are in liquid phase while others are in solid phase. An optical floating zone (FZ) furnace is designed to facilitate this process [5]. Typically, a large quantity of desired material is synthesized in the powder form using solid state reaction. The powder is then loaded into a long thin balloon. A hydraulic press is used to press powders into a dense rod, which is cut into a short and a long segment. The short part is loaded on a metal rod at the bottom of the FZ furnace, while the long segment is hanging below another metal rod from the top. Both metal rods can independently move

along vertically direction and rotate about their axis. Mirrors are installed in the FZ furnace and adjusted to focus the light from high power light bulb to a very small area at the center of the furnace. This is where we want our top and bottom material rods to meet. The heat is so focused that material melts at the touching point. The top and bottom material rods are set to rotate in counter-directions and move downwards with different speeds. The idea is to slowly move the melted material away from the hot zone while bringing fresh material in with a suitable pace, so that good large single crystals can be grown during the process. A successful FZ growth can produce a single crystal of several grams each time. All the $MgCr_2O_4$ crystals shown in Section 2.A are grown using this method. I did not personally participate in this endeavor. Dr. Koohpayeh and Dr. Wen made these crystals at Johns Hopkins University back in 2012. Many single crystals of transition metal oxides and rare-earth oxides have been grown successfully using this technique.

All congruent-melting compounds that I grew are not oxides but halides. A complicating factor is that most of them are highly hydroscopic and degrade within a few minutes if not seconds after exposing to air. Materials are often grown in sealed quartz tubes after pumping to high vacuum. Samples need to be handled and stored in the glovebox with water content less than 5ppm. The basic idea of growing large single crystals is the same - slow cooling with a large temperature gradient. Due to the highly hydroscopic nature, we need seal the materials in quartz tubes and use a different type of furnace to achieve this - a Bridgman furnace. The one I used is housed in PARADIM bulk material growth facility at Johns Hopkins University, Figure 1.2. The quartz tube is loaded in a graphite crucible which is hanging from a rod at the top of the furnace inside a vacuum chamber. A conduction coil is wrapped on the outside. The chamber is first pumped into high vacuum. An AC electric current is then sent through the coil and the graphite crucible is heated via induction. One advantage of this furnace is that the entire sample can be melted inside the quartz tube. By slowly rotating and lowering the crucible out of the hot zone, 11 g single crystal of FeI_2 were successfully grown, Figure 1.2. Using a small diameter quartz (~ 8 mm)

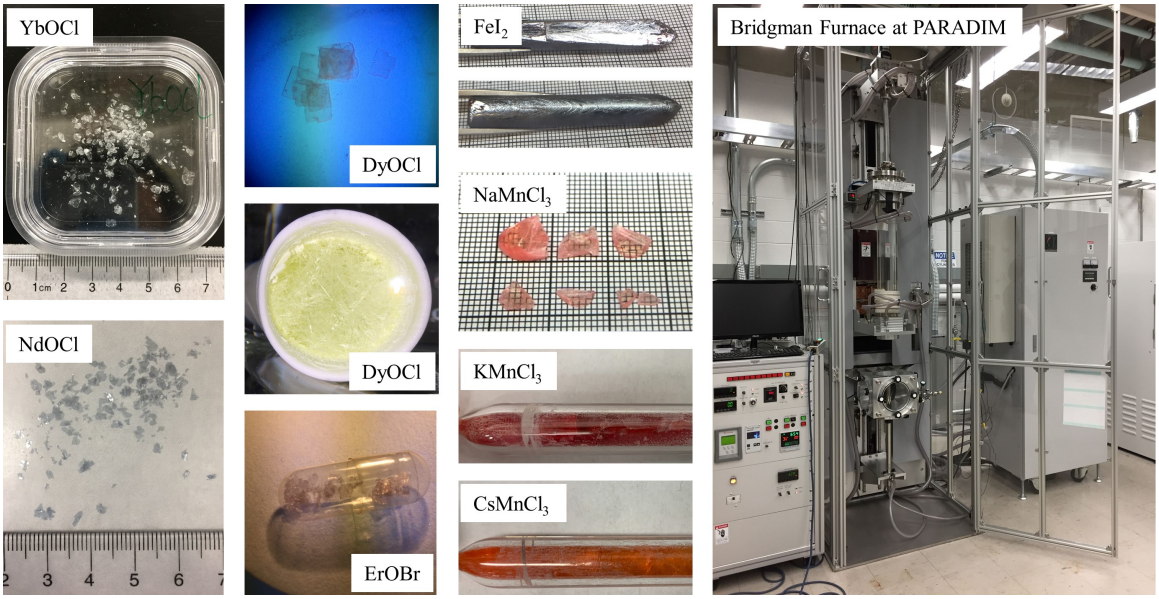

Figure 1.2: Various crystals grown using the flux method and the Bridgman method. YbOCl, NdOCl, DyOCl and ErOBr were grown using corresponding trihalides as flux at Georgia Tech. Crystals of DyOCl appear in the form of flat squares and long needles. FeI_2 was grown using the Brigman furnace at PARADIM. $NaMnCl_3$, $KMnCl_3$ and $CsMnCl_3$ were grown from motionless Brigman method at Georgia Tech.

appears to be the key to achieve this. Attempts with larger diameter did not produce any usable large single crystals. I also managed to grow some other good single crystals in the lab using just small tube furnaces with a method called "motionless" Bridgman method. A quartz tube is filled more than half full with polycrystal samples, then pumped and sealed using flame torch. It is placed horizontally in a tube furnace with one end of the quartz tube closer to the opening of the furnace while the other end close to the center. This is again to create a temperature gradient across the sample. When the cold end starts to solidify, it draws liquid from the hot end and single crystal forms in the process.

A lot of interesting compounds do not melt congruently. The flux method may be used to obtain small crystals. Having crystals, albeit small, is always better than none. We can extract a lot of information from thermodynamic measurements along different crystallographic directions. Many spectroscopic measurements such as Raman or ESR do not require very large crystals either. It is also possible to conduct successful neutron

diffraction experiments using crystals as small as 10 mg. With the advance of modern neutron instrumentation, we could see doing inelastic neutron scattering on small crystals in the next 10 years. Therefore, it is still worth the effort to grow small crystals. Flux growth is one of the widely-used methods. The essential idea is to dissolve the desired material in the liquid phase of some other compounds at a temperature that it does not decompose. Then, small crystals can spontaneously nucleate and grow when solubility is decreased by lowering the temperature. The suitable choice of the flux material is very important. Useful information can be found in binary or ternary phase diagrams databases. I have grown several single crystals in the family of LnOX where Ln is a rare-earth element and X is a halogen element using LnX_3 as flux, Figure 1.2.

1.3 Structural Characterization

Structural characterization is required to confirm if the desired material is successfully synthesized. Powder X-ray diffraction (PXRD) measurement is the most accessible tool and is routinely used in my research for this purpose. Most of times, structural information of the target compound is already recorded in the database. A PXRD scan is often sufficient to tell whether the correct material has been prepared by examining if extra peaks are present in the pattern compared to a reference scan from a structural database. A licensed software called HighScore is installed on the computer controlling the XRD machine at Georgia Tech, which can perform the pattern matching. It is a good practice to first identify the background and find peaks with appropriate criteria, then perform pattern matching with constrained set of chemical elements. Once the target compound is confirmed, a longer scan is needed for detailed structural refinement. I use a free software called Fullprof [6] to do this.

There are many tutorials online for how to use Fullprof. Here I speak from my personal experience and summarize some useful tips. There are generally three sets of the parameters needed to be refined - peak-shape parameters, structural parameters and auxiliary parameters. The shape of Bragg peaks in a PXRD pattern is not a simple Gaussian. It results from a combined effect of XRD instrument and micro-structure of the sample. Getting the peak-shape correct could greatly reduce the residue of a fit. It is possible to perform a so-called "profile matching" to obtain a set of peak-shape parameters first, but it is not always necessary. In this process, the program fits intensities of each individual peak computed from the space group and lattice parameters, instead of calculating from structural parameters. The reason for doing this is that sometimes the relative intensities of different peaks deviate significantly from what a structural model produces due to preferred orientations in grains of the power sample. The "profile matching" or a LeBail fit allows us to focus on getting the peak-shape correct. I find that "Pseudo-Voigt * Axial divergence

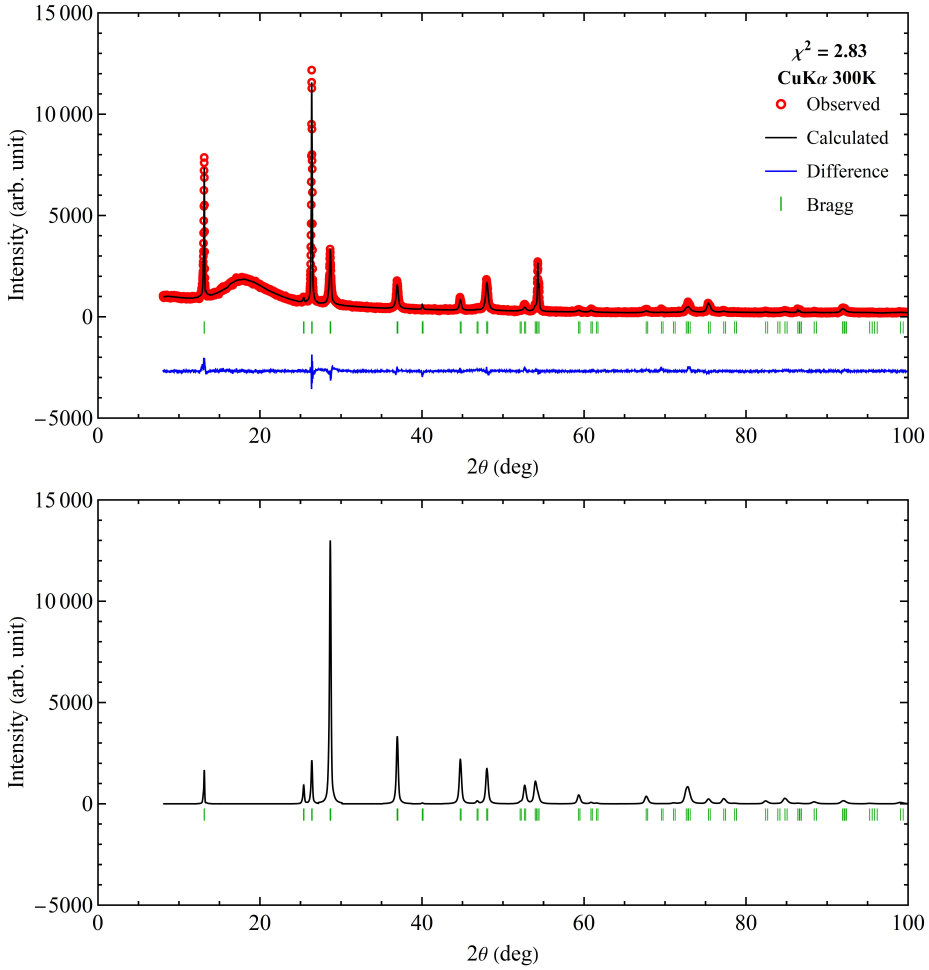

Figure 1.3: Rietveld refinement of PXRD pattern of FeI_2 (top) and calculated patterns without preferred orientations (bottom).

asymmetry" is generally a good peak profile function. To enable the "Asymmetry Parameters" for this function, we need to open the pcr file and change "AsyLim" from 0 to 180, which sets the limiting 2θ angle for asymmetry corrections. The program often crashes if all peak-shape parameters are allowed to change simultaneously. A better way is to release parameters one by one after fit converges every time. In addition, one thing to note is that the "scale" parameter needs to be fixed during the profile matching. After getting a good set of peak-shape parameters, we can start the Rietveld refinement of the structural model. The most common problem of getting the intensity to match is the preferred orientation, commonly existing in powder samples. Fullprof provides two different models for this,

which can be selected using the "Nor" parameter in the pcr file. Figure 1.3 shows a decent Rietveld fit of PXRD pattern of FeI_2 with corrections for preferred orientations. Note relative intensities in the measured pattern are drastically different from calculated patterns without preferred orientations.

1.4 Thermodynamic Measurement

Bulk physical properties can be probed using thermodynamic measurements, such as heat capacity, susceptibility and magnetization. They can offer a lot of useful information about microscopic details of the material. Since the interaction scale of the magnetic degrees of freedom in the material is typically quite small, it is necessary to go to very low temperatures to see any collective behavior. An important instrument called "Physical Properties Measurement System" (PPMS) made by Quantum Design is used in our lab to achieve the low temperature. It provides an operating temperature down to 1.8 K and magnetic field up to 14 Tesla. With the dilution refrigerator option, it can go as low as 50 mK. Quantum Design offers quite a few options to operate with PPMS. All of the thermodynamic data presented in this thesis is collected using PPMS. Figure 1.4 presents three examples with distinct low temperature behaviors that I will now explain.

The specific heat data of Cu-Elpasolite ($K_2PbCu(NO_2)_6$) shows three prominent features - a broad peak centered at 2 K, two sharp peaks around 0.6 K and an up-turn below 0.1 K. The separation of these features in temperature is a manifestation of the hierarchy of microscopic interactions in the material. Cu-Elpasolite is a quasi-1D material with strong intra-chain interactions and weak inter-chain couplings. The broad peak around 2 K releases entropy by accumulating short-range correlations within the chain. The sharp peaks signal the formation of long-range 3D ordering. The two-peak feature depends on the further microscopic details, but a sharp 3D anomaly following a broad peak is quite generic for quasi low dimensional materials. The up-turn below 0.1 K is onset of nuclear spin ordering, resulting from the hyperfine couplings at an energy scale much lower than the exchange interactions.

The specific heat of DyOCl shows very interesting two-peak feature. The broad hump at higher temperatures comes from freezing out the lattice vibration. From the estimated entropy change, we notice the system is releasing Rln(2) from each of the sharp peaks and

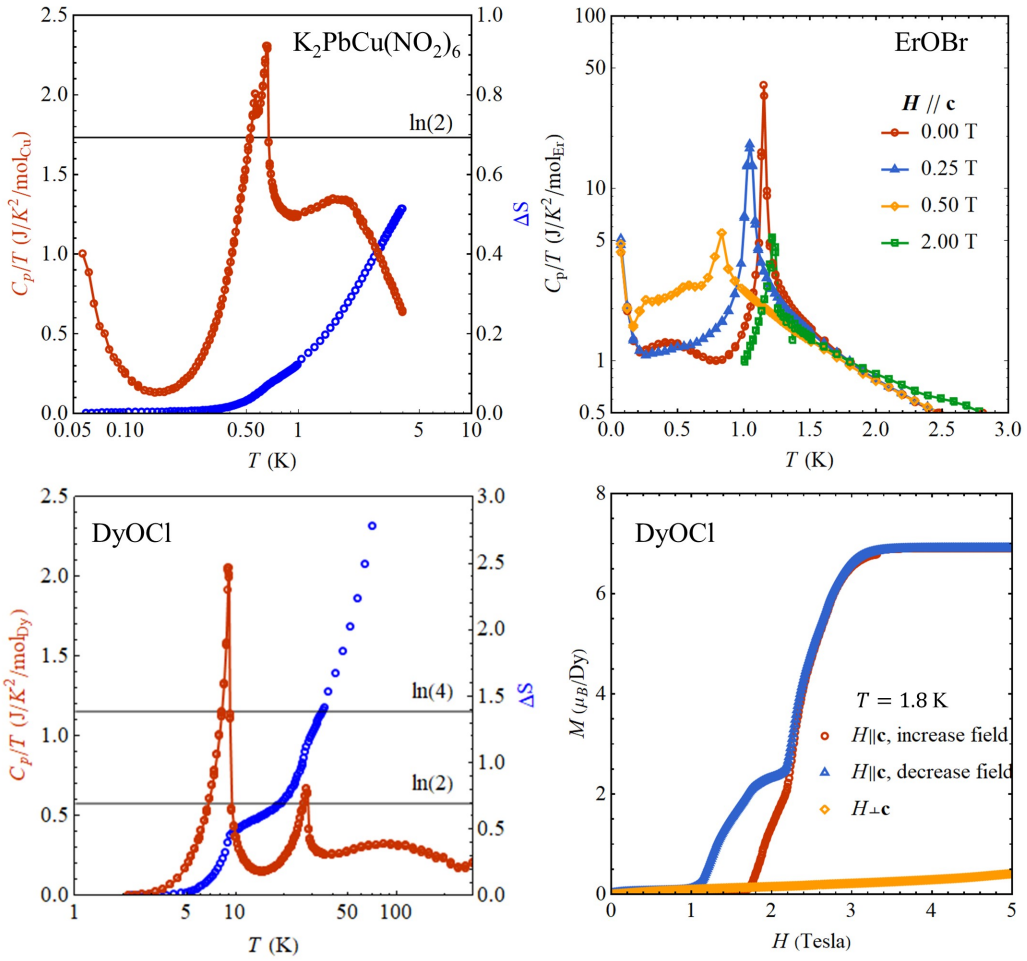

Figure 1.4: Three distinct low-temperature heat capacity behaviors in $K_2PbCu(NO_2)_6$, DyOCl and ErOBr. The red data in $K_2PbCu(NO_2)_6$ and DyOCl panels are C_p/T and the blue data are the entropy change obtained from integrating C_p/T.

Rln(4) in total. This implies that the local degrees of freedom can not be described by an effective spin-$1/2$ like in the case of Cu-Elpasolite where the total entropy change is close to Rln(2). In fact, there are two quasi-degenerate doublet on a site for the Dy^{3+} atom in the crystal of DyOCl. In addition to the dipolar degrees of freedom, there are also quadruplar and octupolar degrees of freedom. The interactions among these higher order multiplets are surprisingly strong in DyOCl, so much so that a collective ordering emerges around 30 K before the magnetic ordering around 9 K. We have performed neutron diffraction experiment in all three temperature regimes at 35 K, 15 K and 1.8 K. The data at higher two temperatures are identical and no magnetic Bragg peaks were observed. Combining with

our heat capacity data, we identify DyOCl as in a multipolar ordered phase between 9 K and 30 K. Neutron is not a effective tool for probing such kind of phases with "hidden order". Other types of advanced experimental techniques have to be used. In the magnetically ordered phase, by doing magnetization measurement with field parallel and perpendicular to the c-axis, we can deduce that spins are confined in the ab-plane with a very strong anisotropy. This mostly like is coming from an anistropic g-factor of Dy^{3+}.

Last but not least, we can also apply magnetic fields when doing the heat capacity measurement. In ErOBr, we observe an extremely rare re-entrant behavior. As we increase the field from 0 Tesla to 0.5 Tesla, the ordering temperature decreases monotonically indicated by the position of the sharp peak. It then jumps back up to a higher temperature at 2 Tesla. If the temperature is kept fixed, we would observe two peaks in heat capacity as we increase the field. Monte Carlos simulations suggests that the second peak leads us to a exotic partially ordered phase at high field, which calls for further neutron-scattering studies on single crystals.

1.5 Neutron Scattering

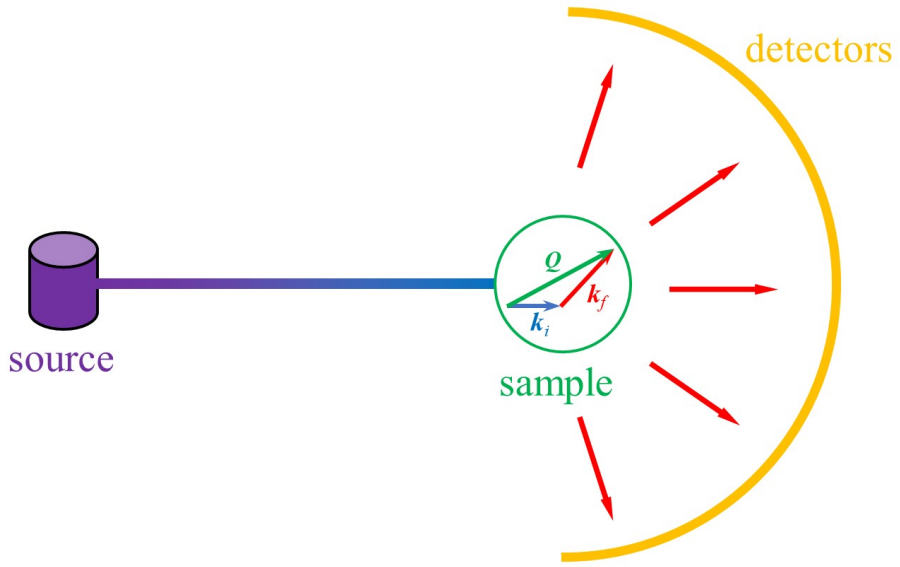

Figure 1.5: Schematic plot of neutron scattering experiments. The incoming neutron has wave-vector of $\mathbf{k}_i$ and the outgoing neutron has wave-vector of $\mathbf{k}_f$. The momentum transferred from the neutron to the sample is $\mathbf{Q} = \hbar\mathbf{k}_i - \hbar\mathbf{k}_f$ due to the momentum conservation law.

The basic components for neutron-scattering, like any other type of scattering experiments, consists of a source of radiation, a sample of interest and a bank of detectors, Figure 1.5. Neutrons are produced from either a fission nuclear reactor source or a spallation source. Currently in US, there are two operating reactor sources having a general user program, hosted at the NIST Center for Neutron Research at Gaithersburg, Maryland and High Flux Isotope Reactor at Oakridge National Lab (ORNL), Oakridge, Tennessee. ORNL also hosts a modern linear accelerator based spallation source (SNS). All of neutron scattering experiments that I participated in were done in these three facilities. Most of neutron instruments operates with neutrons of fixed incoming energies. A series of choppers is installed on the path of neutron beam to select the energy required by the users. The scattering of neutrons follow the basic conservation law of energy and momentum. By comparing the state of out-going and in-coming neutron, we can deduce the energy and

momentum transfer that occurred during scattering, mapping out the entire dispersion band of the dynamical response of the materials. The scattering of neutrons also has to obey the conservation of angular momentum. Since neutron carries intrinsic angular momentum of spin-$1/2$, the initial and final scattering states in the material can only differ at most one unit of angular momentum, correspondingly the spin state of neutron is flipped.

Neutron-scattering is the ideal experimental technique to probe combined structural and magnetic properties of bulk materials [7]. Neutrons do not carry an electric charge and they interact with nucleus via short range nuclear force. The dense bulk materials are actually very sparse from the perspective of neutrons. Most of the neutrons pass through materials without ever being scattered off. Those that do happen to interact with the material will exchange energy and momentum to materials, from which we can infer dynamical properties of the material. Moreover, neutrons can penetrate complex sample environment, such as cryostats, magnets, and pressure cells, which are essential to understand the low temperature physics of materials. Neutrons carry spin and can be used to probe microscopic interactions between magnetic atoms. Neutron scattering is arguably the most powerful and versatile experimental tool for studying low temperature magnetic phenomena. For instance, neutron diffraction is invaluable for understanding low temperature magnetic structures. Inelastic neutron scattering gives access to magnetic excitation spectra, such as spin-waves and spinons. The first experimental evidence of the Haldane conjecture that there is gap in the excitation of the spin-1 chain was obtained from neutron scattering [8].

Generating neutron beams is not a trivial task, because it requires a nuclear reaction. With the advent of modern nuclear reactors and linear accelerators, the supply of steady and well characterized neutron beam becomes possible. Even through the flux of neutron (10^{11} $\mathrm{s}^{-1}\mathrm{m}^{-2}$) is in no comparison with that of X-ray ($10^{17}\mathrm{s}^{-1}\mathrm{m}^{-2}$), data with good statistics can still be collected in a matter of days. Since the magnetic interactions tends to be very small, on the order of 1meV, samples are routinely required to be cooled down to miliKelvin temperature to observe collective physics. A typical cooling instrumentation is

the He^3 refrigerator. It first liquefies He^3 gas by being in contact with a liquid He^4 bath, then uses cold charcoal (below 4K) to further cryo-pump on condensed He^3 liquid. A base temperature of 300mK can be achieved. The temperature of the sample is controlled by the pumping rate of the charcoal that in turn depends on the charcoal temperature. In experiments, an empirical chart between the charcoal and sample temperature is used as a guide for the temperature control.

Neutron Scattering Cross Section

The magnetic neutron scattering cross-section for a system of N identical magnetic ions is given by

$$\frac{d^2\sigma}{d\Omega dE_f}(\mathbf{Q},E) = N\frac{k_f}{k_i}\left(\frac{\gamma r_0}{2}\right)^2 |gf(\mathbf{Q})|^2 \sum_{\alpha,\beta}\left(\delta_{\alpha\beta} - \frac{Q_\alpha Q_\beta}{|\mathbf{Q}|^2}\right)\mathcal{S}^{\alpha\beta}(\mathbf{Q},E)\ , \qquad (1.6)$$

where E_i and $\mathbf{k}_i$ are the energy and wave-vector of incoming neutrons, E_f and $\mathbf{k}_f$ are corresponding quantities of outgoing neutrons. The neutron momentum and energy transfers to the sample are defined as $\hbar\mathbf{Q} = \hbar\boldsymbol{k}_i - \hbar\boldsymbol{k}_f$ and $E \equiv \hbar\omega = E_i - E_f$. $(\gamma r_0/2)^2 = 0.07265$ barn (10^{-24} cm^2) is the conversion factor that places the intensity on absolute scale. Here I assume an isotropic gyromagnetic tensor g and no orbital contribution to the magnetic form-factor $f(\mathbf{Q})$. The dynamic structure factor is defined as

$$\mathcal{S}^{\alpha\beta}(\mathbf{Q},E) = \frac{1}{2\pi\hbar N}\int_{-\infty}^{+\infty} dt e^{-iEt/\hbar}\sum_{n,m}\sum_{i,j} e^{-i\mathbf{Q}\cdot(\mathbf{R}_{i,n}-\mathbf{R}_{j,m})}\langle \hat{S}^\alpha_{i,n}(0)\cdot\hat{S}^\beta_{j,m}(t)\rangle_T\ , \quad (1.7)$$

where $\alpha,\beta = x,y,z$ label components of the Cartesian frame, $S^\alpha_{i,n}(t)$ is the α-component of a spin operator at time t and $\langle\cdots\rangle_T$ denotes the thermal ensemble average. For a spin-isotropic paramagnet, $\mathcal{S}^{\alpha\beta}(\mathbf{Q},E) = \delta_{\alpha\beta}\mathcal{S}^{zz}(\mathbf{Q},E)$, then the above cross-section becomes

$$\frac{d^2\sigma}{d\Omega dE_f}(\mathbf{Q},E) = N\frac{k_f}{k_i}\left(\frac{\gamma r_0}{2}\right)^2 |gf(\mathbf{Q})|^2 2\mathcal{S}^{zz}(\mathbf{Q},E)\ . \qquad (1.8)$$

$\mathcal{S}^{zz}(\mathbf{Q}, E)$ obeys the zeroth moment sum-rule

$$\frac{\int_{-\infty}^{+\infty} \int_{\mathrm{BZ}} dE d^3\mathbf{Q}\, \mathcal{S}^{zz}(\mathbf{Q}, E)}{\int_{\mathrm{BZ}} d^3\mathbf{Q}} = \frac{1}{3} S(S+1) \,, \tag{1.9}$$

where $\int_{\mathrm{BZ}}$ indicates integration over the Brillouin zone.

Instantaneous Structure Factor

The zeroth moment or instantaneous structure factor is defined as

$$\mathcal{S}^{\alpha\beta}(\mathbf{Q}) = \int_{-\infty}^{+\infty} dE\, \mathcal{S}^{\alpha\beta}(\mathbf{Q}, E) \,, \tag{1.10}$$

which in the present formalism becomes

$$\begin{aligned} \mathcal{S}^{\alpha\beta}(\mathbf{Q}) &= \frac{1}{N} \sum_{n,m} \sum_{i,j} e^{-i\mathbf{Q}\cdot(\mathbf{R}_{i,n} - \mathbf{R}_{j,m})} \left\langle \hat{S}^{\alpha}_{i,n}(0) \cdot \hat{S}^{\beta}_{j,m}(0) \right\rangle_T & (1.11) \\ &= \frac{1}{N} \sum_{i,j} e^{-i\mathbf{Q}\cdot(\mathbf{r}_i - \mathbf{r}_j)} \left\langle \hat{S}^{\alpha}_{i,\mathbf{Q}}(0) \cdot \hat{S}^{\beta}_{j,-\mathbf{Q}}(0) \right\rangle_T & (1.12) \\ &= \frac{1}{N} \left\langle \hat{S}^{\alpha}_{\mathbf{Q}}(0) \cdot \hat{S}^{\beta}_{-\mathbf{Q}}(0) \right\rangle_T \,. & (1.13) \end{aligned}$$

First Moment

In turn, the first moment is defined as

$$\mathcal{K}^{\alpha\beta}(\mathbf{Q}) = \int_{-\infty}^{+\infty} dE\, E\, \mathcal{S}^{\alpha\beta}(\mathbf{Q}, E) \,, \tag{1.14}$$

which can be written for a non-Bravais lattice as

$$\begin{aligned} \mathcal{K}^{\alpha\beta}(\mathbf{Q}) &= \frac{1}{N} \sum_{n,m} \sum_{i,j} e^{-i\mathbf{Q}\cdot(\mathbf{R}_{i,n} - \mathbf{R}_{j,m})} \left\langle \hat{S}^{\alpha}_{i,n}(0) \cdot \left[\hat{\mathcal{H}}, \hat{S}^{\beta}_{j,m}(0)\right] \right\rangle_T & (1.15) \\ &= \frac{1}{N} \left\langle \hat{S}^{\alpha}_{\mathbf{Q}}(0) \cdot \left[\hat{\mathcal{H}}, \hat{S}^{\beta}_{-\mathbf{Q}}(0)\right] \right\rangle_T \,. & (1.16) \end{aligned}$$

The time evolution of a spin operator in the Heisenberg picture is

$$\frac{\partial}{\partial t}\hat{S}^{\alpha}_{i,n}(t) = -\frac{i}{\hbar}\left[\hat{S}^{\alpha}_{i,n}(0), \hat{\mathcal{H}}\right], \tag{1.17}$$

where $[\hat{A}, \hat{B}] = \hat{A}\hat{B} - \hat{B}\hat{A}$ denotes the commutator. The above expression can be symmetrized (at least in the case of a centro-symmetric lattice) so that

$$\mathcal{K}^{\alpha\beta}(\mathbf{Q}) = \frac{1}{2N}\left\langle\left[\hat{S}^{\alpha}_{\mathbf{Q}}(0), \left[\hat{\mathcal{H}}, \hat{S}^{\beta}_{-\mathbf{Q}}(0)\right]\right]\right\rangle_T = \frac{1}{2N}\left\langle\left[\left[\hat{S}^{\alpha}_{\mathbf{Q}}(0), \hat{\mathcal{H}}\right], \hat{S}^{\beta}_{-\mathbf{Q}}(0)\right]\right\rangle_T. \tag{1.18}$$

Expressed in terms of the individual spin correlators for our Heisenberg Hamiltonian

$$\mathcal{H} = \frac{1}{2}\sum_{n,m}\sum_{i,j} J_{in,jm}\mathbf{S}_{i,n}\cdot\mathbf{S}_{j,m}\,, \tag{1.19}$$

where $J_{in,jm}$ is the exchange interaction strength, the first moment becomes

$$\mathcal{K}^{\alpha\alpha}(\mathbf{Q}) = -\frac{1}{2N}\sum_{n,m}\sum_{i,j}\sum_{\beta} J_{in,jm}\left\langle\hat{S}^{\beta}_{i,n}(0)\cdot\hat{S}^{\beta}_{j,m}(0)\right\rangle(1-\delta_{\alpha\beta})\left[1-\cos\left(\mathbf{Q}\cdot(\mathbf{R}_{i,n}-\mathbf{R}_{j,m})\right)\right]. \tag{1.20}$$

1.6 Data Analysis

A successful neutron scattering experiment often requires collecting data with a few different incoming neutron energies and at several temperatures above and below any magnetic transitions that exist. This can generate a few hundred gigabytes of data. The first step in the data processing is to normalize to the absolute unit of barn$\cdot$ meV$^{-1}\cdot$sr$^{-1}\cdot$atom^{-1}. This is not strictly necessary, but it can come in handy in analysis and model building later. It is important to record the mass of the sample before putting in the neutron beam if one wish to do this. Normalization is typically done by comparing the intensity in data with that from a Vanadium standard sample for which an accurate calculation for the intensity is possible, since the scattering from Vanadium is predominantly incoherent. The next step is to symmetrize the data using the Laue symmetry of the material. This process combines the data from symmetry-equivalent positions in the reciprocal space and can increase the statistics of the data by several folds. When done properly, the symmetrization process can greatly boost signal-to-noise ratio without creating any spurious new signals. Typical results are shown in Section 3.B.

How do we analyze the data and extract useful information to build a microscopic Hamiltonian model? We can approach this question from several different directions. Our goal is to understand how magnetic moments or spins are arranged in the material and their collective dynamics. If the system is in a long-range ordered state, the coherent scattering of neutron from periodic arrays of spins gives rise to magnetic Bragg peaks at positions of $\mathbf{G} + \mathbf{k}$ in the reciprocal space where $\mathbf{G}$ is a reciprocal lattice point of the bulk material and $\mathbf{k}$ the propagation vector of the magnetic structure. We can first try Fullprof to fit the magnetic Bragg patterns and figure out the magnetic structure. Next is to construct a minimum model that can realize this structure as the ground state. Symmetry consideration is very important in constructing a model. There could be bonds that appear to have the same length, but are inequivalent under operations of the space group symmetry. Sometimes,

the inequivalence of bonds can be seen very straightforwardly from the local environment and atoms involved in the exchange pathways. This situation actually happens much often than one would think, for instance, in the case of J_{3a} and J_{3b} bond in $MgCr_2O_4$ of Chapter 2 and J'_{2a} and J'_{2b} bond in FeI_2 of Chapter 3. The best fitting value of J_{3a} is two order of magnitude larger than J_{3b}. Distinguishing J'_{2a} and J'_{2b} is the key to select the experimentally observed structure. Treating these inequivalent bonds as one parameter will greatly hinder the progress of finding a satisfactory model for the material. After having constructed a model, we can use the Luttinger-Tisza method [9] to obtain a ground state phase diagram and try to place some constraints on the parameters in the model. This method is used in obtaining Figure 2.3 and presented in some detail in Section 2.H. Another way is doing a direct energy minimization or enumerating all possible structures consistent with observed ordering wave-vectors in the material. This is used in Section 3.D. The goal here is to locate regions in the parameter space that are compatible with the experimentally-determined magnetic ground state. Starting with a point in this restricted space, we can further refine the values of model parameters by fitting to the inelastic spectrum using linear spin-wave theory (LSWT) [10]. The purpose of the fitting is partly to find a quantitative model to account for the data. More importantly, it is to discern if anything appears that can not be explained by a simple model and LSWT. That is potentially where new physics emerges. The case of FeI_2 in Chapter 3 is exactly like this, where LSWT fails completely to account for one of low energy modes and pushes us to invoke a generalized spin-wave theory and an anisotropic model, which eventually leads to a comprehensive understanding of the exotic "single-ion bound state".

If the system remains disordered at temperatures of interest, instead of sharp magnetic Bragg peaks we will typically see broad but highly structured scattering pattern in the energy-integrated data, often referred as "diffuse scattering". It directly measures the instantaneous structure factor mentioned in the previous section, which is nothing but the Fourier transform of real-space spin correlations, so we could directly fit the diffuse scatter-

ing data with a Fourier series and extract the spin correlations, cf. Section 2.E. This works very well for single crystal data, not so much for powder data. In this case, we need to employ the Reverse Monte Carlo (RMC) method [11]. RMC starts by placing a random spin at each magnetic site in the crystal structure of the material. The cost function is defined as the difference between the calculated pattern and the measurement. A change of spin state on a random site is proposed and accepted according to Metropolis algorithm with this cost function. At the end, we obtain a box of spins whose correlations match with the data almost perfectly. Not only so, we can also try to discover interesting correlation among emergent objects consisting of several spins, especially when a broad diffuse scattering signal coexist with sharp magnetic Bragg peaks. RMC does not invoke any Hamiltonian and can only help us to understand static properties of the system. In order to investigate the collective spin dynamics, we need to adopt a model. A method called "Self-consistent Gaussian Approximation" (SCGA) [12] is extremely useful in extracting exchange constants from the energy-integrated data of $\mathcal{S}(\mathbf{Q})$. This method imposes a soft constraint on the average of spin length instead of a hard constraint on the length of each individual spin. By doing so, it introduces fluctuations of Gaussian type back in the system and significantly improve results from the mean-field theory. Most amazing aspect is that it can quantitatively approximate the result from the classical Monte Carlo simulations all the way up the phase transitions. This method is very versatile and can be used for both single crystal and powder and applied to any type of bilinear spin model. I used this method to obtain a good Heisenberg model for diffuse scattering data in both $MgCr_2O_4$ project (Figure 2.1) and FeI_2 project (Figure 3.3). Section 3.E presents detailed formulation of SCGA for a generic anisotropic model. Once having a good model about the short range correlations in the paramagnetic phase, we further seek to understand the dynamical response of the system and model the inelastic neutron spectrum. For a generic 3D system, a quantum mechanical calculation like time-dependent DMRG is not feasible. Here, I introduce two semi-classical approaches to study spin dynamics in a disordered system. In Chapter 2, we directly apply

the linear spin-wave theory for a large box of disordered spins. This method is extremely successful in capturing all the details in the spectrum shown in Figure 2.2. Given the spin configuration is not the ground state of the system, we inevitably obtain some imaginary modes after diagonalizing the Hamiltonian. However, the total spectral weight of these imaginary modes is very small. We have tried different methods of handling these modes and the final result does not show any significantly difference. In Chapter 4, I introduce the equation of motion approach. At linear level, it is equivalent to the linear spin-wave theory. The full nonlinear effect is accounted for when solving the equations of motion numerically. This approach is not only able to describe the dynamics in the paramagnetic phase, but also account for the temperature renormalizaiton effects of the spin-wave band in the order phase.

The general methodology that I described in this section is illustrated in great detail in the following chapters of this thesis. It provides the guidance and constitutes basic toolbox in my research.

1.7 Overview of Research Projects

During the past few years of studying condensed matter physics, I was very fortunate to participate in many interesting projects. Some are still actively progressing and will be published in the near future. A complete publication list is provided in the next section. Figure 1.6 gives an overview of compounds that I studied in terms of the spatial dimension of the dominant interactions and the internal dimension of the effective spins. A complete list of compounds is given in Table 1.1. In this thesis, I present in details two material projects and one computational technique. The general theme of my research is to investigate exotic magnetic phases of matters and understand collective dynamics emerged from these phases using neutron-scattering and computational techniques. The material projects that I included in this thesis are at the frontier of this quest.

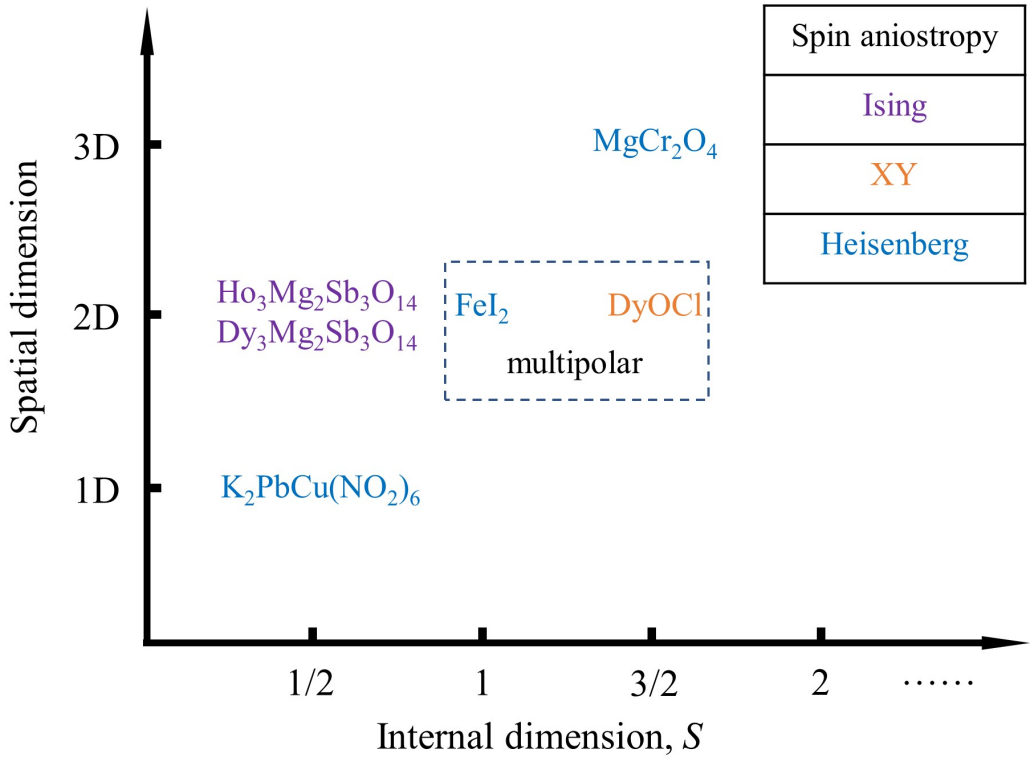

Figure 1.6: A "compound map" as function of effective spatial dimension and internal dimension of the spin.

Table 1.1: Summary of all compounds that I am studying or have studied in the category of their characteristic structural features. Materials that I synthesized are colored blue, all of which are made in the single crystal form.

Kagome	Triangular	Honeycomb	Square
$Dy_2Mg_2Sb_3O_{14}$	FeI_2	$NaMnCl_3$	DyOCl
$Ho_2Mg_2Sb_3O_{14}$	$HoCl_3$	ErOCl	ErOBr
	$Yb_3(OH)_7SO_4{\cdot}H_2O$	YbOCl	NdOCl
Pychlore	**Chain**	**3D-Hex**	**FCC**
$MgCr_2O_4$	$K_2PbCu(NO_2)_6$	$CsMnCl_3$	Ba2DyNbO6
	$KMnCl_3$		Ba2ErNbO6
	$KFeCl_3$		Ba2YbNbO6

$MgCr_2O_4$ presented in Chapter 2 is a canonical frustrated material, consisting of antiferromagnetically coupled spins on a corner-sharing tetrahedron network. Competing interactions lead to a large number of microstates with very small energy differences, preventing the system from entering a long-range ordered state at temperatures predicted from the mean-field theory. Eventually, at a temperature $\sim$20 times smaller than the interaction scale set by the Curie-Weiss constant, the subleading spin-lattice induces a lattice distortion and simultaneously selects a complex magnetic ordered structure. In this study, we set out to understand the short-range spin correlations and the collective dynamics in the deep cooperative paramagnetic regime, just a few Kelvin above the phase transition. Using SCGA and LSWT, we are able to put forward a detailed microscopic model which quantitatively accounts for both energy-integrated and energy-resolved data. We show that excitations of $MgCr_2O_4$ in the cooperative paramagnetic regime are predominantly fast harmonic precessions of spins riding on a spatially-disordered slow-varying background. This is the key advance of our study comparing to earlier efforts of understanding $MgCr_2O_4$ using a phenomenological spin-cluster model. In this work, I participated in the neutron-scattering experiment, processed the data, conducted a co-fitting to the instantaneous structure and the first moment using SCGA and extracted the exchange constants of a Heisenberg model with further neighbor couplings. Our theory collaborators then computed the inelastic spectrum using the linear spin-wave theory with the best fitting parameters. The result agrees with

the data amazing well. This work is published in PRL (Publication 3).

FeI_2 presented in Chapter 3 set foot in a completely different direction. Multipolar degrees of freedom generally exist for a magnetic ion with effective spin larger than $1/2$. It naturally arise from anisotropic charge and magnetization distribution due to crystal electric field and spin-orbital coupling. The detection of multipolar ordering is not easy. In many case, its existence is deduced from the absence, rather than the presence of certain observations in the neutron-scattering experiments, such as DyOCl discussed in Section I.4. FeI_2 is a one of the extremely rare cases where, despite having a conventional long-range ordered state, a "quadupolar" excitation band appears as lowest energy mode in the spectrum. This band is as bright and dispersive as the single-magnon spin-wave band situated at higher energy. The "quadupolar" nature of this excitation band was confirmed long time ago in the 1970s using far inferred spectroscopy with applied magnetic field. In the experiment, people observed a g-factor of this band almost twice as the single-magnon band and later correctly understood it as a two-magnon bound state due to the presence of large single-ion anisotropy. The "doubled" g-factor comes from the spin quantum number of $|\Delta S^z| = 2$ carried by this "quadupolar" band, which however seems to blatantly violate the dipole selection rule. This puzzle has been hanging around over forty years since the very first experiment. Our key contribution in this study is resolving this puzzle completely via a novel mechanism involving off-diagonal symmetric exchange interactions. We find the two-magnon bound state of quadupolar nature is in fact hybridized with the one-magnon band of dipolar nature through this coupling. Both excitations end up of being mixed character. A hybridization gap is opened and the "quadupolar" band becomes bright and dispersive. All of these are strongly supported by extensive quantitative modeling of inelastic neutron-scattering data. In this work, I participated in sample growth and neutron-scattering data, processed and analyzed the data, performed SCGA fitting to the diffuse scattering data and generalized spin-wave theory (GSWT) fitting to the low-temperature inelastic data. Our theory collaborator provides the FORTRAN routines for

GSWT calculations. I wrote the first version of the paper and now is pending review from all collaborators (Publication 9).

The spin dynamics simulation introduced in Chapter 4 is one of my effort to learn advanced numerical techniques and apply to a realistic system. This method is computationally much more demanding than the linear spin-wave theory calculation, but it offer a simple framework to study finite-temperature and non-linear effects. I first present detailed implementation of the algorithm and benchmark calculations against published results on simple cubic system, then apply it to study the full temperature-dependent spin dynamics of an antiferromagnetic diamond lattice model in both ordered and paramagnetic phase.

1.8 Publication list

In Preparation

9. **X. Bai**, S.-S. Zhang, Z. L. Dun, H. Zhang, M. B. Stone, A. I. Kolesnikov, F. Ye, C. D. Batista, and M. Mourigal, "Hybridized Quadrupolar Excitations in Frustrated Triangular Ising Magnet FeI_2", in preparation.

8. **X. Bai**, Y. Jiang, V. O. Garlea, Nicholas P. Butch, and M. Mourigal, "Quadrupolar ordering and orbital dynamics in DyOCl", in preparation.

7. **X. Bai**, Q. Huang, Y. Jiang, V. O. Garlea, and M. Mourigal, "Magnetic properties of a strongly frustrated J_1-J_2 square lattice compound ErOBr", in preparation.

Submitted Journal Articles

6. Z. L. Dun*, **X. Bai***, J. A. M. Paddison, N. P. Butch, C. D. Cruz, M. B. Stone, T. Hong, M. Mourigal, H. D. Zhou, "Quantum Spin Fragmentation in Kagome Ice $Ho_3Mg_2Sb_3O_{14}$", submitted to Physical Review X (June, 2018). ArXiv:1806.04081. * contributed equally.

5. J. A.M. Paddison, P. Mukherjee, **X. Bai**, Z. Dun, C. R. Wiebe, H. Zhou, J. S. Gardner, M. Mourigal, and S. E. Dutton. "Modeling Spin Dynamics in the Singlet Ground State Garnet $Ho_3Ga_5O_{12}$." submitted to Physical Review B (August, 2019). ArXiv:1908.03530.

Published Journal Articles

4. N. Jiang, **X. Bai**, J. Bacsa, M. Mourigal, and H. S. La Pierre, "Synthesis and magneto-structural characterization of the quantum spin liquid candidate, $Yb_3(OH)_7SO_4{\cdot}1.5H_2O$", *Inorganic Chemistry*, **58(15)**, 10417-10423 (2019).

3. **X. Bai**, J. A. M. Paddison, E. Kapit, S. M. Koohpayeh, J.-J. Wen, S. E. Dutton, A. T. Savici, A. I. Kolesnikov, G. E. Granroth, C. L. Broholm, J. T. Chalker, and M. Mourigal, "Magnetic excitations of the classical spin liquid $MgCr_2O_4$", *Physical Review Letters* **122**, 097201 (2019).

2. N. Blanc, J. Trinh, L. Dong, **X. Bai**, A. A. Aczel, M. Mourigal, L. Balents, T. Siegrist, and A. P. Ramirez, "Quantum criticality among entangled spin chains", *Nature Physics* **14**, 273-276 (2018).

1. J. A. M. Paddison, H. S. Ong, J. O. Hamp, P. Mukherjee, **X. Bai**, M. G. Tucker, N. P. Butch, C. Castelnovo, M. Mourigal, and S. E. Dutton, "Emergent order in the kagome Ising magnet $Dy_3Mg_2Sb_3O_{14}$", *Nature Communications* **7**, 13842 (2016).

CHAPTER 2

MAGNETIC EXCITATIONS OF THE CLASSICAL SPIN-LIQUID $MGCR_2O_4$

2.1 Introduction

The classical pyrochlore Heisenberg antiferromagnet is a canonical model of frustrated magnetism. With only nearest-neighbor (NN) exchange interactions, it does not exhibit magnetic ordering down to zero temperature and instead hosts a liquid-like state of strongly correlated spins. In real space, this cooperative paramagnet is a system of underconstrained spins on a network of corner-sharing tetrahedra. The energy is minimized if the vector sum of spins is zero on every tetrahedron, giving rise to an extensive ground-state degeneracy. Mapping spin variables to flux variables on the bonds of the dual diamond lattice transforms this spin constraint to a divergence-free condition on the flux fields. Consequently, spin correlations decay algebraically in real space, and sharp features—known as pinch points—are present in reciprocal space. This exotic magnetic state of matter is termed a Coulomb phase [13, 14, 15].

The best candidate materials to realize the Coulomb phase include the spin-ices [16, 17, 18] and the cubic AB_2O_4 spinels and $NaA'B_2F_7$ fluorides [19, 20, 21], in which a transition-metal ion B occupies a pyrochlore lattice. Canonical spinel examples are $CdCr_2O_4$ [22], $ZnCr_2O_4$ [23], and $MgCr_2O_4$ [24, 25], which are all highly-frustrated antiferromagnets that ultimately order magnetically at temperatures T_N much smaller than the scale of exchange interactions. Contrary to expectations, neutron-scattering experiments on these materials do not reveal sharp pinch points; instead, only broad ring-like diffuse scattering patterns are observed. These experimental observations have been explained in terms of decoupled hexagonal spin clusters—loops of six spins with alternating directions [23]. This phenomenological model has been remarkably successful in explaining magnetic scat-

tering features [23, 24, 25, 26]. However, it leaves three key questions unaddressed. First, what is the microscopic origin of cluster-like scattering in terms of the underlying magnetic interactions? Second, how does frustration relate to the complex ordered structures that B-site spinels often exhibit below T_{N}? And, third, what is the origin of the broad magnetic excitation spectrum observed in the cooperative paramagnetic state? This final question is of particular importance because three explanations have been proposed: (i) scattering is broad in energy, because excitations have a short lifetime; (ii) scattering is broad because the excitations are fractionalised; (iii) scattering is broad in momentum, because the excitations are riding on a disordered background.

In this chapter, we use a combination of neutron spectroscopy and modeling to determine the spin Hamiltonian of $MgCr_2O_4$ the nature of its magnetic excitations in the correlated paramagnetic regime at temperature $T = 20$ K. We study this material because it is a paradigmatic example of a frustrated antiferromagnetic spinel that shows cluster-like scattering above T_{N} and exotic magnetic order below T_{N}. Our results significantly advance previous studies by measuring and explaining the entire four-dimensional (4D) magnetic response of $MgCr_2O_4$ as a function of energy and momentum. We use quantitative modeling to determine a set of exchange interactions that best reproduce our experimental data. Remarkably, we find that linear spin-wave theory accurately captures all the details of the correlated paramagnetic response in $MgCr_2O_4$ revealing the harmonic nature of excitations in this classical spin-liquid. Furthermore, we find that our model remains highly frustrated despite the presence of further-neighbor (FN) interactions. We explain this result by showing that $MgCr_2O_4$ is proximate to a highly-degenerate spiral-spin-liquid phase distinct from the Coulomb phase. Our results suggest that competition between nearly-degenerate states may drive the complex low-temperature states often observed in frustrated B-site spinels.

The crystal structure of $MgCr_2O_4$ at $T = 20$ K is cubic (space group $Fd\bar{3}m$, $a = 8.33$ Å). Magnetic Cr^{3+} ions interact magnetically with their nearest neighbors (NN) primarily via direct exchange ($d_{\mathrm{Cr-Cr}} = 2.95$ Å) and with further neighbors (FN) via su-

perexchange [Fig. 2.1(a)]. Thermo-magnetic measurements [27, 28, 29, 30] reveal net antiferromagnetic interactions with a Weiss constant ranging from $\theta_{\rm W} = -346$K [28, 27] to -433K [29, 30], and are compatible with spin-only magnetic moments for Cr^{3+} ($S = 3/2$ and $g \approx 2.05$) [29]. Below $\sim$ 40 K ($\approx 0.1\theta_{\rm W}$), the magnetic susceptibility markedly departs from the Curie-Weiss law which contrasts with predictions for the NN model [31]. Futhermore a cooperative paramagnetic regime appears with cluster-like scattering [24, 25, 26, 32]. This regime persists down to $T_{\rm N} \approx 13$ K [33, 29, 30], a temperature at which the onset of long-range magnetic ordering [27, 29, 30] is accompanied by a structural distortion to tetragonal or lower symmetry [34, 35, 36] due to spin-lattice coupling [37, 38, 23, 39]. Magnetic Bragg peaks observed below $T_{\rm N}$ are indexed by two inequivalent propagation vectors, $\boldsymbol{k}_{L,1} = \left(\frac{1}{2}, \frac{1}{2}, 0\right)$ and $\boldsymbol{k}_{L2} = \left(1, 0, \frac{1}{2}\right)$ [40] with respect to the cubic cell; the magnetic structure of this so-called "L phase" is not fully solved [40, 32]. Moreover, an additional partially-ordered magnetic phase ("H phase") with a single propagation vector $\boldsymbol{k}_H = (0, 0, 1)$ is observed for some samples between $T_{\rm N}$ and $T_H \approx 16$ K [40, 24].

2.2 Methods

To understand the nature of the magnetic excitations in $MgCr_2O_4$ we performed neutron-scattering experiments to survey its magnetic excitation spectrum as a function of neutron momentum transfer $\hbar\mathbf{Q} = \hbar\boldsymbol{k}_i - \hbar\boldsymbol{k}_f$ and energy transfer $E = E_i - E_f$ to the sample. Large single crystals of $MgCr_2O_4$ were grown using the floating-zone technique following systematic sample-quality studies [29, 30]. Our 10 best crystals were co-aligned on an aluminum holder for a total sample mass $m \approx 13.5$ g and overall mosaic $\leq 3^\circ$ [see Section2.A]. Inelastic neutron-scattering data were collected on the SEQUOIA instrument [41, 42] at the Spallation Neutron Source, Oak Ridge National Laboratory (USA). Incoming neutron energies of $E_i = 40$ and 80 meV were used, yielding elastic energy resolutions of 0.8(4) and 1.6(8) meV, respectively. The sample mount was cooled to $T = 20$ K using a closed-cycle refrigerator and rotated in steps of 1° over a range $> 90^\circ$. The data were converted to absolute units in MANTID [43] using measurements of a vanadium standard, analyzed in HORACE [44] where background contributions and Bragg peaks from the sample were masked, and symmetrised in the $m\bar{3}m$ Laue class [see Section2.B]. The normalized magnetic intensity can be written $I(\mathbf{Q}, E) = (\frac{1}{2}\gamma r_0)^2 [g f(|\mathbf{Q}|)]^2 \, \mathcal{S}(\mathbf{Q}, E)$, where $(\frac{1}{2}\gamma r_0)^2 = 0.07265 \times 10^{-24}$ cm^2 [45], $f(|\mathbf{Q}|)$ is the magnetic form factor, and $\mathcal{S}(\mathbf{Q}, E)$ is the magnetic scattering function. We obtained energy-integrated quantities $I_\alpha(\mathbf{Q}) \equiv \int_0^{E'} \mathrm{d}E \, E^\alpha \, (1 + e^{-E/k_\mathrm{B}T}) \mathcal{S}(\mathbf{Q}, E)$, where $\alpha \in \{0, 1\}$, and $E' = 20$ meV is chosen to encompass the magnetic excitation bandwidth. The quantities $I_0(\mathbf{Q})$ and $I_1(\mathbf{Q})$ are proportional to the instantaneous magnetic structure factor $\mathcal{S}(\mathbf{Q})$ and the first moment $\mathcal{K}(\mathbf{Q})$, respectively, with the constant of proportionality $F(|\mathbf{Q}|) = (\frac{1}{2}\gamma r_0)^2 [g f(|\mathbf{Q}|)]^2$.

2.3 Modeling of energy-integrated data

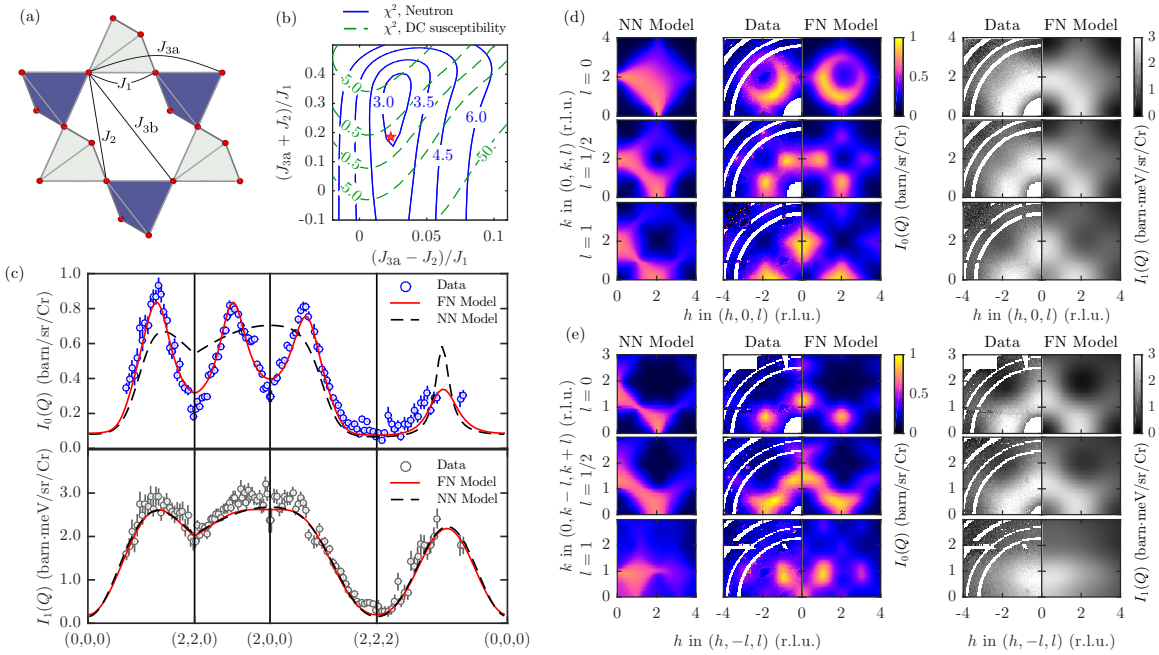

Figure 2.1: (a) The pyrochlore lattice of Cr^{3+} ions (red spheres) in $MgCr_2O_4$ and definition of exchange interactions up to third neighbors. Note that J_{3a} and J_{3b} span the same distance but are not equivalent by symmetry. (b) Contour plot of the goodness of fit χ^2 between calculations and neutron (blue solid lines) and bulk susceptibility (green dashed lines) measurements. FN exchange interactions J_2 and J_{3a} are fixed on a grid with J_1 and J_{3b} fitted at each grid point. The choice of $J_2 \pm J_{3a}$ as plotting axes highlights the nearly equivalent spin structure factors obtained for $J_2 = J_{3a}$. Spin correlations are calculated using the self-consistent Gaussian approximation (SCGA) at $T = 20$ K. The red star is the best overall fit. (c) Momentum dependence of $I_0(\mathbf{Q}) = F(|\mathbf{Q}|)\mathcal{S}(\mathbf{Q})$ and $I_1(\mathbf{Q}) = F(|\mathbf{Q}|)\mathcal{K}(\mathbf{Q})$ along several paths of the Brillouin zone (BZ) at $T = 20$ K, and comparisons with SCGA predictions for NN (dashed black line) and FN (solid red line) models. For the NN model, $J_1 = 38$ K. (d-e) Selected slices across $I_0(\mathbf{Q})$ and $I_1(\mathbf{Q})$ for fixed momentum transfer along the $(0,0,l)$ and $(0,-l,l)$ directions, respectively, and comparison between NN and FN models calculated using the SCGA. Throughout, white rings are masked aluminum background lines. In (c)–(e), only $E_i = 80$ meV data are shown, but both 40 meV and 80 meV data were included in fits.

To model the magnetism of $MgCr_2O_4$, we use the Heisenberg model $\mathcal{H} = \frac{1}{2}\sum_{ij} J_{ij}\,\mathbf{S}_i \cdot \mathbf{S}_j$, where $\mathbf{S}_i$ represents the spin at one of the N sites $\mathbf{R}_i$ of the pyrochlore lattice, and the four interactions $J_{ij} \in \{J_1, J_2, J_{3a}, J_{3b}\}$ extend to third-nearest neighbors [Figure 2.1(a)]. We will show that it is crucial to model the two inequivalent third-neighbor pathways J_{3a} and J_{3b} separately. Our choice of a Heisenberg model is motivated by the small orbital contribution to the magnetic moment ($g \approx 2.05$) and a preliminary reverse Monte Carlo analysis [46, 11, 47] that revealed an isotropic distribution of spin orientations [see Section2.C]. For a Heisenberg paramagnet, the structure factor is the Fourier transform of instantaneous two-spin correlators, $\mathcal{S}(\mathbf{Q}) = \frac{2}{3N}\sum_{ij}\langle \mathbf{S}_i \cdot \mathbf{S}_j \rangle \cos(\mathbf{Q}\cdot\mathbf{r}_{ij})$, where $\mathbf{r}_{ij} = \mathbf{R}_i - \mathbf{R}_j$ is the vector between the spin pair. The first moment contains correlators weighted by the corresponding interactions [48, 49], $\mathcal{K}(\mathbf{Q}) = -\frac{1}{3N}\sum_{ij} J_{ij}\,\langle \mathbf{S}_i \cdot \mathbf{S}_j \rangle\,[1 - \cos(\mathbf{Q}\cdot\mathbf{r}_{ij})]$. As J_{3a} and J_{3b} are symmetry inequivalent but associated with the same lattice harmonics, it is impossible to determine their values by a simple ratio between Fourier coefficients of the structure factor and the first moment. Therefore, we employ the self-consistent Gaussian approximation (SCGA) [50] to calculate $\mathcal{S}(\mathbf{Q})$ and $\mathcal{K}(\mathbf{Q})$ from the magnetic interaction matrix; this method is in excellent quantitative agreement with classical Monte Carlo simulations [see Section2.E].

Determining the magnetic interactions of $MgCr_2O_4$ is a challenging problem, because the spin correlations of the model are essentially degenerate along the line $J_2 = J_{3a}$ in interaction space [51]. Consequently, we used three complementary approaches. First, we performed a global fit to $\mathcal{S}(\mathbf{Q})$ and $\mathcal{K}(\mathbf{Q})$ for a grid of values of J_2 and J_{3a}, with J_1 and J_{3b} fitted at each grid point. The corresponding goodness-of-fit χ^2, shown in Figure 2.1(b), reveals a shallow valley of possible minima [see Section2.D]. Second, we calculated the goodness-of-fit to the temperature dependence of bulk magnetic susceptibility data between 20 K and 400 K for all the parameter sets $\{J_1, J_2, J_{3a}, J_{3b}\}$ extracted from the $\mathcal{S}(\mathbf{Q}) + \mathcal{K}(\mathbf{Q})$ fits. The intersection of χ^2 minima for these two results yields $J_1 = 38.05(3)$ K, $J_2/J_1 = 0.0815$, $J_{3a}/J_1 = 0.1050$ and $J_{3b}/J_1 = 0.0085(1)$ [red star in Figure 2.1(b)]. Finally, we

validated these parameters using fits to the energy-resolved $S(\mathbf{Q},\omega)$, as discussed below [Figure 2.2].

In Figure 2.1, we compare the experimental $I_\alpha(\mathbf{Q})$ with SCGA calculations for our optimized exchange parameters. The FN interactions are small, with a maximum of $J_{3a} \approx 0.1J_1$, and are all antiferromagnetic, in contrast to first-principles estimates [52]. Crucially, however, these interactions quantitatively explain the cluster-like scattering [23, 25, 26, 32] [Figure 2.1(d-e)]. Compared to the NN model, our model correctly captures the suppressed intensity at the $(2,0,0)$ and $(2,2,0)$ pinch-point positions [Figure 2.1(c)], indicating the destruction of the Coulomb phase by FN interactions [50]. In real space, the spin correlators as a function of distance show an alternation in sign, which explains the apparent success of the decoupled hexagonal spin-cluster model [see Section2.E]. However, our FN Heisenberg model enables three key advances. First, it allows a complete microscopic description of the spin dynamics; second, it allows the frustration to be understood in terms of degeneracies of the model; and, third, it enables the nature of the low-temperature ordered phases to be predicted in absence of magnetoelastic effects. We discuss these results in turn below.

2.4 Modeling of energy-resolved data

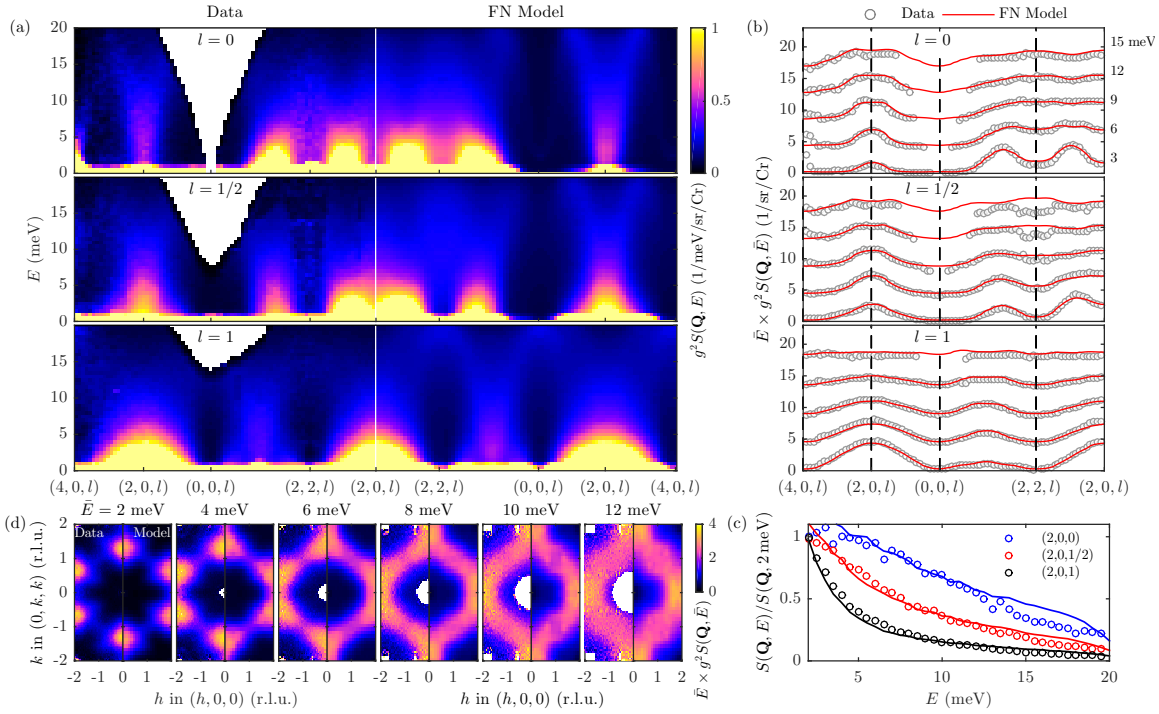

Figure 2.2: Magnetic excitation spectra of $MgCr_2O_4$ at $T = 20$ K measured with incident neutron energy $E_i = 40$ meV, and comparison with linear spin-wave theory (LSWT) calculations for our FN model. (a) Momentum-energy slices through $g^2S(\mathbf{Q}, E)$ along different paths, comparing data (left column) and FN model (right column). (b) Cuts at constant energies $\bar{E} \pm 0.2$ meV through the data (gray circles) and FN model (red lines), where $\bar{E}$ is labeled on each plot. The intensity is multiplied by $\bar{E}$ and offset by 4/sr/Cr for clarity. (c) Energy dependence of the experimental (colored circles) and modeled (colored lines) dynamical structure factor at selected momenta, normalized to the energy transfer $E_0 = 2$ meV. (d) Slices at constant energies $\bar{E} \pm 0.2$ meV through the data (left column) and the FN model (right column) in the (h, k, k) plane. Throughout, blank space is due to kinematic constraints on the scattering, and the extra intensity at $(4, 0, 0)$ arises from a strong nuclear Bragg peak and its associated acoustic phonon.

Magnetic excitation spectra of our sample are presented in Figure 2.2. The excitations are gapless with a bandwidth of ≈ 20 meV ($\sim 4J_1S$), although the dominant contribution to the spectral weight resides below ≈ 5 meV ($\sim J_1S$) [Figure 2.2(a)]. Close to the suppressed pinch point at $(2,0,0)$, excitations are relatively sharp and dispersive along the $(\xi,0,0)$ direction [Figure 2.2(b)], a feature also observed in $NaCaNi_2F_7$ [21]. Along other directions, such as $(2,\xi,0)$ and $(\xi,\xi,0)$, excitations form a broad continuum [Figure 2.2(a)] whose energy dependence is Lorentzian with a relaxation rate that changes with momentum [Figure 2.2(c)]. A simple factorization of the dynamic response as $\mathcal{S}(\mathbf{Q},E)=\mathcal{S}(\mathbf{Q})f(E)$, that implies spatially incoherent excitations, is not possible for $MgCr_2O_4$ [Figure 2.2(d)], in contrast to theoretical predictions for the lowest branch of excitations in the NN model [53].

To examine the nature of excitations, we calculated $\mathcal{S}(\mathbf{Q},E)$ in the paramagnetic regime using linear spin-wave theory (LSWT). For a given set of interactions, we use Monte Carlo simulations to generate ensembles of spin configurations at low but finite temperature to avoid ordering, calculate harmonic fluctuations of each spin configuration, and average $\mathcal{S}(\mathbf{Q},E)$ over these samples [see Section2.F]. We compared LSWT calculations—performed for several sets of interactions near the shallow χ^2 minimum of Figure 2.1(b)—with the entire 4D momentum-energy dependence of our experimental data [see Section2.G]. The best match is obtained for our previously-determined FN model, with LSWT calculations in striking agreement with the experimental observations [Figure 2.2]. It is remarkable that, within the resolution of our experiment, the spin dynamics of $MgCr_2O_4$ at $T = 20$ K can be entirely described by spins precessing around their local mean field, with no evidence of quantum effects [21]. Crucially, this excludes fractionalization and finite lifetime as the physical origin for the broad momentum-energy response; rather, it indicates that scattering is broad in wave-vector because excitations propagate in a spatially disordered background.

2.5 Discussion

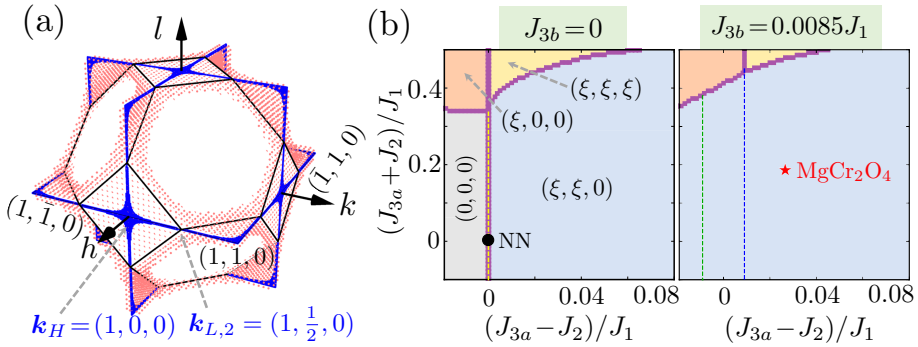

Figure 2.3: (a) Sets of ordering wavevectors $\boldsymbol{\kappa}$ with nearly-degenerate energies represented in the Brillouin zone as colored surfaces. The pink surface shows wavevectors with energies within $\sim 0.5\%$ of the global energy minimum for the FN interaction parameters of $MgCr_2O_4$. The blue lines shows wavevectors with energy equal to the global energy minimum for the macroscopically-degenerate phases represented by a blue dashed line in the phase diagram. (b) Mean-field phase diagrams of our FN Heisenberg model as a function of J_2 and J_{3a}, showing results for $J_{3b} = 0$ (left) and $J_{3b} = 0.0085J_1$ (right). Phases with different ordering wavevectors $\boldsymbol{\kappa}$ are shown in different colors. Special phases (dashed lines) correspond to a macroscopic number of ordering wavevectors with degenerate energies. They emerge from $J_{3a} - J_2 = 0$ (yellow line), which corresponds to the NN model, to form two half-planes corresponding to $J_{3a} - J_2 = \mp J_{3b}$ (green and blue lines).

Our microscopic model also explains the persistence of classical spin-liquid in $MgCr_2O_4$ in spite of the presence of FN interactions. In classical spin liquids, the lowest-energy eigenvalues of the interaction matrix are degenerate throughout large regions of the Brillouin zone, which suppresses magnetic ordering. We find that for the FN parameters of $MgCr_2O_4$, ordering wavevectors $\boldsymbol{\kappa}$ with energies within 0.5% of the global energy minimum describe a large surface near the zone boundary [Figure 2.3(a)]. This result is surprising because FN interactions are generically expected to lift the degeneracy of the NN model. To explain it, we calculated the phase diagram of ordered states as a function of J_2, J_{3a}, and J_{3b} [Figure 2.3(b)]. Crucially, we uncover planes in interaction space along which the degeneracy of possible ordered states is exact and macroscopic. Our FN parameters place $MgCr_2O_4$ in proximity to such a phase, for which wavevectors of the type $\boldsymbol{\kappa} = (1, h, 0)$ are degenerate [blue lines in Figure 2.3(a)]. The corresponding states are a

degenerate set of coplanar spirals [see Section2.H], analogous to the "spiral spin liquid" states previously known only for the J_1-J_2 model on the diamond lattice [54]. This result explains the similarity of cluster-like scattering in $MgCr_2O_4$ to neutron-scattering data for diamond-lattice systems such as $MnSc_2S_4$ [55].

Our analysis sets a benchmark for the comprehensive determination of magnetic interactions in materials in which the traditional approach of spin-wave dispersion modeling is not available—either because the system does not order at an accessible temperature, or the nature of this ordering is controlled by a magnetic Hamiltonian that is distinct from that of the paramagnetic phase due to magnetoelastic effects. The latter is the case in frustrated spinels such as $MgCr_2O_4$ and $ZnCr_2O_4$. Furthermore the presence of several symmetry-unrelated ordering wavevectors makes magnetic structure solution very challenging. However, our results present a key insight: the degeneracy of our spiral spin liquid state encompasses two of the ordering wave-vectors, $\boldsymbol{\kappa}_H$ and $\boldsymbol{\kappa}_{L,2}$, that are observed experimentally below T_N in $MgCr_2O_4$ and $ZnCr_2O_4$. This result suggests that the complex magnetic orderings observed in these frustrated spinels is a consequence of the near-degeneracy of competing ordered states shown in Figure 2.3(a). While the exact ground state is likely selected by magneto-structural effects beyond the Heisenberg model, we anticipate that our paramagnetic Hamiltonian will provide a valuable starting-point to develop a microscopic theory of magnetic ordering in these complex materials.

APPENDIX

2.A Single-crystal sample

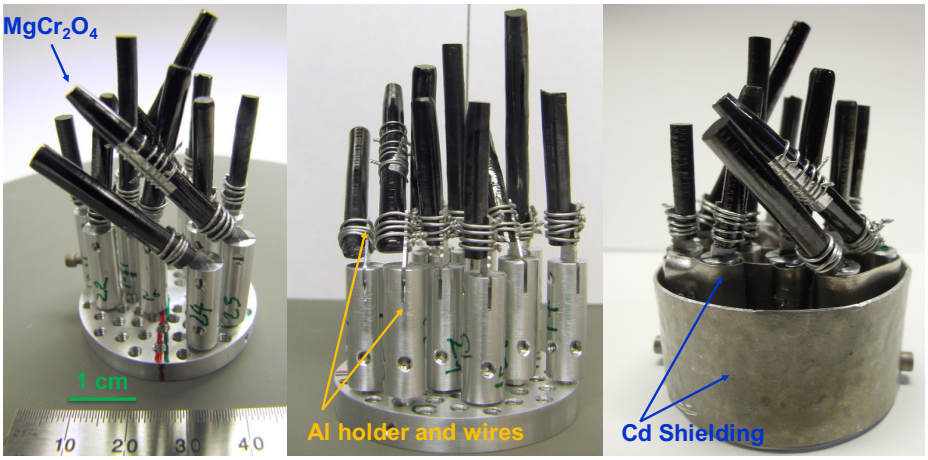

Figure 2.A.1: Picture of the single-crystal mount used in our experiments

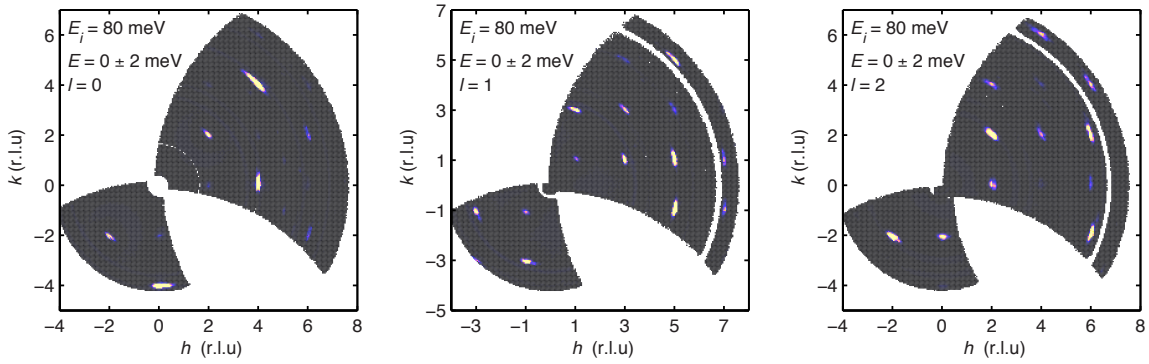

Figure 2.A.2: Elastic line of our single-crystal mount showing nuclear Bragg peaks with positions and intensities compatible with the $Fd\bar{3}m$ space-group.

2.B Data folding and symmetrization

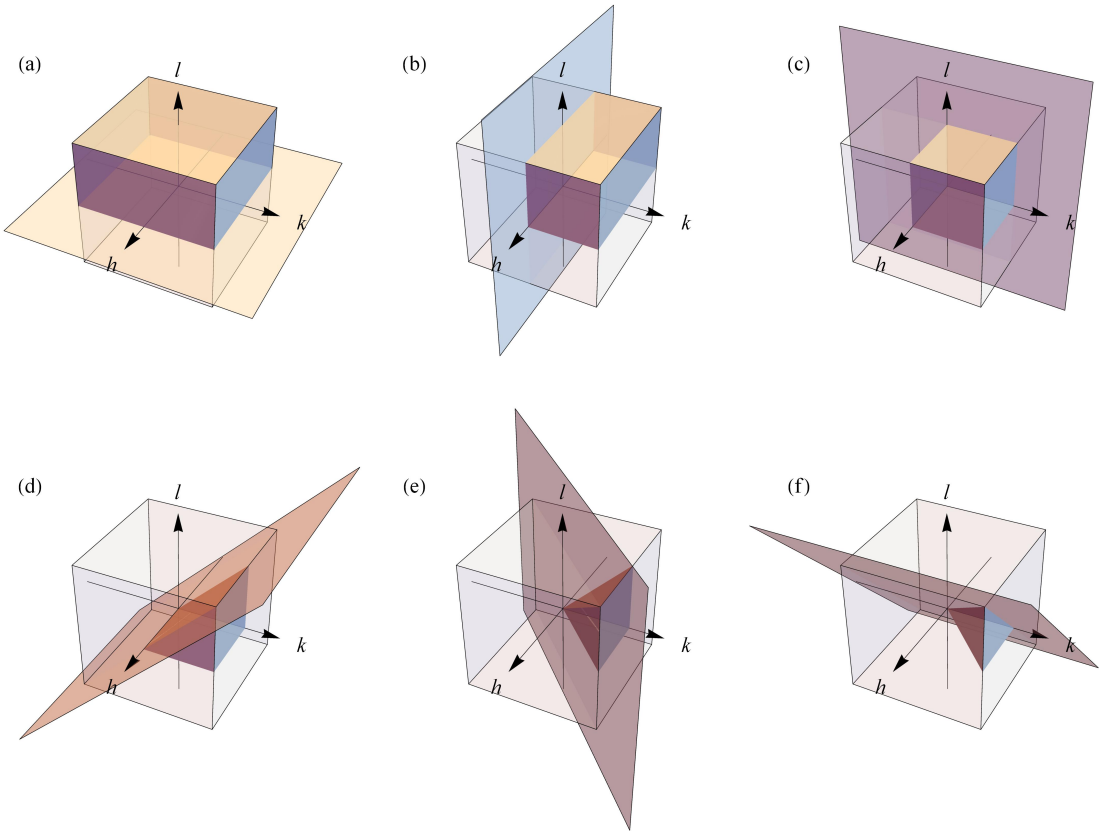

Figure 2.B.1: Graphical representation of the momentum-space folding procedure used to symmetrize our data.

2.C Reverse Monte-Carlo analysis

We used a reverse Monte Carlo (RMC) approach [46] to analyze our magnetic diffuse-scattering data. The RMC approach fits spin configurations directly to experimental data without using a model of the magnetic interactions. For our refinements, we fitted the energy-integrated single-crystal data measured on SEQUOIA at 20 K; the two datasets with incident energies of 40 and 80 meV were fitted simultaneously. Our spin configurations contained $8 \times 8 \times 8$ conventional unit cells (8192 vector spins). Our single-crystal RMC refinement algorithm has been described previously [47]. An overall intensity scale factor and flat background level were refined for each dataset. Fifteen independent refinements were performed and the results averaged to improve their statistical accuracy. Each refinement was performed for 300 proposed moves per spin, after which no significant improvements in the fit was apparent.

Because the RMC approach is data-driven and independent of an interaction model, it allows the assumptions of our interaction model to be tested in an unbiased way. Arguably the most important assumption of our interaction model is that the interactions are described by a Heisenberg form without anisotropy terms. To test this assumption, we look for the presence of anisotropy in the distribution function of spin orientations determined from RMC refinement,

$$p(\theta, \phi) = \frac{n(\theta, \phi)}{N \mathrm{d}(\cos\theta)\, \mathrm{d}\phi},$$

where $n(\theta, \phi)$ is the number spins with orientations within the range $\mathrm{d}(\cos\theta), \mathrm{d}\phi$, and N is the total number of spins. It has been shown previously that RMC refinement is sensitive to anisotropy in pyrochlore magnets, if it is indeed present [56]. However, the function $\ln(p)$ for $MgCr_2O_4$ shown in Figure 2.C.1(a) reveals no evidence for anisotropy, beyond statistical fluctuations that are also present in entirely random spin configurations of the same size [Figure 2.C.1(b)].

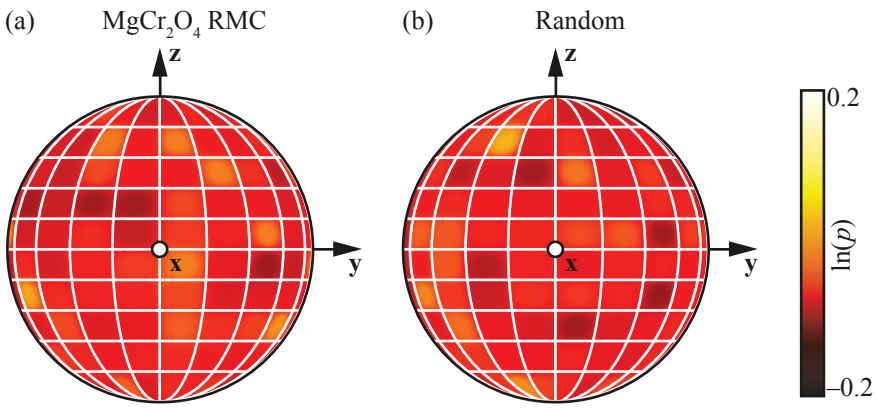

Figure 2.C.1: Stereographic projections of the distribution function of spin orientations for (a) $MgCr_2O_4$ spin configurations determined from RMC refinement to single-crystal diffuse-scattering data, and (b) entirely random spin configurations. The distribution functions reveal no evidence for spin anisotropy in $MgCr_2O_4$. The $\mathbf{x}$, $\mathbf{y}$, and $\mathbf{z}$ axes are defined locally such that $\mathbf{z} \in \frac{1}{\sqrt{3}}\langle 111\rangle$ is parallel to the local three-fold axis of the Cr^{3+} site, and the local $\mathbf{x} \in \frac{1}{\sqrt{6}}\langle 112\rangle$ and $\mathbf{y} \in \frac{1}{\sqrt{2}}\langle 110\rangle$ axes are mutually perpendicular and in the plane perpendicular to $\mathbf{z}$.

2.D Details of SCGA fittings

The SCGA fits to energy-integrated quantities $I_0(\mathbf{Q})$ and $I_1(\mathbf{Q})$ of both 40 and 80 meV datasets are performed for a grid of values of J_2 and J_{3a}. In addition to J_1 and J_{3b}, overall scale factors, s_{40} and s_{80}, are introduced in the fits for each dataset to compensate the discrepancy in the absolute normalization. Constant background parameters $I^{40}_{0,bk}$, $I^{40}_{1,bk}$, $I^{80}_{0,bk}$ and $I^{80}_{1,bk}$ are also included to account for the incoherent scattering signal and instrumental background. Figure 2.D.1 gives an overview of values of all the fitting parameters. The red star is determined from the goodness of fit for the neutron and bulk susceptibility data. The corresponding values are listed in Table 2.D.1.

Table 2.D.1: Values of the best fitting parameters for $MgCr_2O_4$. The Weiss temperature is computed from $\theta_W = (6J_1 + 12J_2 + 6J_{3a} + 6J_{3b})S(S+1)/3$ with $S = 3/2$.

J_1(K)	J_2/J_1	J_{3a}/J_1	J_{3b}/J_1	θ_W (K)	T (K)
38.05(3)	0.0815	0.1050	0.0085(1)	364.3	20

s_{40}	$I^{40}_{0,bk}$	$I^{40}_{1,bk}$	s_{80}	$I^{80}_{0,bk}$	$I^{80}_{1,bk}$
0.6241(5)	0.0675(2)	0.1946(13)	0.6503(5)	0.0843(2)	0.2399(11)

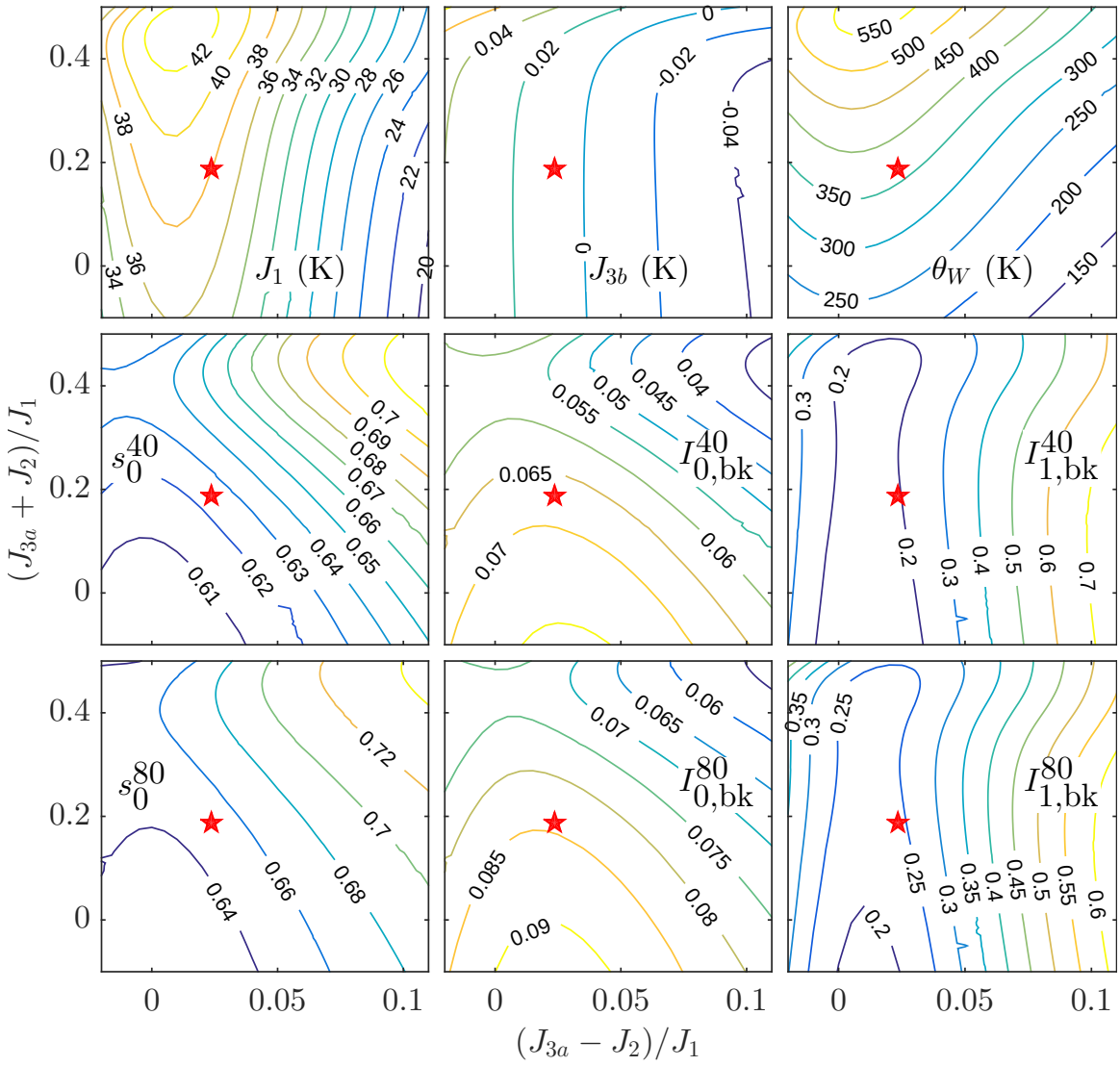

Figure 2.D.1: Contour plots of fitting parameters as a function of J_2 and J_{3a}. The red star indicates the best fit, determined from the goodness of fit for the 40 and 80 meV neutron data at 20 K and bulk susceptibility data between 20 K and 400 K [Figure 2.1(b)].

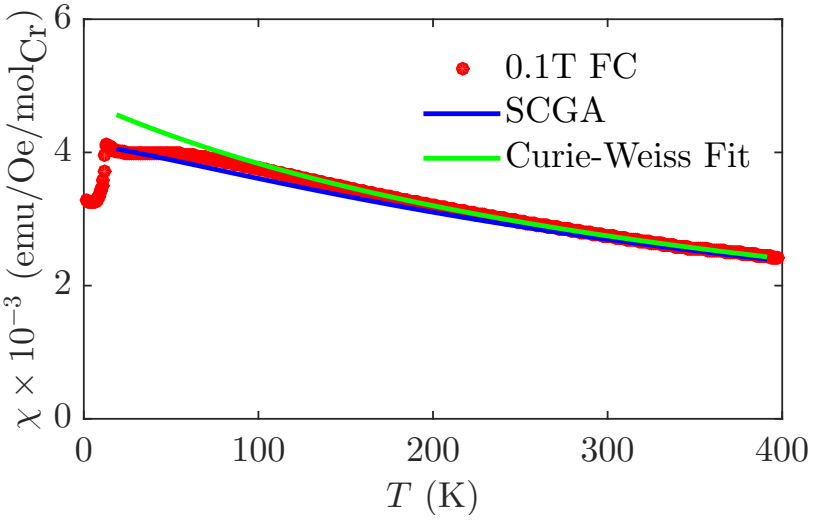

Figure 2.D.2: Temperature dependence of bulk magnetic susceptibility of $MgCr_2O_4$. The red dots are data collected at 0.1 Tesla during cool down. The blue curve is the calculation using SCGA at the best fitting parameters listed in Table 2.D.1. The green curve is the Curie-Weiss fit of the data between 200 K and 400 K, yielding a Weiss constant of 405 K.

2.E Hexagonal spin-cluster model

The structure factor of the hexagonal spin-cluster model is

$$\begin{aligned}\mathcal{S}(\mathbf{Q}) =& \frac{4}{9}\left[\left(1-\cos^2\left(\frac{\pi k}{2}\right)\right)\left(\cos\left(\frac{\pi \ell}{2}\right)-\cos\left(\frac{\pi h}{2}\right)\right)^2\right. \\ &+\left(1-\cos^2\left(\frac{\pi h}{2}\right)\right)\left(\cos\left(\frac{\pi k}{2}\right)-\cos\left(\frac{\pi \ell}{2}\right)\right)^2 \\ &\left.+\left(1-\cos^2\left(\frac{\pi \ell}{2}\right)\right)\left(\cos\left(\frac{\pi h}{2}\right)-\cos\left(\frac{\pi k}{2}\right)\right)^2\right]. \end{aligned} \tag{2.1}$$

This can be rewritten in terms of the Fourier expansion

$$\mathcal{S}(\mathbf{Q}) = \frac{2}{3}\left(\langle \mathbf{S}_0 \cdot \mathbf{S}_0\rangle f_0 + \langle \mathbf{S}_0 \cdot \mathbf{S}_1\rangle f_1 + \langle \mathbf{S}_0 \cdot \mathbf{S}_2\rangle f_2 + \langle \mathbf{S}_0 \cdot \mathbf{S}_3\rangle f_3\right) \tag{2.2}$$

where

$$\langle \mathbf{S}_0 \cdot \mathbf{S}_0\rangle = 1 \tag{2.3}$$

$$\langle \mathbf{S}_0 \cdot \mathbf{S}_1\rangle = -1/3 \tag{2.4}$$

$$\langle \mathbf{S}_0 \cdot \mathbf{S}_2\rangle = 1/6 \tag{2.5}$$

$$\langle \mathbf{S}_0 \cdot \mathbf{S}_3\rangle = \left(\langle \mathbf{S}_0 \cdot \mathbf{S}_{3\mathrm{a}}\rangle + \langle \mathbf{S}_0 \cdot \mathbf{S}_{3\mathrm{b}}\rangle\right)/2 = -1/12\,. \tag{2.6}$$

All the other correlators vanish identically. The Fourier functions f_i are given in Table 2.E.1. In particular, two types of the third nearest neighbors are distinguished by the lattice symmetry, while their corresponding Fourier basis take the same form.

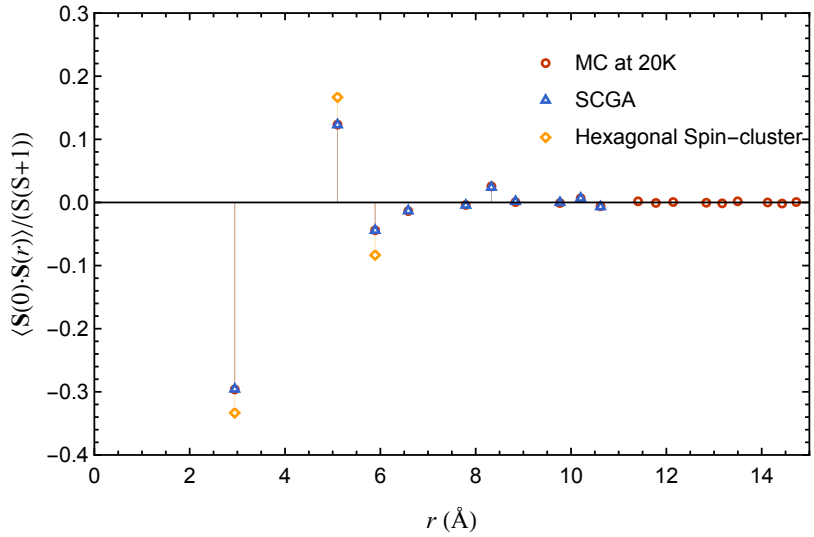

Figure 2.E.1: Spin correlations as a function of distance. The red circles are obtained from Monte Carlo simulations at 20 K for the best fitting parameters. The blue triangles are calculated using SCGA up to 10th neighbors, which show excellent agreement with MC results. The yellow diamonds are correlators for the hexagonal spin-cluster model. All the correlators beyond the third nearest neighbor are zero. Both signs and relative strength of the first three correlators from this model resemble those of our microscopic FN model.

Table 2.E.1: Lattice harmonics entering the instantaneous structure factor in $\mathcal{S}(\mathbf{Q}) = 2/3 \sum_i \langle \mathbf{S}_0 \cdot \mathbf{S}_i \rangle f_i$ and $f_i = \sum_{\mathbf{R}_i} \cos(\mathbf{Q} \cdot (\mathbf{R}_0 - \mathbf{R}_i))$. The level of neighbors is indexed by i.

i		f_i
0		1
1	$2\times$	$\Big[\cos(2\pi\cdot h/4)\Big\{\cos(2\pi\cdot k/4)+\cos(2\pi\cdot \ell/4)\Big\}+\cos(2\pi\cdot k/4)\cos(2\pi\cdot \ell/4)\Big]$
2	$4\times$	$\Big[\cos(2\pi\cdot h/2)\cos(2\pi\cdot k/4)\cos(2\pi\cdot \ell/4)$ $+\cos(2\pi\cdot h/4)\Big\{\cos(2\pi\cdot k/2)\cos(2\pi\cdot \ell/4)+\cos(2\pi\cdot k/4)\cos(2\pi\cdot \ell/2)\Big\}\Big]$
3	$4\times$	$\Big[\cos(2\pi\cdot h/2)\Big\{\cos(2\pi\cdot k/2)+\cos(2\pi\cdot \ell/2)\Big\}+\cos(2\pi\cdot k/2)\cos(2\pi\cdot \ell/2)\Big]$
4	$2\times$	$\Big[\cos(2\pi\cdot 3h/4)\Big\{\cos(2\pi\cdot k/4)+\cos(2\pi\cdot \ell/4)\Big\}+\cos(2\pi\cdot 3k/4)\Big\{\cos(2\pi\cdot h/4)+\cos(2\pi\cdot \ell/4)\Big\}$ $+\cos(2\pi\cdot 3\ell/4)\Big\{\cos(2\pi\cdot h/4)+\cos(2\pi\cdot k/4)\Big\}\Big]$
5	...	...

2.F Linear spin-wave theory calculations

Understanding of the spin wave excitations $MgCr_2O_4$ was enabled by comparing neutron scattering results to semiclassical simulations of $\mathcal{S}(\mathbf{Q}, E)$ for the pyrochlore lattice, with $\mathbf{Q}, E, T$ and the values of further neighbor interactions taken as the input parameters.

Our numerical modeling proceeded as follows: we studied spins on a pyrochlore lattice with $6 \times 6 \times 6$ cubic unit cells and periodic boundary conditions, containing 3456 spins in total, governed by a Heisenberg Hamiltonian with nearest neighbor J and longer ranged interactions J_2, J_{3a} and J_{3b}. To calculate $\mathcal{S}(\mathbf{Q}, E)$, we first computed an approximate classical ground state using the Monte Carlo technique. In the case of pure nearest neighbor interactions (where the ground state is massively degenerate) we reached the $T \to 0$ limit by following the Monte Carlo iterations with a steepest descent method to arrive at an effectively exact ground state. In the case of further neighbor interactions, the true ground state is ordered (with a very small T_{N}); since our study was interested in the spin wave structure of the disordered paramagnetic phase, we thermalized the system at approximately 10 K to ensure the ordered state was never reached. Having derived a base classical spin configuration, we then numerically constructed the quantum harmonic spin wave Hamiltonian as in Walker and Walstedt [57, 58], exactly diagonalized the Hamiltonian using a Bogoliubov transformation to obtain the full single-excitation spectrum, and then used the resulting eigenstates to calculate the dynamical structure factor $\mathcal{S}(\mathbf{Q}, E)$, with Bose factors added to incorporate finite temperature. This method produces the leading order term in the $1/S$ expansion; at this level the eigenfrequencies of the quantum large-S problem and the normal modes of small oscillations about the classical ground state are identical.

To improve our numerical results, we repeated the above process ten times for each set of interactions chosen, and then averaged the resulting distributions of $\mathcal{S}(\mathbf{Q}, E)$ over classical ground states. For the nearest neighbor case, averaging over ground states mitigates finite size effects that result from studying the excitations about a single ground state

chosen from a massively degenerate manifold. For case of longer ranged interactions, our choice to study the system at finite temperature to prevent ordering led to a fraction of the lowest energy modes ($E \sim T$ or below) being unstable, as they described oscillations about a configuration which was not the system's true ground state. Such modes have complex eigenfrequencies and cannot be properly normalized in the Bogoliubov formalism. However, as far as we were able to ascertain, the momentum space distribution of the unstable modes is an effectively random fraction of the total spectral weight at that energy, so we were able to reconstruct the low-energy excitations by averaging over thermal "ground state" spin configurations to sample from the stable modes which had well-defined normalization, simply omitting any contribution from unstable modes.

Finally, to study the energy-integrated spectral weight $\mathcal{S}(\mathbf{Q})$ we employed the self-consistent Gaussian approximation outlined in Ref. [50]. Unlike the harmonic approach detailed above, this method implicitly accounts for interactions between spin waves and does not suffer from normalization issues due to unstable modes, but it is a time-independent method and thus does not provide energy-resolved data. As its computational cost is significantly lower than the harmonic approach, we used it to extract the longer ranged interactions J_2, J_{3a} and J_{3b} from a numerical fit to the neutron scattering data, and then used those parameters in the harmonic calculation to obtain finite-energy results.

2.G Spin dynamics for different exchange models

To make quantitative comparison, we fit results of LSWT calculations to the experimental data with three fitting parameters, the overall energy scale W, the intensity scale I_0 and a constant background I_{bk}. The fitting is performed simultaneously for constant-momentum slices with $L = 0, 0.5, 1$ and 1.5 r.l.u. and energy transfer between 1.5 meV and 25 meV. The simulated data is interpolated on a $\mathbf{Q}$-grid that matches the experimental data and the overall intensity is normalized according to the sum rule, prior to the fitting. All the exchange models and corresponding fitting results are summarized in Figure 2.G.1 and Table 2.G.1. Detailed inelastic spectra are presented in Figure 2.G.2 to 2.G.5.

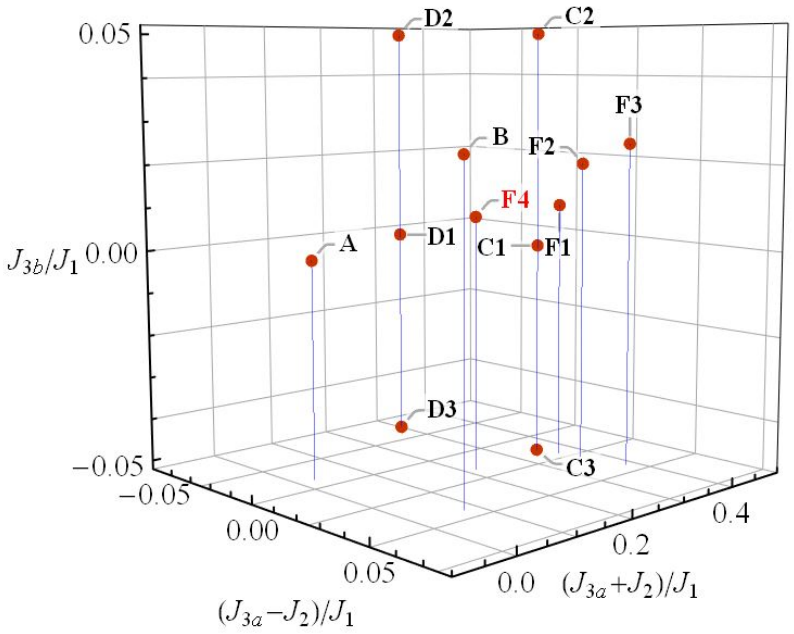

Figure 2.G.1: Overview of all the exchange parameters used in LSWT calculations.

Table 2.G.1: Values of the exchange parameters and fitting results. The reduced χ^2 confirms that the set of parameters, F4, obtained from fitting the energy-integrated quantities and bulk magnetic susceptibility also best reproduces inelastic neutron data. Moreover, the intensity scale I_0 is close to 1, indicating that the calculation for this set of parameters correctly captures the ratio of inelastic to elastic spectral weight.

	A	B	C1	C2	C3	D1
J_2/J_1	0	0	0.15	0.15	0.15	0.15
J_{3a}/J_1	0	0.05	0.17	0.17	0.17	0.12
J_{3b}/J_1	0	0.025	0	0.05	-0.05	0
W	35.918	19.3418	17.6436	18.0734	16.9698	16.0742
I_0	0.74193	1.213	1.4196	1.3546	1.3229	1.3707
I_{bk}	0.034101	0.027938	0.038731	0.026772	0.04146	0.044522
χ^2	0.037663	0.031606	0.034808	0.033442	0.044838	0.044944

	D2	D3	F1	F2	F3	F4
J_2/J_1	0.15	0.15	0.15	0.15	0.15	0.08145
J_{3a}/J_1	0.12	0.12	0.1774	0.185	0.2	0.105
J_{3b}/J_1	0.05	-0.05	0.01	0.02	0.025	0.00878
W	17.1556	12.5	17.636	18.3618	18.3784	20.442
I_0	1.3857	0.48817	1.4227	1.3598	1.354	1.0531
I_{bk}	0.033162	0.099382	0.03265	0.027036	0.020982	0.0317
χ^2	0.037591	0.077936	0.032907	0.032382	0.033653	0.031522

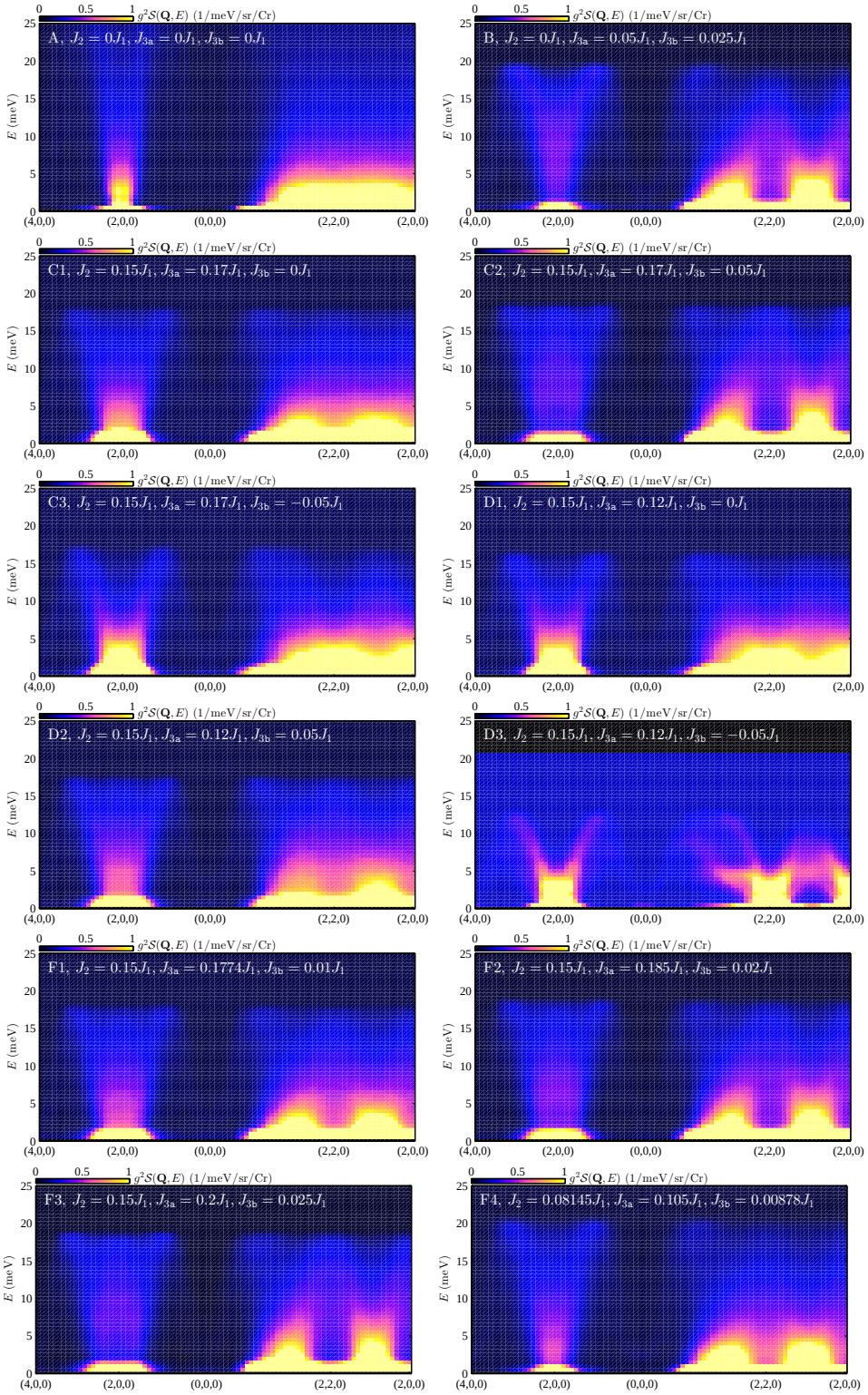

Figure 2.G.2: Calculated inelastic spectra along the path $(4, 0, 0) \rightarrow (2, 0, 0) \rightarrow (0, 0, 0) \rightarrow (2, 2, 0) \rightarrow (2, 0, 0)$.

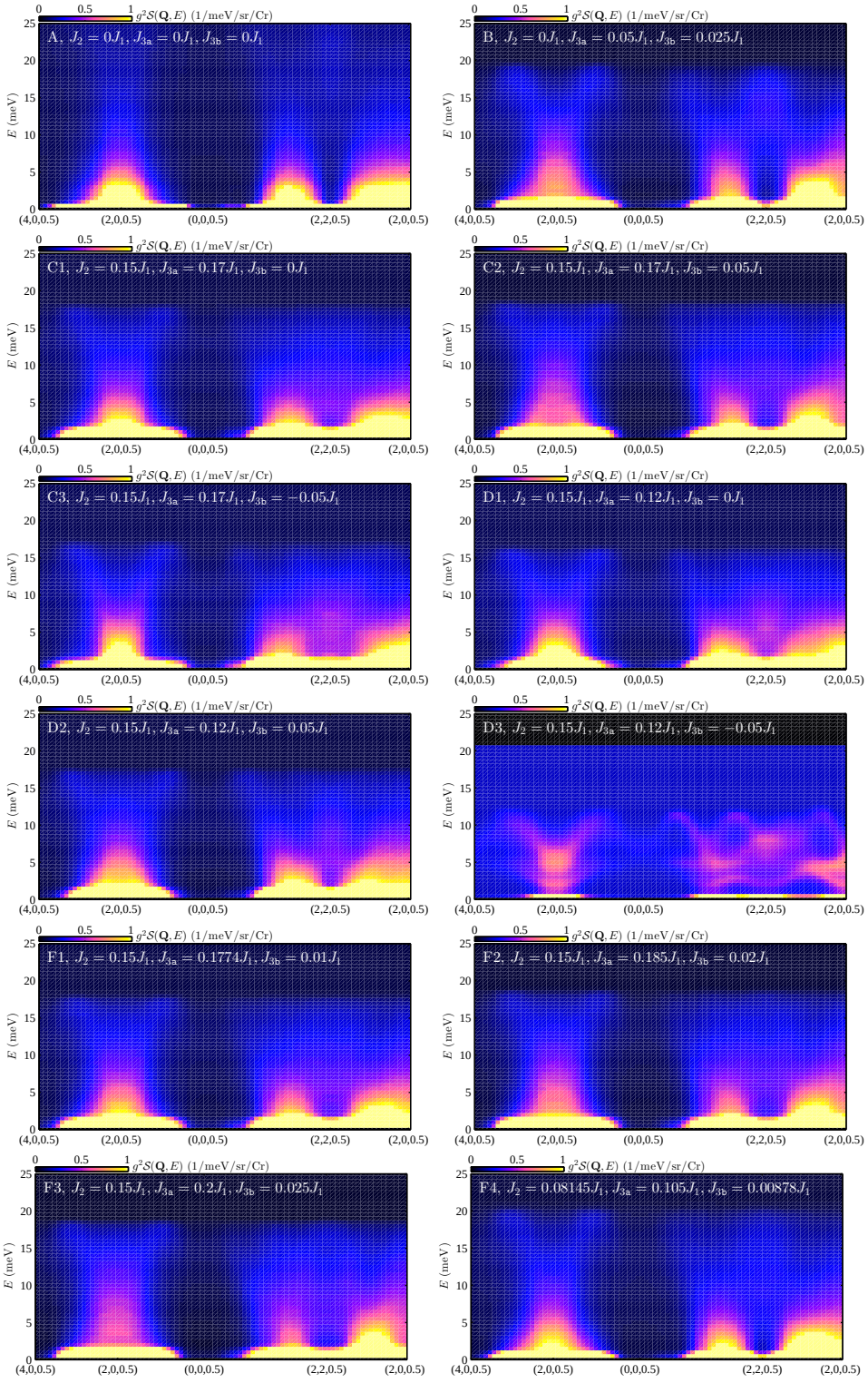

Figure 2.G.3: Calculated inelastic spectra along the path $(4, 0, 0.5) \rightarrow (2, 0, 0.5) \rightarrow (0, 0, 0.5) \rightarrow (2, 2, 0.5) \rightarrow (2, 0, 0.5)$.

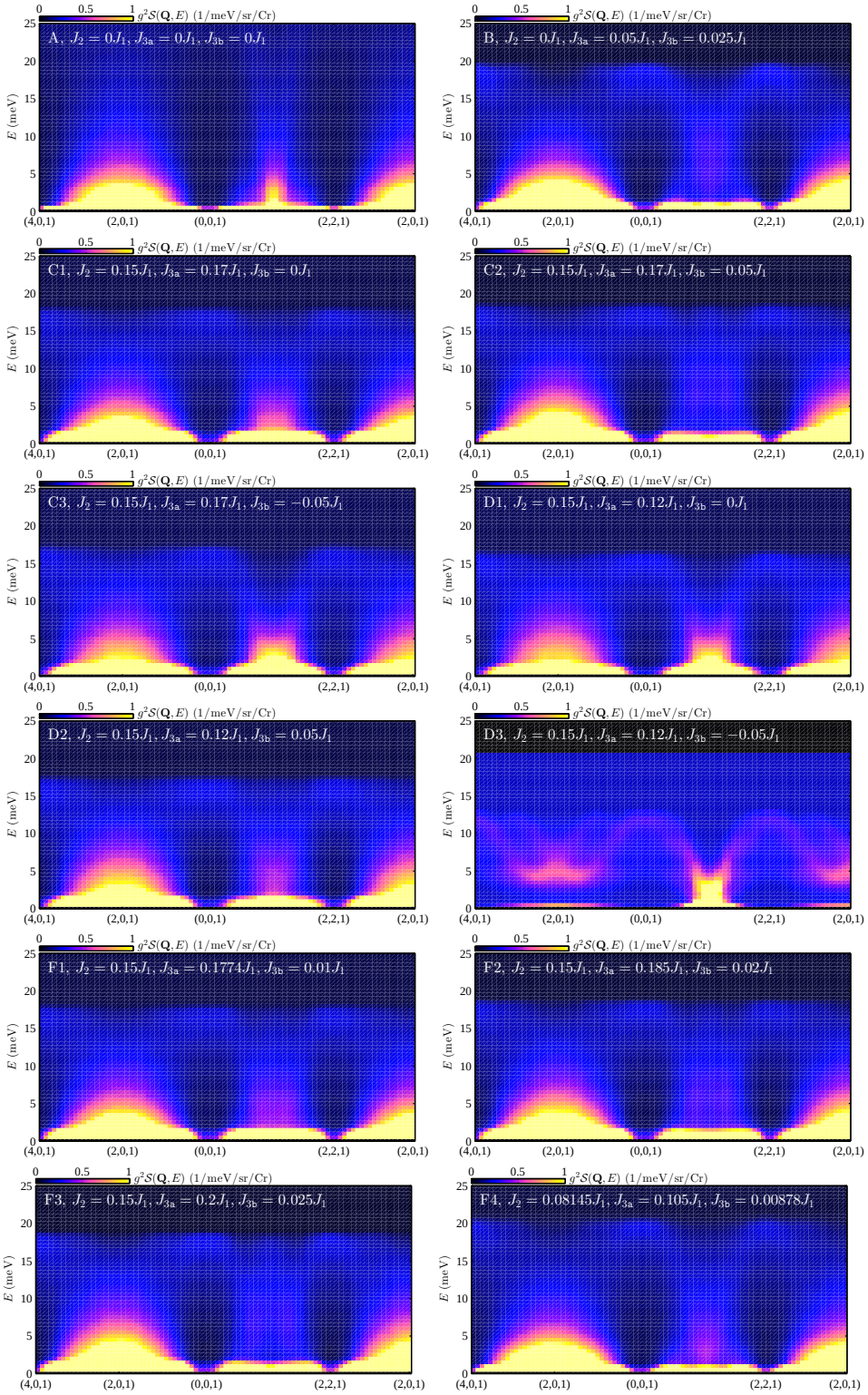

Figure 2.G.4: Calculated inelastic spectra along the path $(4, 0, 1) \to (2, 0, 1) \to (0, 0, 1) \to (2, 2, 1) \to (2, 0, 1)$.

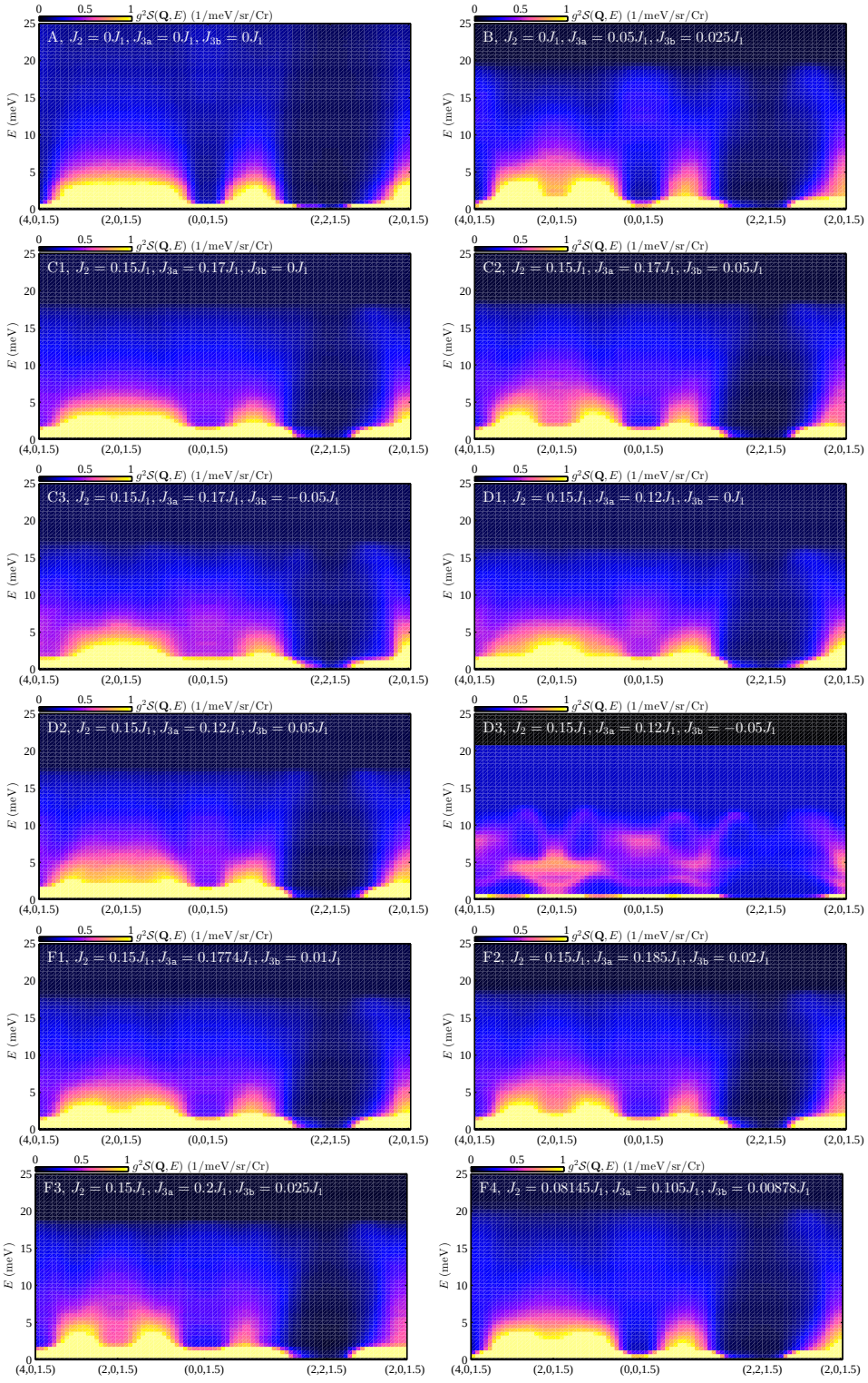

Figure 2.G.5: Calculated inelastic spectra along the path $(4, 0, 1.5) \rightarrow (2, 0, 1.5) \rightarrow (0, 0, 1.5) \rightarrow (2, 2, 1.5) \rightarrow (2, 0, 1.5)$.

2.H Mean-field calculations

The Hamiltonian is

$$\mathcal{H} = \frac{1}{2}\sum_{mn}\sum_{\mu\nu}\sum_{i}\mathcal{J}^{(i)}_{\mu\nu}(\mathbf{R}_m - \mathbf{R}_n)\mathbf{S}_{m\mu}\cdot\mathbf{S}_{n\nu} \tag{2.7}$$

where $\mathcal{J}^{(i)}_{\mu\nu}(\mathbf{R}_m - \mathbf{R}_n)$ is the exchange matrix with $i = 1, 2, 3\text{a}$ and 3b indexing the level of interactions and $\mathbf{S}_{m\nu}$ is the spin at the unit cell m and sublattice ν. The Fourier transform of the exchange matrix is given by

$$\mathcal{J}_{\mu\nu}(\mathbf{Q}) = \frac{1}{N}\sum_{i}\sum_{\mathbf{R}_m-\mathbf{R}_n}\mathcal{J}^{(i)}_{\mu\nu}(\mathbf{R}_m - \mathbf{R}_n)\, e^{\mathrm{i}\mathbf{Q}\cdot(\mathbf{R}_{m\mu}-\mathbf{R}_{n\nu})}\,. \tag{2.8}$$

where $\mathbf{R}_{m\mu} = \mathbf{R}_m + \mathbf{c}_\mu$, $\mathbf{c}_1 = (0,0,0)$, $\mathbf{c}_2 = (0, 1/4, 1/4)$, $\mathbf{c}_3 = (1/4, 0, 1/4)$ and $\mathbf{c}_4 = (1/4, 1/4, 0)$. The explicit formula can be found in [50].

For $\mathbf{Q} = 2\pi(h, 1, 0)$, the interaction matrix reduces to

$$\mathbf{J} = \begin{pmatrix} -2(J_{3\text{b}} + J_{3\text{a}})\mathbf{I}_{2\times2} & 2(J_1 - 2J_2)\mathbf{\Lambda} \\ 2(J_1 - 2J_2)\mathbf{\Lambda}^{\mathrm{T}} & -2(J_{3\text{a}} + J_{3\text{b}})\mathbf{I}_{2\times2} \end{pmatrix} \quad \mathbf{\Lambda} = \begin{pmatrix} \cos\left(\frac{h\pi}{2}\right) & -\sin\left(\frac{h\pi}{2}\right) \\ \sin\left(\frac{h\pi}{2}\right) & \cos\left(\frac{h\pi}{2}\right) \end{pmatrix} \tag{2.9}$$

which can be diagonalized by a unitary matrix

$$\mathbf{U} = \frac{1}{2}\begin{pmatrix} \mathrm{i}e^{\frac{\mathrm{i}h\pi}{2}} & -\mathrm{i}e^{-\frac{\mathrm{i}h\pi}{2}} & -\mathrm{i}e^{\frac{\mathrm{i}h\pi}{2}} & \mathrm{i}e^{-\frac{\mathrm{i}h\pi}{2}} \\ e^{\frac{\mathrm{i}h\pi}{2}} & e^{-\frac{\mathrm{i}h\pi}{2}} & -e^{\frac{\mathrm{i}h\pi}{2}} & -e^{-\frac{\mathrm{i}h\pi}{2}} \\ \mathrm{i} & -\mathrm{i} & \mathrm{i} & -\mathrm{i} \\ 1 & 1 & 1 & 1 \end{pmatrix} \tag{2.10}$$

$$\mathbf{U}\cdot\mathbf{J}\cdot\mathbf{U}^{\dagger}=\begin{pmatrix}\epsilon_{+} & 0 & 0 & 0\\ 0 & \epsilon_{+} & 0 & 0\\ 0 & 0 & \epsilon_{-} & 0\\ 0 & 0 & 0 & \epsilon_{-}\end{pmatrix},\quad \epsilon_{\pm}=\pm 2(J_1-2J_2)-2(J_{3\mathrm{a}}+J_{3\mathrm{b}}) \tag{2.11}$$

The spin configuration for minimal eigenvalue ϵ_{-} is

$$\mathbf{S}_{n\nu}=\hat{\mathbf{x}}\sin\left(\mathbf{Q}\cdot\mathbf{R}_{n\nu}+\phi_{\nu}\right)+\hat{\mathbf{y}}\cos\left(\mathbf{Q}\cdot\mathbf{R}_{n\nu}+\phi_{\nu}\right) \tag{2.12}$$

where

$$\phi_1=\frac{h\pi}{2}-\frac{\pi}{2},\quad \phi_2=\frac{h\pi}{2}+\pi,\quad \phi_3=\frac{\pi}{2},\quad \phi_4=0\,. \tag{2.13}$$

CHAPTER 3
HYBRIDIZED QUADRUPOLAR EXCITATIONS IN TRIANGULAR ISING MAGNET FEI_2

3.1 Introduction

Multipolar degrees of freedom in condensed matter systems arise naturally from anisotropic charge and magnetization distributions due to crystal electric fields (CEF) and spin-orbital coupling (SOC). The low energy physics is described in general by SU(N) effective spin models which include interactions among magnetic dipolar moments and higher order multipoles. Exotic multipolar phases can be stabilized without a symmetry-breaking ordering in the dipolar sector. Such kinds of phases are evasive to conventional probes, often referred as "hidden orders". Experimental realizations in solid state materials are rather rare, mostly confined to a handful of $4f$-electron systems. More often than not, multipolar degrees of freedom associated with SU(N) spins remain silent due to weak interactions and have little signature on low energy spectrum of materials. In this work, we present a detailed neutron-scattering study on an exceptional spin-1 system - the frustrated triangular magnet FeI_2 with dominant Ising-like single-ion anisotropy, where a surprisingly *bright* and *dipersive* band of mixed dipolar-quadrupolar character emerges from a conventional magnetic-ordered ground state and appears as the lowest-energy mode in the spectrum.

Historically, the peculiarity of this band was first noticed in far-infered spectroscopy with external magnetic fields in the 1970s [59, 60, 61]. It shows a g-factor twice as that of single-magnon bands at higher energies. This phenomenon was interpreted as forming a new type of two-magnon bound-state (TMBS) in the presence of strong Ising-like single-ion anisotropy, called the "single-ion bound state" (SIBS) [62, 63, 64]. The essential physics can be illustrated through a simple picture of ferromagnetic spin-1 chain with

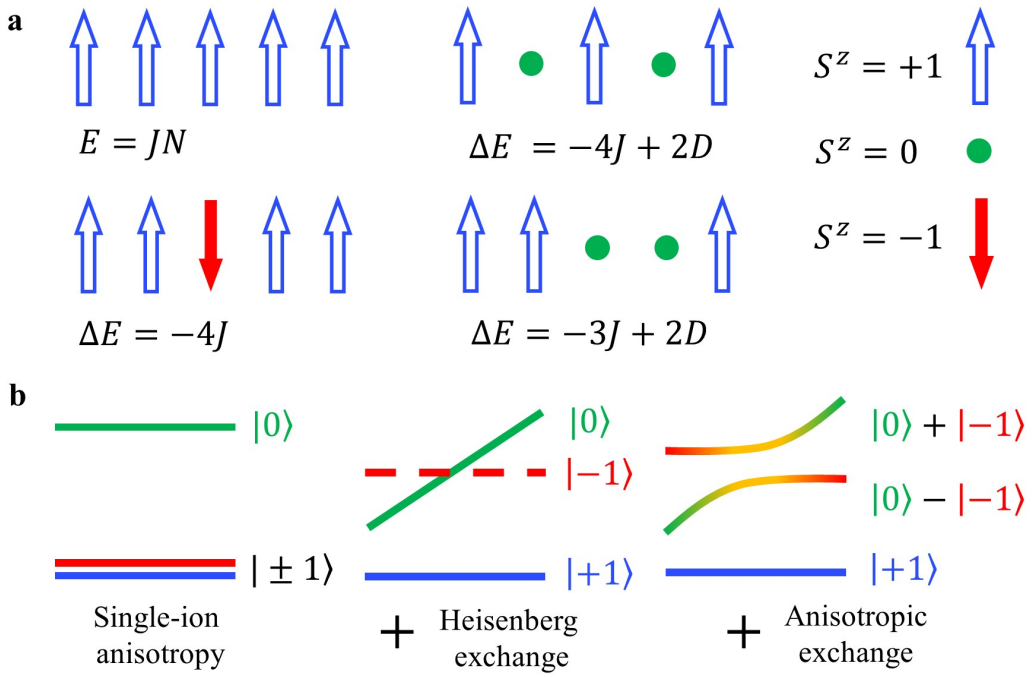

Figure 3.1: Illustration of two-magnon bound states in ferromagnetic spin-1 chain and preview of the hybridization mechanism via anisotropic exchange interactions. (a) The ground state and three types of doubly-excited states. The three local states of a spin ($S^z = +1, 0, -1$) are represented by a up-blue-arrow, green-dot and red-down-arrow, respectively. The system lowers its energy by forming bound states of two free single-spin excitations. In particular, the exchange two-magnon bound state gains (TMBS) energy of $-J$ (two adjacent green-dots) and the single-ion bound state (SIBS) gains $2D$ (one red-down-arrow). For a spin-1 system, the energy of SIBS does not depend on D, therefore remain unchanged while all the other excitations, including the single-magnon ($\Delta E = -2J + D$), are pushed up in energy if D is increased. For a sufficiently large D, the SIBS could appear as the lowest-energy mode in the spectrum. (b) The effects of different terms in the Hamiltonian on the excitation spectrum. The easy-axis single-ion anisotropy splits three degenerate local states of spin-1, giving a doubly-degenerate ground state. The Heisenberg exchange interaction induces a collective magnetic ordering at low temperature and further split the ground-state doublet. The single-magnon excitation ($|+1\rangle \rightarrow |0\rangle$) becomes dispersive and its full energy-momentum dependence can be mapped out by neutron-scattering, while the SIBS ($|+1\rangle \rightarrow |-1\rangle$) remain localized and it is invisible in the conventional experimental probes due to vanishing dipolar matrix element $\langle +1|S^{\pm}|-1\rangle = 0$. Anisotropic exchanges create a new channel of interactions mixing the single-magnon band and SIBS. A hybridization gap is opened and the SIBS gains intensity and appears dispersive in the neutron-scattering measurements.

Hamiltonian $\mathcal{H} = J\sum_{\langle i,j\rangle}\mathbf{S}_i\cdot\mathbf{S}_j - D\sum_i(S_i^z)^2$. Figure 3.1(a) shows the ground state with all spins in the $S^z = +1$ state and three types of doubly-excited states. The first type of excitation creates two excited spins in the $S^z = 0$ state on non-adjacent sites costing total energy of $-4J + 2D$. The second type puts them next to each other, therefore reduces the total energy cost by $-J$. This leads to an effective attractive interaction between excited spins, forming an exchange two-magnon bound state. The third type excites the same spin "twice" and flip its state from $S^z = +1$ to $S^z = -1$, costing total energy of $-4J$. In this case, the system effectively gains energy of $2D$ from the single-ion term by binding two free magnons on one site, hence the name "single-ion bound state". As we increase D, both single magnon and exchange bound states are pushed up in energy, while the SIBS remains unchanged and eventually becomes the lowest mode for sufficiently large D. The anomalous g-factor of SIBS can be easily understood from the fact that it is a $|\Delta S^z| = 2$ process. What's not understood until now is how such excitation evades the dipolar selection rule, not only detected in far-infred measurements, but also in triple-axis neutron scattering [65] and ESR measurements [66, 67].

Here, we resolve this puzzle conclusively four decades after its first observation, through a novel hybridization mechanism involving anisotropic exchange interactions, supported by extensive quantitative modeling of single-crystal inelastic neutron-scattering data from modern state-of-art instruments. For a spin-1 system, local physical observables are represented by 3×3 hermitian matrices, eight independent operators in total, $T_{a=1,\cdots,8} = \{S^x, S^y, S^z, \tilde{\mathcal{O}}_{22}, \tilde{\mathcal{O}}_{21}, \mathcal{O}_{20}, \mathcal{O}_{21}, \mathcal{O}_{22}\}$. First three are dipolar operators and the remaining five are quadrupolar operators. They are the eight generators of SU(3) group and satisfy the commutation relation $[T_a, T_b] = if_{abc}T_c$, where f_{abc} are the SU(3) structure constants. Instead of thinking SIBS as a higher order process by applying the dipolar operator S^- twice on the same site, we should view this as an excitation associated with quadrupolar operators $\mathcal{O}_{22} = \left((S^+)^2 + (S^-)^2\right)/2$ and $\tilde{\mathcal{O}}_{22} = -i\left((S^+)^2 - (S^-)^2\right)/2$. In addition, the single ion term $-D\left(S_i^z\right)^2$ is related to the quadrupolar component $\mathcal{O}_{20}$ up to a constant. Fig.

3.1(b) illustrates the changes of spectrum by successively introducing the Ising-like single-ion anisotropy, Heisenberg and anisotropic exchange interactions. The energetics in FeI_2 is fortuitous such that the dipolar excitation ($|+1\rangle \rightarrow |0\rangle$) overlaps with the quadrupolar excitation ($|+1\rangle \rightarrow |-1\rangle$). We treat them on the equal footing using generalized spin-wave theory (GSWT) and show that the anisotropy exchanges enabled by spin-orbital coupling mixes these two channels, opens a hybridization gap in the spectrum and renders the dark and flat SIBS *bright* and *dispersive* as observed in experiments. This is a genuine quantum-mechanical effect arises from a classical long-range order magnet with negligible longitudinal fluctuations.

FeI_2 crystallizes in the trigonal space group $P\bar{3}m1$ with lattice constants $a = 4.05$ Å and $c = 6.75$ Å at room temperature, Figure 3.2(a). Magnetic Fe^{2+} ions form structurally perfect triangular-lattice layers. The electronic ground state of free Fe^{2+} ion is labeled ^5D corresponding to a total spin $S = 2$ and a total orbital angular moment $L = 2$ [68]. In the crystal environment of FeI_2, Fe^{2+} ions are in octahedral coordination of iodine atoms with weak trigonal distortion, lowering the site-symmetry from $m\bar{3}m$ to $\bar{3}m$, Figure 3.1(b). Relevant low-energy degrees of freedom can be identified through a series of approximations, Figure 3.1(c). The leading-order cubic crystal field splits the five degenerate d-orbitals into a ground-state triplet (T_{2g}) and a excited-state doublet (E_g) with a gap on the order of 100 meV. This is much larger than the subleading spin-orbital coupling ($\sim$10 meV) and trigonal crystal field ($\sim$1 meV), therefore it's good approximation to neglect the contribution of E_g orbitals and work in the terms of an effective orbital angular moment $l = 1$ [69, 70]. The spin-orbital coupling further splits the remaining 15 levels ($(2S+1)\times(2l+1)$) into three multiplets labeled by the total angular moment $J = 1, 2$ and 3. Figure 3.2(d) shows energy-resolved neutron-scattering intensity along a high-symmetry path in the $(h, k, 0)$-plane collected at 11 K in the paramagnetic phase. It reveals two broad bands of inter-multiplet transitions from $J = 1$ to $J = 2$, centered around 25 and 35 meV. The low energy magnetic fluctuations within the ground-state multiplet are confined below 10 meV, which

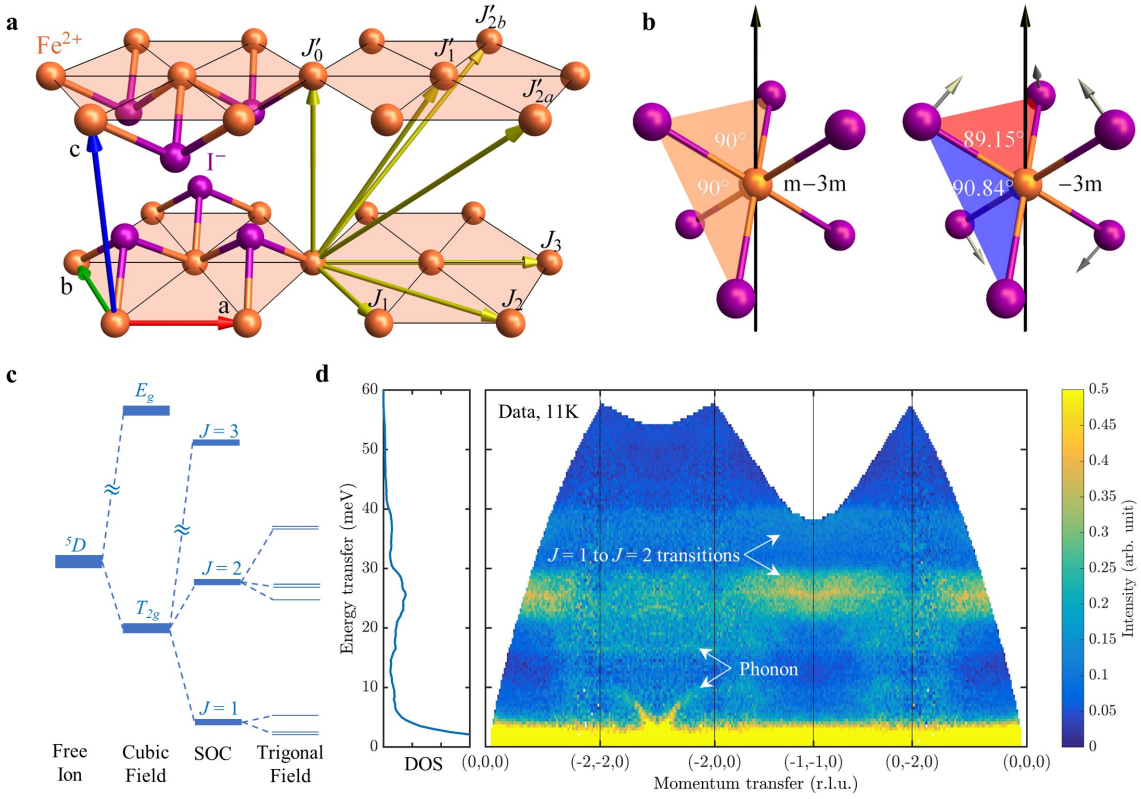

Figure 3.2: Structure, exchange pathways and single-ion properties of FeI_2 and an overview of the full inelastic neutron spectrum. (a) Crystal structure and interaction pathways of FeI_2, showing triangular layers of Fe^{2+} ions (orange spheres) and their binding with iodine atoms (purple spheres). (b) The local environment of Fe^{2+} ions, showing a perfect octahedral coordination by iodine atoms with $m\bar{3}m$ symmetry (left) and the weakly trigonal-distorted environment in FeI_2 with $\bar{3}m$ symmetry (right). White arrows indicate the direction of distortion. (c) Single-ion level diagram of the FeI^{2+} ion in FeI_2, showing a hierarchy of interaction energy scales including the dominant cubic crystal field ($\sim$1 eV), subleading spin-orbital coupling ($\sim$10 meV) and trigonal crystal field ($\sim$1 meV). (d) Energy dependence of the dynamical responses of Fe_2 along a high-symmetry path in the momentum space, showing inter-multiplet transitions at high energies, phonons from lattice dynamics at intermediate energies and magnetic fluctuations within $J = 1$ multiplet at low energies. The data is collected at 11 K with incoming neutron energy of 65 meV on SEQUOIA. To the left, it shows a momentum-integrated spectrum in general accordance with the single-ion diagram.

can be described using an effective spin-1 model. In this language, the trigonal crystal field is mapped to a Ising-like single-ion anisotropy term $-D(S^z)^2$ [70]. The strength of the single-ion parameter D is estimated to be 22 K from susceptibility measurement on single crystals [71] and 26 K from Mössbauer study of Fe^{2+} ion on powder samples [69], an order of magnitude larger than the estimated exchange energy scale ($\sim$2 K) [61].

3.2 Methods

Sample preparation. Small single-crystal samples of FeI_2 were grown in evacuated quartz tubes from pure elements using chemical vaper transport technique with the hot end at 570°C and the cold end at room temperature [72]. As-grown FeI_2 crystals appear as thin black flakes, very easy to bent and cut. Due to the highly hygroscopic nature, all samples are handled in glovebox with water contain less than 5ppm. Small crystals were collected and sealed in quartz tubes under vacuum. Large single crystals up to 3g were grown by slowly passing through the floating zone furnace at alleviated temperatures.

X-ray diffraction measurements and refinements. Room-temperature powder X-ray diffraction (XRD) were carried out on crushed single-crystal samples using an Empyrean diffractometer with 50% of each Cu-$K\alpha_1$ and Cu-$K\alpha_2$ radiations. FeI_2 sample is highly hydroscopic and degrades within a few seconds exposing to air. We loaded our samples in a domed holder to keep it from degrading during the measurement. The holder was rotating with 16 RPM in attempt to reduce the preferred orientations. Measurement were taken between $8 \leq 2\theta \leq 100^\circ$ with $\Delta 2\theta = 0.013^\circ$. Rietveld refinement was carried out using the FULLPROF program [6]. Peak-shapes were modeled by pseudo-Voigt functions convoluted with asymmetry due to axial divergence, and the preferred orientation was treated with usual Rietveld function. Fits to data are shown in Fig. 3.A.1, and refined values of structural parameters are given in Tab. 3.A.1.

Neutron scattering measurements. Inelastic neutron-scattering experiments were performed on the SEQUOIA time-of-flight spectrometer at the Spallation Neutron Source (SNS), Oak Ridge National Laboratory (ORNL), USA [73, 74]. The sample was a $\sim$2.5 g slab crystal sealed in aluminum foil and mounted in the $(h, k, 0)$ scattering plane on an aluminum holder. The alignment of the mount was checked and adjusted on CG-1B at the High Flux

Isotope Reactor (HFIR) of ORNL. The sample holder was attached to the bottom of a sample stick inserted in an Orange Cryostat reaching a base temperature of 1.8 K. Measurements were performed at 1.8 K with $E_i = 12$, 65 and 80 meV, at 8K with $E_i = 12$meV and at 11 K with $E_i = 12$ and 65 meV. The sample was rotated in a step of 0.5° with a range of 200° for $E_i = 12$ at 1.8 K, and in a step of 1° with the same range for all the other configurations.

Elastic neutron-scattering experiments were performed on the CORELLI spectrometer at SNS of ORNL. A thin-flake sample of 0.4 g was sealed in aluminum foil mounted on an aluminum holder and attached to the bottom of a sample stick. The stick is inserted in a 8 T superconducting cryomagnet and an Orange Cryostat reaching a base temperature of 1.8 K. The sample is rotated in a step of 3° with a range of 82°. The zero-field data is shown in Fig. 3.3(b).

Data analysis. Initial data reduction was performed in MANTID for both SEQUOIA and CORELLI datasets. Subsequent analysis of the SEQUOIA data was performed in HORACE [44] on a dedicated node within Georgia Tech's Partnership for Advanced Computing infrastructure.

3.3 Modeling of energy-integrated data

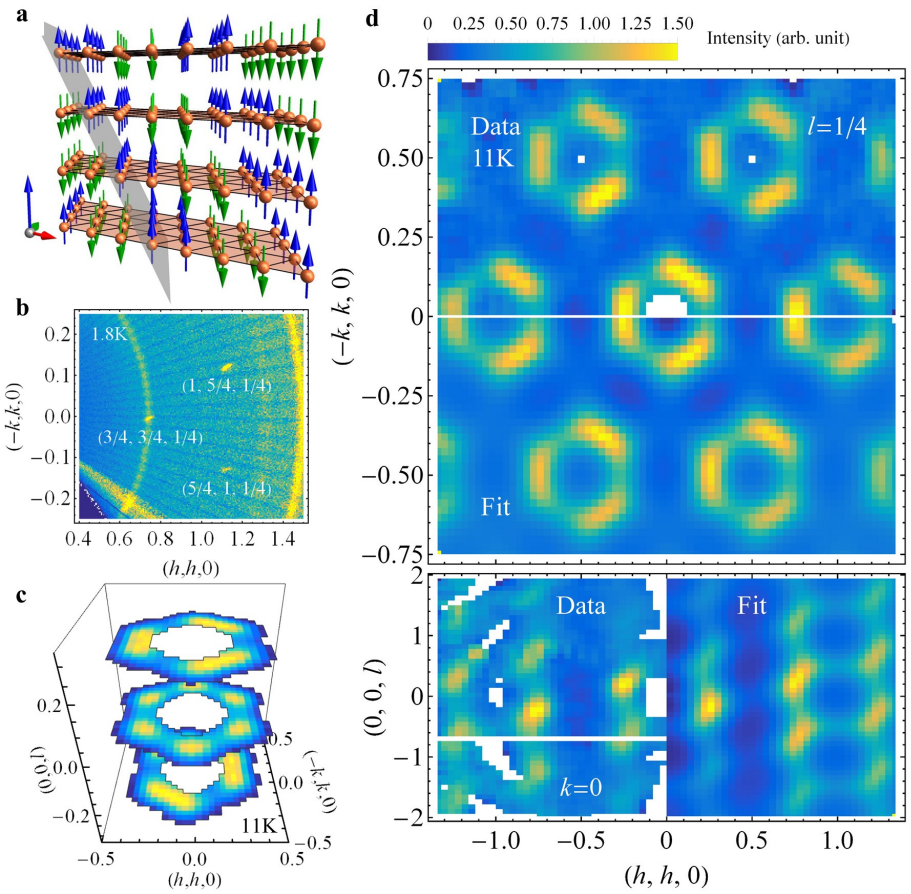

Figure 3.3: Magnetic Bragg peaks and paramagnetic neutron-scattering data of FeI_2. (a) Magnetic structure of FeI_2, showing a stacking of ferromagnetic plane (gray) in a up-up-down-down (blue-blue-green-green) sequence. (b) Elastic neutron-scattering data collected at 1.8 K on CORELLI, showing magnetic Bragg peaks from three equivalent magnetic domains related by 120° rotations. (c) Focused 3D overview of diffuse-scattering data collected at 11 K on SEQUOIA by integrating over energy transfer from 0 to 6 meV, showing intensity patterns consistent with the $m\bar{3}m$ Laue symmetry. (d) Extended diffuse-scattering data in the $(h, k, 0)$-plane at $l = 1/4$ and SCGA fits using the Heisenberg model (top); the same comparison for in the (h, h, l)-plane at $k = 0$.

A strong first-order magnetic phase transition occurs around 9.5K in FeI_2 [75]. No concurrent structural distortion was observed in powder neutron diffraction data [76]. A collinear structure with magnetic moments oriented along c-axis is stabilized in the ordered phase [76, 77, 78], featuring a up-up-down-down stripe configuration in the ab-plane, Figure 3.3(a). The stripe pattern successively shifts one lattice constant along a-axis while moving up one layer and repeats after four layers, corresponding to a propagation vector $\mathbf{k} = (1/4, 0, 1/4)$. Another two equivalent k-domains also exist in the material related by 120 degree rotation, Figure 3.3(b). This structure is similar to that of $MnBr_2$, [79] where the moments are aligned in the ab-plane instead of along c-axis. Upon applying magnetic fields along c-axis, four different phases emerge before reaching saturation at 12.5T [80]. Although detailed single-crystal neutron diffraction was performed to investigate magnetic structures of all four phases [77], some of them were not determined with high confidence [81].

The first step towards understanding the exotic excitations in FeI_2 is constructing a minimal model which realizes the observed magnetic structure at low temperatures. To this end, we introduce three intra-plane coupling $\{J_1, J_2, J_3\}$ and four inter-plane couplings $\{J_0^{'}, J_1^{'}, J_{2a}^{'}, J_{2b}^{'}\}$ in our model, Figure 3.2(a). Due to the dominant easy-axis single-ion anisotropy, it suffices to just consider a Ising model $\mathcal{H} = \sum_{(i,j)} J_{ij} S_i^z S_j^z$ in finding the energetic constraints among various couplings for the desired magnetic ground state. It was shown that the in-plane up-up-down-down stripe ordering can be stabilized with competing nearest and further neighbor interactions in the Ising model satisfying following conditions [82]

$$J_1 < 0\,(\text{ferro}), \quad J_2 > 0\,(\text{antiferro}), \quad J_1 - 2J_3 < 0 \quad \text{and} \quad J_1 + 2J_2 + 2J_3 > 0. \tag{3.1}$$

To select the experimentally observed 3D stacking pattern, we find two more constraints for inter-plane couplings by enumerating the energy of all possible stacking sequence with

periodicity less than or equal to four,

$$J_{2a}^{'} > 0\,(\text{antiferro}), \quad \text{and} \quad -J_{2a}^{'} < J_0^{'} + 2J_1^{'} < 3J_{2a}^{'}\,, \tag{3.2}$$

see Section 3.D for more details. It is important to realize $J_{2a}^{'}$ and $J_{2b}^{'}$ couplings are symmetry-inequivalent despite having the same bond length. The $J_{2a}^{'}$ bond has an almost 180 degree Fe^{2+}-I^{-}-I^{-}-Fe^{2+} bridge, while atoms connected by the $J_{2b}^{'}$ bond does not have any plausible pathway between them, therefore we assume $J_{2b}^{'}$ being zero from here on. The energy of the SIBS excitation in the Ising model is given by $4(-J_1 + J_2 + J_3 + 2J_{2a}^{'})$, corresponding to flipping the spin on a single site.

To further determine the interaction strengths, we upgrade to a Heisenberg model $\mathcal{H} = \sum_{(i,j)} J_{ij}\mathbf{S}_i \cdot \mathbf{S}_j - D\sum_i (S_i^z)^2$ and employ self-consistent Gaussain approximation (SCGA) [12] for conducting a global fit to the diffuse scattering data collected at 11 K in the paramagnetic phase. This approach has proven to be very successful in extracting microscopic models for frustrated systems [83]. We use experimentally observed SIBS energy of $\sim$2.8 meV as a separate constraint for the exchange parameters in the fitting. Figure 3.3(c) gives an overview of our diffuse scattering data revealing highly structured patterns consistent with the $\bar{3}m$ Laue symmetry. A decent global fit to the entire data set is achieved and good agreements in both in-plane and out-of-plane cuts are demonstrated in Figure 3.3(d). The best fitting parameters (Table 3.A.1) satisfy all the constraints mentioned earlier. Notably, the magnitude of the nearest neighbor coupling ($J_1 = -2.74$ K) is comparable to the second ($J_2 = 1.31$ K) and third neighbor coupling ($J_3 = 2.46$ K). This is primarily resulting from a cancellation of ferromagnetic direct exchange and antiferromagnetic superexchange [84].

3.4 Modeling of energy-resolved data

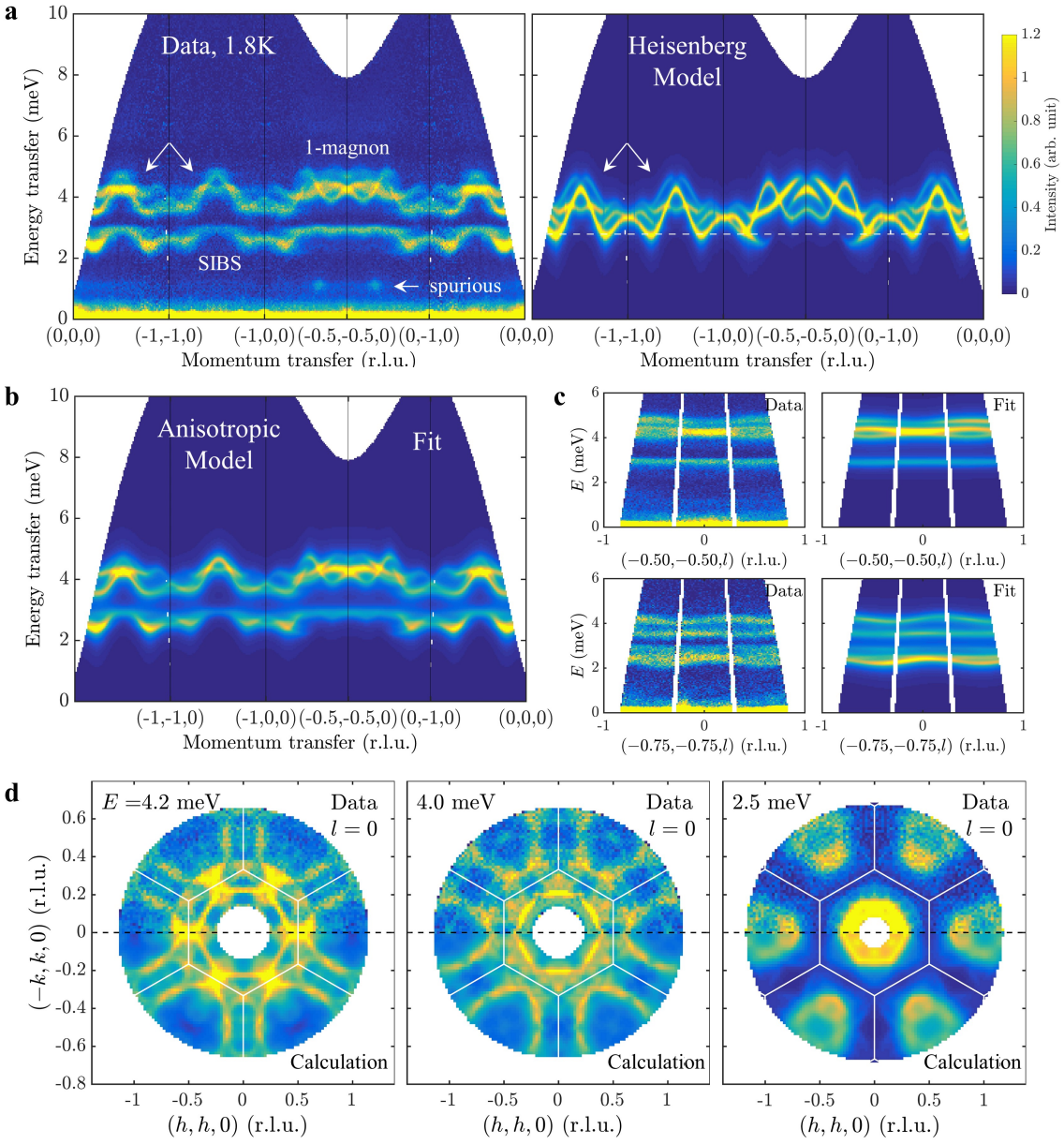

Figure 3.4: Low-temperature inelastic neutron-scattering data of FeI_2 and GSWT fits using the anisotropic model. (a) Energy dependence of collective magnetic excitations of FeI_2 collected at 1.8 K on SEQUOIA along a high-symmetry path in the momentum space (left), showing a single-magnon band with several overlapping branches and a gaped single-ion bound state of equally bright intensity and strongly dispersive features. Calculated spin-wave spectrum using best fitting parameters of diffuse-scattering data (right), showing that only the single-magnon band is qualitatively captured. White dashed line indicates the energy of SIBS. The white arrows indicate symmetry equivalent positions in the reciprocal space with large disparity in intensity in the data, which can not be explained by a Heisenberg model with the Fe^{2+} form factor. (b) General spin-wave theory fitting of the inelastic spectrum using the anisotropic model, showing that all the details of both the single-magnon and SIBS are reproduced. (c) The comparison between the data and GSWT fitting for cuts in the out-of-plane direction. (d) Wave-vector dependence of magnetic excitations at selected energies (top panels) and GSWT calculations (bottom panels) using the best fitting parameters of the anisotropic model. Excellent agreements are achieved for cuts in the single-magnon band (4.2 and 4.0 meV) and in SIBS (2.5 meV).

From this Heisenberg model, we calculate the inelastic spectrum in the ordered phase using linear spin-wave theory (LST) and compare it with our neutron-scattering data in Figure 3.4(a). Despite the overall resemblance, this model fails in several important aspects. First of all, we see two separate bands in the data, corresponding to the single-magnon band and the single-ion bound state. The latter is completely missing in the LST calculation. This is certainly expected, because it ignores the quadrupolar degrees of freedom associated with SU(3) spins from the beginning. The white dashed line in LST panel of Figure 3.4(a) indicates the SIBS energy that we put as constraint in the SCGA fitting. Interestingly, it overlaps with the spin-wave spectrum computed from the best fitting parameters. To make further progress, we need to invoke more advanced tools. In the spin-wave theory of SU(2) spins, bound states are complicated objects involving summing over infinite orders in the $1/S$ expansion or solving difficult integral equations. Instead, we employ generalized spin-wave theory (GSWT) and faithfully represent the local states of SU(3) spins using Schwinger bosons [85],

$$|m\rangle_i = b^\dagger_{i,m}|\text{vac}\rangle_i, \quad m = +1, 0, -1 \tag{3.3}$$

with constraint $\sum_m b^\dagger_{i,m} b_{i,m} = 1$, where i labels the site in the lattice. In a magnetically ordered ground state where $b^\dagger_{i,\uparrow}$ boson forms a Bose-Einstein condensate, $b_{i,0}$ boson creates a single-magnon of dipolar character with quantum spin number $|\Delta S^z| = 1$, while $b_{i,\downarrow}$ boson creates a SIBS of quadrupolar character with $|\Delta S^z| = 2$. This approach allow us to treat both dipolar and quadrupolar excitations on the equal footing and study their interplay by diagonalizing a Hamiltonian truncated at the quadratic order. However, having this tool is not enough. For a Heisenberg model, GSWT predicts the single-magnon and SIBS decouple at linear level in our system. They would pass through each other without any interference and SIBS would still remain invisible in neutron-scattering experiments. This is not what we observed in the data. Figure 3.4(a) shows that not only the SIBS appears as bright as the one-magnon branch, but also dispersive wherever the single-magnon gets close, as if it were "pushed down" in energy by the single-magnon band to avoid crossing.

The hint to this puzzle comes from an anomalously strong intensity difference between $(-0.5, -0.5, 0)$ and $(-1, -0.5, 0)$ at 4.2 meV in the one-magnon branch, indicated by white arrows in Figure 3.4(a). These two points are related by the $\bar{3}m$ Laue symmetry and a reciprocal lattice vector. As expected, the intensity at $(-1, -0.5, 0)$ is only marginally weaker than $(-0.5, -0.5, 0)$ in the LST calculation of the Heisenberg model due to the Fe^{2+} form factor. Yet, they differ strongly in the data as demonstrated in Figure 3.4(d). This phenomenon results from a combined effect of anisotropic interaction and neutron dipole factor. Through symmetry analysis, we find four independent exchange parameters for nearest neighbor bonds, $\{J_1^{\pm}, J_1^{zz}, J_1^{\pm\pm}, J_1^{z\pm}\}$, see SectionS8 for details,

$$\begin{aligned}\mathcal{H}_{\text{NN}} = \sum_{\langle i,j \rangle} \big[& J_1^{zz} S_i^z S_j^z + J_1^{\pm} \left(S_i^+ S_j^- + S_i^- S_j^+ \right) + J_1^{\pm\pm} \left(\gamma_{ij} S_i^+ S_j^+ + \gamma_{ij}^* S_i^- S_j^- \right) \\ & - \frac{i J_1^{z\pm}}{2} \left((\gamma_{ij}^* S_i^+ - \gamma_{ij} S_i^-) S_j^z + S_i^z (\gamma_{ij}^* S_j^+ - \gamma_{ij} S_j^-) \right) \big] , \end{aligned} \tag{3.4}$$

where γ_{ij} are bond-dependent phase factors. This piece of the Hamiltonian is in fact the same as the well-known triangular-lattice compound $YbMgGaO_4$. Similar intensity mod-

ulation was also noted in the diffuse scattering data of $YbMgGaO_4$ [86]. For a minimal model, we include all anisotropic exchange parameters for NN bonds, but only consider two parameters $\{J^{\pm}, J^{zz}\}$ for each of the other five bonds. There are 15 parameters in total including the single-ion anisotropy. We perform a pixel-to-pixel fitting using GSWT to a high-symmetry path in $(h, k, 0)$-plane and selected cuts in the out-of-plane direction, and use the rest of the data as a check for our model. The fit works remarkably well for all the slices involved as shown in Figure 3.2(b), 2(c) and Figure 3.G.3. We further compute constant energy cuts from best fitting parameters (Table 3.E.1) and compare with the data in Figure 3.2(d). The agreement is astonishingly good for all energies. We find that large off-diagonal exchanges are required to account for the intricate details observed in the data, $J_1^{\pm} = -2.770(19)$ K, $J_1^{zz} = -2.461(895)$ K, $J_1^{\pm\pm} = -2.019(10)$ K, $J_1^{z\pm} = -3.017(6)$ K. See Sections 3.H for fitting details.

3.5 Discussion

What do we learn from this anisotropic model of FeI_2? First, the $J_1^{z\pm}$ term plays the key role of *hybridizing* the overlapping single-magnon and SIBS bands, and opening a gap. In the SU(3) Schwinger boson representation, $S_i^z S_j^+$ is replaced by $\sim \left(b_{i,-1}^\dagger b_{i,0} + b_{j,-1}^\dagger b_{j,0} \right)$ at the quadratic order, given spins at site i and j both in the ground state of $S^z = +1$. This introduces an on-site coupling through annihilating a single-magnon by $b_{i,0}$ and subsequent creating a SIBS by $b_{i,-1}^\dagger$. Through this coupling, both excitations acquire a mixed dipolar-quadupolar character, which is best illustrated in Figure 3.E.1(b). The relative weight of $b_{i,-1}^\dagger$ and b_{i0} in the eigen-modes varies with energy. The closer it is to the gap, the more quadrupolar character it gets. The intensely bright and strongly dispersive piece of SIBS is in fact part of the single-magnon band if the hybridization were absent. Second, our fitting result suggests a subtle correction to the up-up-down-down magnetic ground state. Instead of orienting purely along c-axis, we find spins tilting roughly 10° away from it, Figure 3.G.1(a), while remaining collinear. The ground state is nevertheless very close to a SU(2) coherent state where the dipole moment length is maximal $| \langle \mathbf{S} \rangle | = 1$, as shown in Figure 3.E.1(a). That is to say, the ground state of FeI_2 is a conventional long-range ordered state with negligible quadrupolar contribution. The hybridization of single magnon and SIBS observed in the spectrum of FeI_2 is a quantum-mechanical phenomenon occurred predominantly in the transverse channel. This is in nice contrast with $CsFeCl_3$ where the single-ion anisotropy is easy-plane type rather than easy-axis [87]. A different type of hybridization was found between longitudinal and transverse fluctuations in the pressure-induced ordered phase [88].

Last but not least, FeI_2 along with $Ba_2CoGe_2O_7$ [89], $Sr_2CoGe_2O_7$ [90], $NiCl_2$-4SC$(NH_2)_2$ [91] and $CsFeCl_3$ are the only few $3d$-compounds, to the best of our knowledge, where excitations with multipolar characters have been conclusively detected. Magnetic ions in these compounds are well-known to have partially-quenched orbital degrees of freedom,

which have potential of creating large single-ion anisotropies. FeI_2 stands out as the only one has the easy-axis type, and all the others have the easy-plane type. The most important implication of our work is perhaps that systems of large-spin with Ising anisotropy are not to be shunned away from detailed studies for lacking of quantum effects. The dipolar-quadrupolar hybridization via anisotropic exchanges in FeI_2 is a genuine non-perturbative quantum-mechanical phenomenon. It is fortuitous that excitations of different characters overlap in FeI_2 which facilitates the strong hybridization, but it is quite feasible to tune the spectra using magnetic field or pressure to promote detection of multipolar excitations in many more large-spin systems.

APPENDIX

3.A Powder X-ray diffraction measurements

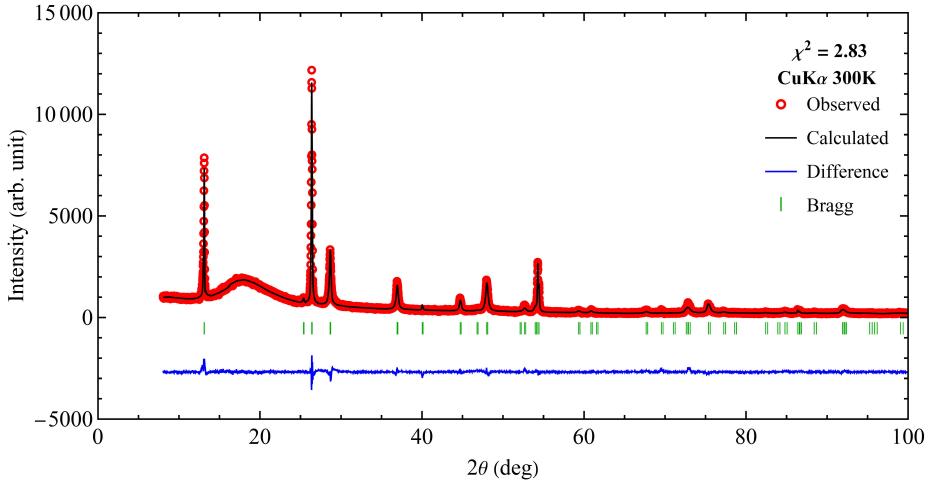

Figure 3.A.1: Room-temperature X-ray diffraction patterns of crushed single-crystals measured in a domed sample holder spinning at 16 RPM. The broad peak at $2\theta \sim 20^\circ$ is the background from the polycarbonate dome which keeps the sample from degrading during the measurement. Strong preferred orientation is present in the crushed crystals.

Table 3.A.1: Structural parameters determined from Rietveld refinement of powder X-ray diffraction data.

FeI_2, $P\bar{3}m1$

Radiation	50%, Cu $K\alpha_1$, $\lambda = 1.540598$ Å 50%, Cu $K\alpha_2$, $\lambda = 1.544426$ Å				
T	300 K				
Lattice parameters	$a = b = 4.05012$ Å, $c = 6.75214$ Å				
B_{iso}	1.4032 Å^2				
Atom	x	y	z	Occ.	Site
Fe	0.00000	0.00000	0.00000	1.000	1a
I	0.33333	0.66667	0.25000	1.000	2d

Room-temperature powder X-ray diffraction (XRD) were carried out on crushed single-crystal samples using an Empyrean diffractometer with 50% of each Cu-$K\alpha_1$ and Cu-$K\alpha_2$

radiations. FeI_2 sample is highly hydroscopic and degrades within a few seconds exposing to air. We loaded our samples in a domed holder to keep it from degrading during the measurement. The holder was rotating with 16 RPM in attempt to reduce the preferred orientations. Measurement were taken between $8 \leq 2\theta \leq 100^\circ$ with $\Delta 2\theta = 0.013^\circ$. Rietveld refinement was carried out using the FULLPROF program [6]. Peak-shapes were modeled by pseudo-Voigt functions convoluted with asymmetry due to axial divergence, and the preferred orientation was treated with usual Rietveld function. Fits to data are shown in Figure 3.A.1, and refined values of structural parameters are given in Table 3.A.1.

3.B Data symmetrization

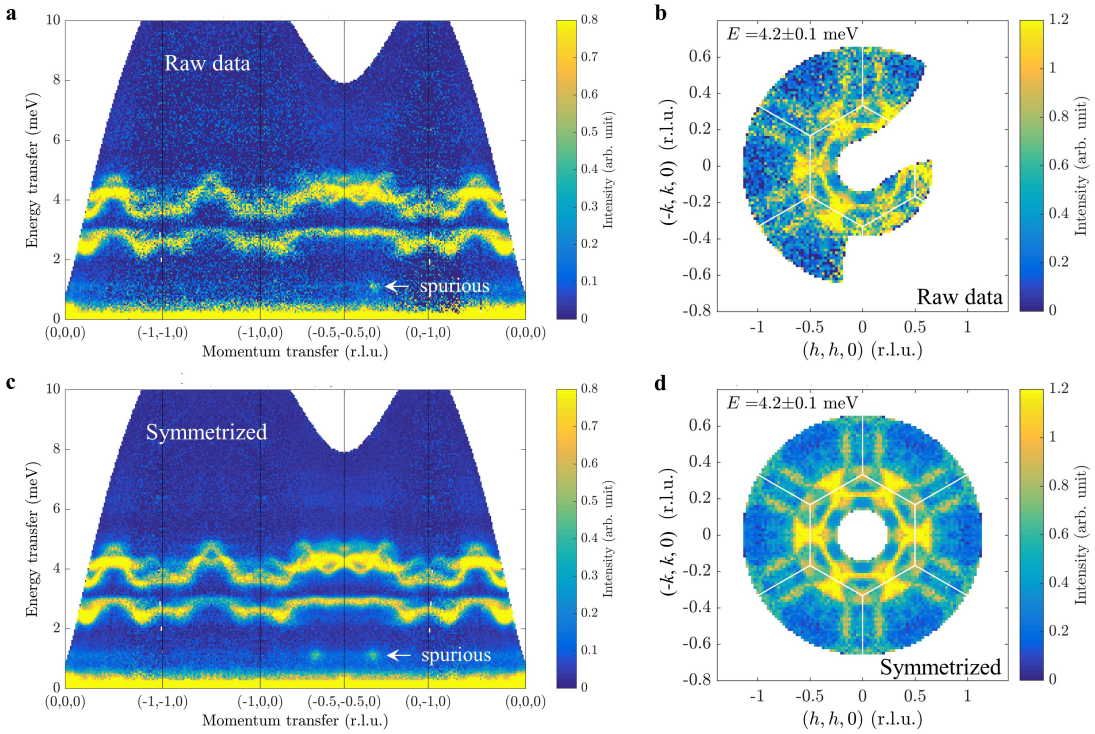

Figure 3.B.1: Comparison between the raw data ((a), (b)) and the symmetrized data ((c), (d)). The white lines are Brillouin zone boundaries of triangular lattice.

We can gain several factors more statistics by exploiting the $\bar{3}m$ Laue symmetry of system to symmetrize the raw neutron scattering data. Elements of symmetry operation are tabulated on the Bilbao crystallographic server under "General Positions of three-dimensional crystallographic point groups" [92]. There are three different coordinate systems for $\bar{3}m$ point group: "-31m hexagonal axes", "-3m1 hexagonal axes" and "-3m rhombohedral axes". Group elements in "-3m1 hexagonal axes" agree with those in the International Tables for Crystallography, which has its origin at the center of the unit-cell. The "-31m hexagonal axes" with origin at the corner of the unit-cell is what we need for the symmetrization process working in the environment of Horace [44]. The data is stored in the global Cartesian frame in Horace, so we need to transform it to the fractional coordinate before applying the symmetry operations. These group elements are written for a unit-cell

with $\gamma = 120^{\circ}$, so this will also be our convention for the unit-cell in the reciprocal space in presenting the data, see Figure 3.G.2. In the ordered phase, there are three magnetic domains related by 120° rotation with somewhat different populations. The symmetrization process averages over all three domains.

3.C Elastic cuts of neutron-scattering data

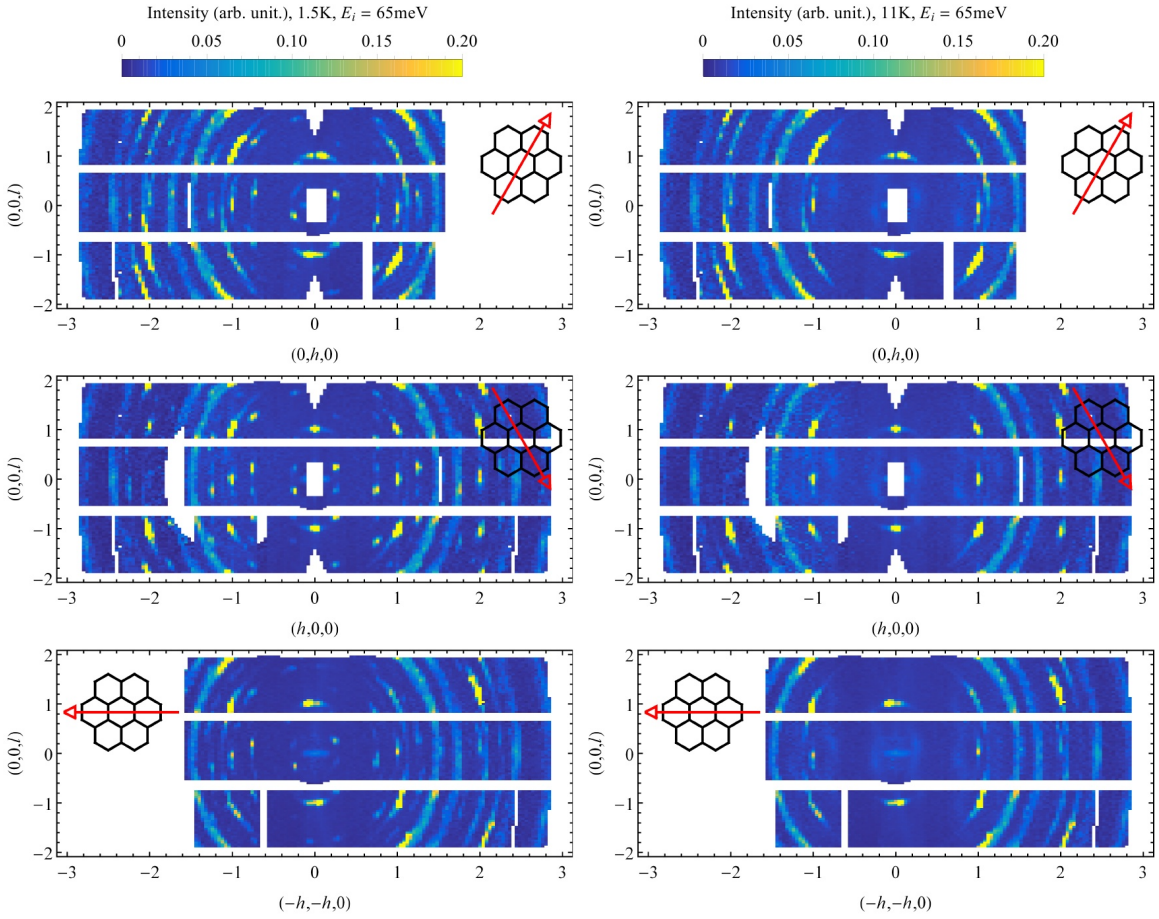

Figure 3.C.1: Elastic cuts of neutron-scattering raw data collected at 1.5K (left) and 11K (right) with incoming energy of 65meV. Three symmetry-equivalent cuts related by 120° rotation are shown for each dataset. The ring-like signals are from aluminum sample holder. Intensities at $(1, 0, 1)$ and equivalent positions are coming from structural domains which are 60° rotation from majority of the crystal. The fraction of minority domains estimated from integrated intensities is less than a few percent. Positions of magnetic Bragg peaks are consistent with reported propagation vectors $\mathbf{k} = (1/4, 0, 1/4), (0, 1/4, 1/4)$ and $(-1/4, -1/4, 1/4)$ [77], corresponding to three magnetic domains of the stripe ordering related by 120 degree rotation. The weak signals at $(1/4, 0, -1/4)$ and related positions are the magnetic Bragg peaks from the minority structural domains.

3.D Ground-state constraints of exchange parameters

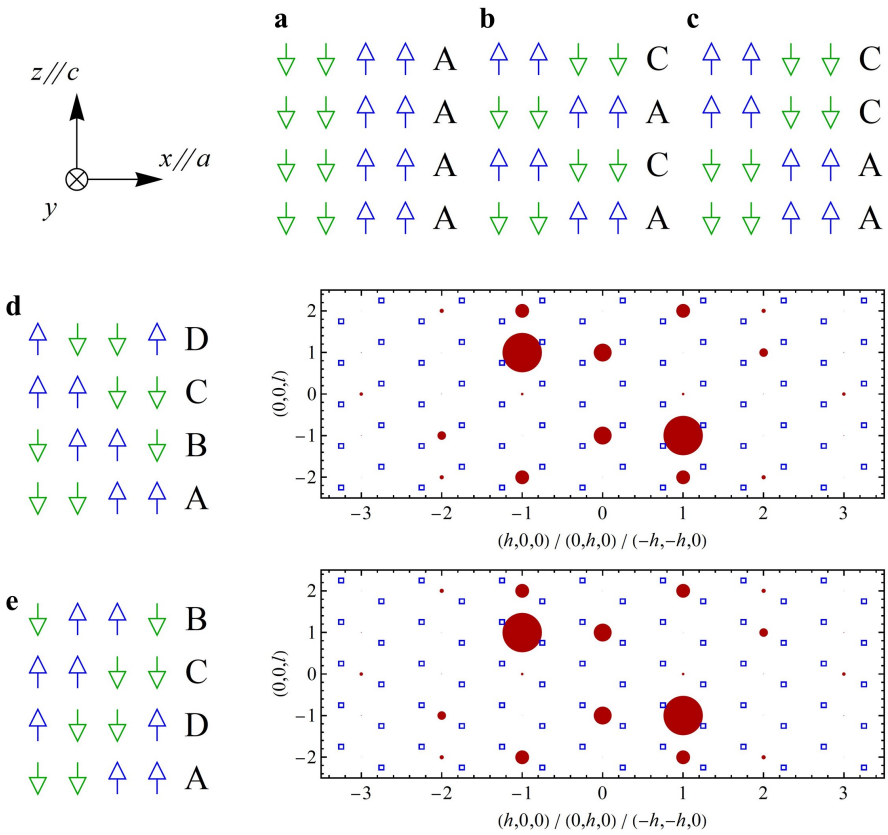

Figure 3.D.1: Various low-energy 3D stacking patterns with periodicity less than or equal to four. Positions of magnetic (blue squares) and nuclear Bragg peaks (red disk) of the ABCD and ADCB stacking are shown to the right of respective spin structures. The size of nuclear Bragg peaks is drawn in the scale of their relative intensities. By comparing with experimentally observed diffraction pattern, we find the ABCD stacking is realized in the FeI_2. The energies of ABCD, AACC and ADCB stacking do not depend on $J_0^{'}$ and $J_1^{'}$ and they would be degenerate if $J_{2a}^{'}$ and $J_{2b}^{'}$ were treated the same.

The energies of these configurations are

(a) AAAA, $E = J_1 - J_2 - J_3 + J_0^{'} + 2J_1^{'} - J_{2\mathrm{a}}^{'} - J_{2\mathrm{b}}^{'}\,,$

(b) ACAC, $E = J_1 - J_2 - J_3 - J_0^{'} - 2J_1^{'} + J_{2\mathrm{a}}^{'} + J_{2\mathrm{b}}^{'}\,,$

(c) AACC, $E = J_1 - J_2 - J_3\,,$

(d) ABCD, $E = J_1 - J_2 - J_3 - 2J_{2\mathrm{a}}^{'} + 2J_{2\mathrm{b}}^{'}\,,$

(e) ADCB, $E = J_1 - J_2 - J_3 + 2J_{2\mathrm{a}}^{'} - 2J_{2\mathrm{b}}^{'}\,.$

3.E Self-consistent Gaussian approximation

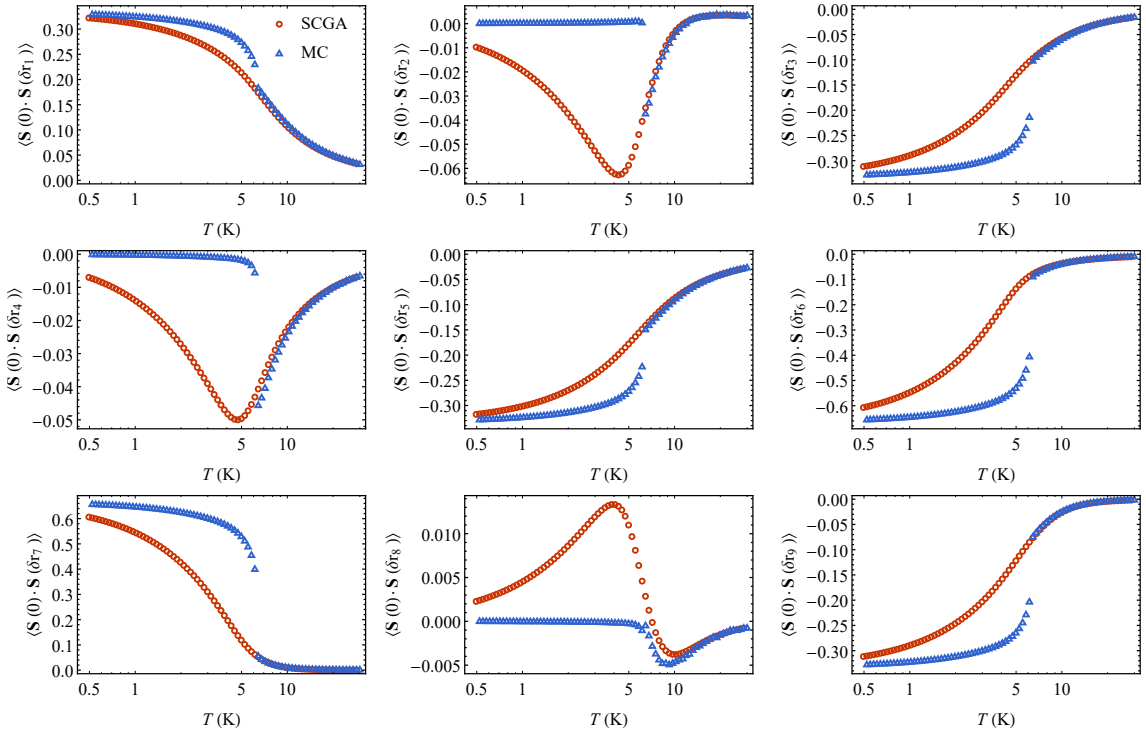

Figure 3.E.1: Comparison between SCGA calculation (blue triangles) with MC simulation (red circles) of SU(2) spins for the best fitting parameters of diffuse-scattering data. The good agreement is found for all spin correlations up to the phase transition.

Table 3.E.1: The best SCGA fitting parameters of diffuse-scattering data.

J_1 (K)	J_2	J_3	J_0'	J_1'	J_{2a}'	D	scale	const. bk
-2.74	1.31	2.46	-0.41	0.59	0.82	25.2	1.96	0.19

Self-consistent Gaussian approximation (SCGA) provides a quantitatively accurate approximation to Monte Carlo simulation of SU(2) spins in the paramagnetic regime [12]. It is a very useful tool for extracting exchange parameters from fitting single crystal diffuse scattering data, applicable for both isotropic [83] and anisotropic systems [93]. The basic idea is to relax the hard constraint on fixed spin-length and allow individual spins to

fluctuate,

$$\mathcal{Z} = \int \prod_i d\mathbf{S}_i \delta(\mathbf{S}_i^2 - 1) \exp\left(-\beta\mathcal{H}\right) \tag{3.5}$$

$$\approx \int_{-\infty}^{+\infty} \prod_{i,\alpha} dS_i^\alpha \exp\left(-\frac{1}{2}\lambda (S_i^\alpha)^2\right) \exp\left(-\beta\mathcal{H}\right) \tag{3.6}$$

while introducing a Langrange multiplier λ is to ensure the length of the spin is 1 on average

$$\frac{1}{N}\sum_{i\alpha} \left\langle (S_i^\alpha)^2 \right\rangle = 1 \tag{3.7}$$

It is convenient to work in the momentum space by Fourier transforming of the Hamiltonian

$$\mathcal{H} = \frac{1}{2}\sum_n \sum_{i,j} \sum_{\mu,\nu} \sum_{\alpha,\beta} A^n_{i\mu,j\nu} J_n^{\alpha\beta} S_\mu^\alpha(\mathbf{r}_i) S_\nu^\beta(\mathbf{r}_j) \tag{3.8}$$

$$= \frac{1}{2}\sum_n \sum_{i,j} \sum_{\mu,\nu} \sum_{\alpha,\beta} \frac{1}{N_{\text{uc}}} \sum_{\mathbf{q},\mathbf{p}} e^{i(\mathbf{R}_i+\mathbf{d}_\mu)\cdot\mathbf{q}} e^{i(\mathbf{R}_j+\mathbf{d}_\nu)\cdot\mathbf{p}} A^n_{i\mu,j\nu} J_n^{\alpha\beta} S_\mu^\alpha(\mathbf{q}) S_\nu^\beta(\mathbf{p}) \tag{3.9}$$

$$= \frac{1}{2}\sum_n \sum_{i} \sum_{\mu,\nu} \sum_{\alpha,\beta} \frac{1}{N_{\text{uc}}} \sum_{\mathbf{q},\mathbf{p}} e^{i(\mathbf{R}_i+\mathbf{d}_\mu)\cdot\mathbf{q}} e^{i(\mathbf{R}_i+\mathbf{d}_\mu)\cdot\mathbf{p}} J_n^{\mu\alpha,\nu\beta}(\mathbf{p}) S_\mu^\alpha(\mathbf{q}) S_\nu^\beta(\mathbf{p}) \tag{3.10}$$

$$= \frac{1}{2}\sum_n \sum_{\mu,\nu} \sum_{\alpha,\beta} \sum_{\mathbf{p}} J_n^{\mu\alpha,\nu\beta}(\mathbf{p}) S_\mu^\alpha(-\mathbf{p}) S_\nu^\beta(\mathbf{p}) \tag{3.11}$$

$$= \frac{1}{2}\sum_n \sum_{\mathbf{p}} \mathbf{S}(-\mathbf{p})^T \cdot \mathbf{J}_n(\mathbf{p}) \cdot \mathbf{S}(\mathbf{p}) \tag{3.12}$$

where $\alpha, \beta = x, y, z$ labels spin components, μ, ν sublattice index and i, j unit-cell index. $A^n_{i\mu,j\nu}$ is the adjacency matrix of the nth neighbor. The Fourier transform of the interaction

matrix, spins and the δ-funciton are used

$$J_n^{\mu\alpha,\nu\beta}(\mathbf{p}) = J_n^{\alpha\beta} A_{\mu\nu}^n(\mathbf{p}) = J_n^{\alpha\beta} \sum_j A_{i\mu,j\nu}^n \exp(-i\mathbf{p}\cdot(\mathbf{R}_i - \mathbf{R}_j + \mathbf{d}_\mu - \mathbf{d}_\nu))) \tag{3.13}$$

$$S_\mu^\alpha(\mathbf{q}) = \frac{1}{\sqrt{N_{\text{uc}}}} \sum_i S_\mu^\alpha(\mathbf{r}_i) e^{-i\mathbf{q}\cdot(\mathbf{R}_i+\mathbf{d}_\mu)} \tag{3.14}$$

$$S_\mu^\alpha(\mathbf{r}_i) = \frac{1}{\sqrt{N_{\text{uc}}}} \sum_{\mathbf{q}} S_\mu^\alpha(\mathbf{q}) e^{i\mathbf{q}\cdot(\mathbf{R}_i+\mathbf{d}_\mu)} \tag{3.15}$$

$$\delta(\mathbf{q}-\mathbf{p}) = \frac{1}{N_{\text{uc}}} \sum_i e^{-i\mathbf{R}_i\cdot(\mathbf{q}-\mathbf{p})}\,. \tag{3.16}$$

The partition function can be written in a Gaussian form

$$\mathcal{Z} = \int \prod_{\mathbf{q}} d\mathbf{S}(-\mathbf{q}) d\mathbf{S}(\mathbf{q}) \exp\left(-\frac{1}{2}\mathbf{S}(-\mathbf{q}) \cdot \left(\lambda \mathbf{1} + \beta \sum_n \mathbf{J}_n(\mathbf{q}) \right) \cdot \mathbf{S}(\mathbf{q})^T \right) \tag{3.17}$$

where $\mathbf{S}(\mathbf{q})$ is a $3N_{\text{basis}}$-component vector and $\mathbf{J}_n(\mathbf{q})$ is a $3N_{\text{basis}} \times 3N_{\text{basis}}$ matrix. The spin correlation is given by

$$S^{\alpha\beta}(\mathbf{q}) = \sum_{\mu,\nu} \left\langle S_\mu^\alpha(-\mathbf{q}) S_\nu^\beta(\mathbf{q}) \right\rangle = \sum_{\mu,\nu} \left(\left[\lambda \mathbf{1} + \beta \sum_n \mathbf{J}_n(\mathbf{q}) \right]^{-1} \right)_{\mu\nu}^{\alpha\beta}. \tag{3.18}$$

The Lagrangian multiplier λ is solved from

$$1 = \frac{1}{N_{\text{uc}}} \sum_{\mathbf{q},\alpha} S^{\alpha\alpha}(\mathbf{q}) = \frac{1}{N_{\text{basis}} N_{\text{uc}}} \sum_{\mathbf{q}} \text{tr} \left[\lambda \mathbf{1} + \beta \sum_n \mathbf{J}_n(\mathbf{q}) \right]^{-1}. \tag{3.19}$$

The equal-time structure factor observed in unpolarized neutron scattering is

$$S(\mathbf{Q}) = \sum_{\alpha\beta} \left(\delta^{\alpha\beta} - \frac{Q^\alpha Q^\beta}{Q^2} \right) S^{\alpha\beta}(\mathbf{Q}) \tag{3.20}$$

where $\mathbf{Q} = \mathbf{G} + \mathbf{q}$ and $\mathbf{G}$ is a reciprocal lattice vector. Spin correlations in real space can

be calculated as well

$$\langle S^{\alpha}(\mathbf{r})S^{\beta}(\mathbf{r}+\delta\mathbf{r}_n)\rangle = \frac{1}{M_n}\frac{1}{N_{\text{basis}}}\frac{1}{N_{\text{uc}}}\sum_{i,j}\sum_{\mu,\nu} A^n_{i\mu,j\nu}\langle S^{\alpha}(\mathbf{R}_i+\mathbf{d}_\mu)S^{\beta}(\mathbf{R}_j+\mathbf{d}_\nu)\rangle \quad (3.21)$$

$$= \frac{1}{M_n}\frac{1}{N_{\text{basis}}}\frac{1}{N_{\text{uc}}}\sum_{\mu,\nu}\sum_{\mathbf{p}} A^n_{\mu\nu}(\mathbf{p})\langle S^{\alpha}_{\mu}(-\mathbf{p})S^{\beta}_{\nu}(\mathbf{p})\rangle\,. \quad (3.22)$$

where M_n is the number nth neighbor, N_{basis} the number atom in the unit-cell and N_{uc} the number of unit-cell. The single-ion term, $-D\sum_{i\mu}(S^z_\mu(\mathbf{r}_i))^2$, after Fourier transfom, adds a constant $-2D$ to the zz component for each sublattice in the interaction matrix.

3.F Generalized spin-wave theory

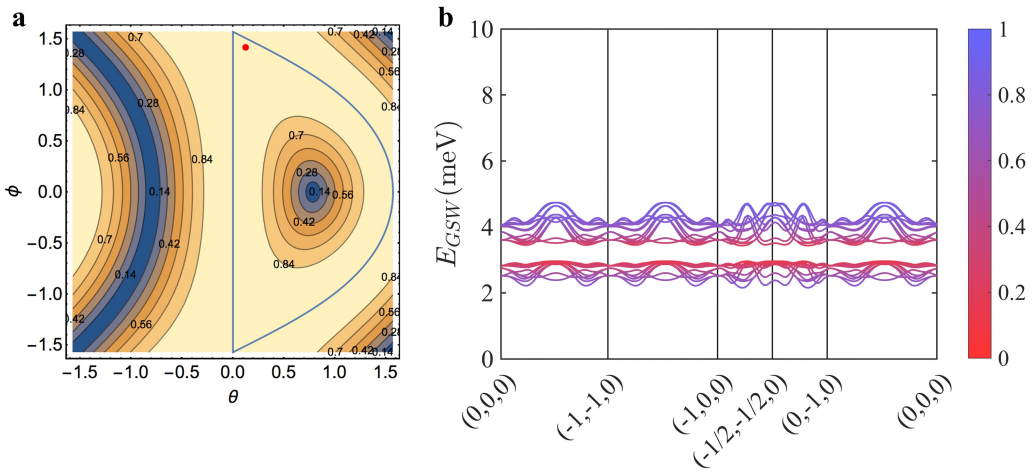

Figure 3.F.1: (a) Length of dipole moment m in parameter space (θ, ϕ). Dark blue line: $SU(2)$ spin coherent state; Red dot: optimal fitting parameter. (b) Excitation spectrum in $SU(3)$ spin wave theory. Color scale: blue (red) refers to the weight of b_{i0} and $b_{i,-1}$ boson, respectively.

3.G GSWT fitting of inelastic neutron-scattering data

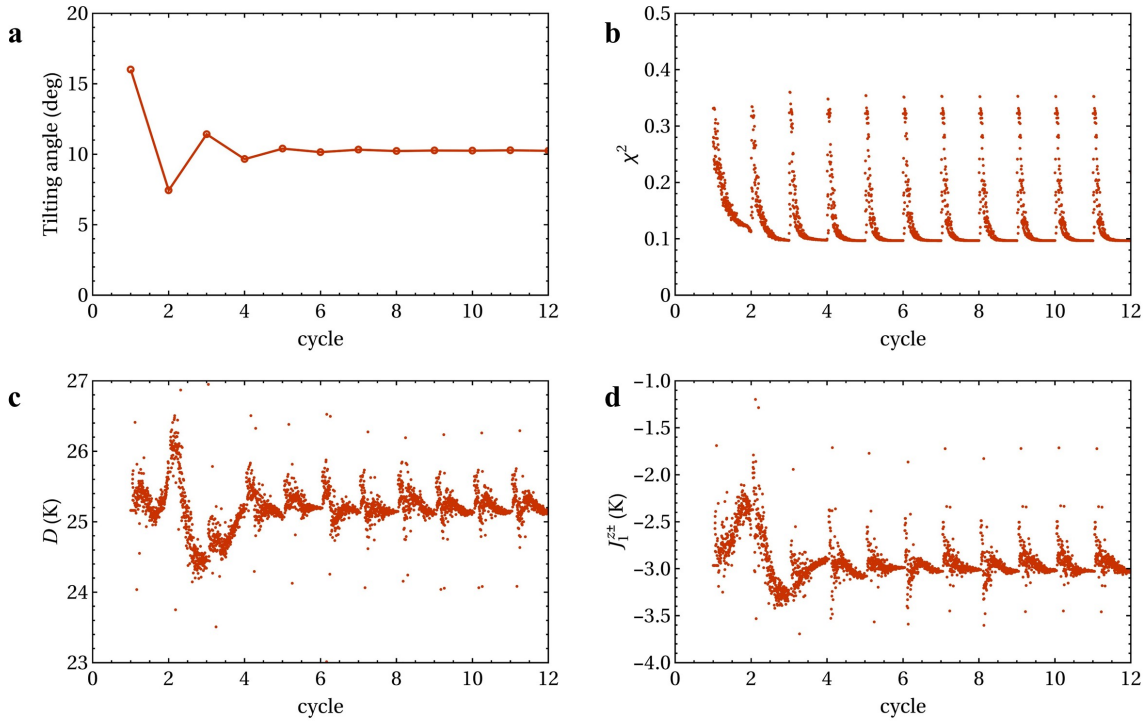

Figure 3.G.1: Progress of various quantities in the GSWT fittings - the tilting angle ((a)), the reduced χ^2 ((b)), the single-ion anistropy D ((c)) and the off-diagonal exchange $J_1^{z\pm}$ ((d)) which is responsible for the hybridization.

We perform a pixel-to-pixel fitting to selected cuts of symmetrized inelastic neutron-scattering data along a high-symmetry path in the $(h, k, 0)$-plane and four out-of-plane paths, shown in Figure 3.G.2. The raw data was collected on SEQUOIA at 1.8 K with incoming neutron energy $E_i = 12$ meV. Our anisotropic model includes four exchange constants $\{J_1^{\pm}, J_1^{zz}, J_1^{\pm\pm}, J_1^{z\pm}\}$ for NN bonds, two exchange constants $\{J^{\pm}, J^{zz}\}$ for each of the other bonds, one single-ion anisotropy, one scaling parameter and one damping parameter, 17 parameters in total. The J_0^{zz} and J_1^{zz} coupling does not have any effect on calculated inelastic spectrum, so they are set to zero in the fitting. The reduced χ^2 defined as $\sum_i (I_{\text{obs}} - I_{\text{cal}})/N_{\text{pix}}$ is minimized by varying the other 15 parameters using the Nelder-Mead method implemented in the NLopt package [94, 95]. The fitting procedure

runs in cycles, each containing 300 minimization steps. The ground state is optimized at the beginning of each cycle. The optimized magnetic structure appears to tilt away from c-axis while remain collinear. The tilting angle converges to around 10°. The fitting starts with the best SCGA fitting parameters of diffuse-scattering data with small randomization. We performed 80 independent fittings with randomized starting parameters and computed the standard deviation of converged results after 11 cycles as an estimation of error. The progress for one of the fitting is shown in Figure 3.G.1. The best fitting parameters are listed in Table 3.E.1. All the zz-couplings only contribute constants to the calculated spectrum, which leads to significant parameter dependence among them. This can be seen from their large standard deviations. The spectrum is however extremely sensitive to the combination $E_{\text{SIBS}} = 4(-J_1^{zz} + J_2^{zz} + J_3^{zz} + 2J_{2a}^{\prime zz})$ which determines the energy of the single-ion bound state. All the transverse couplings and the single-ion anisotropy D are determined with very small error.

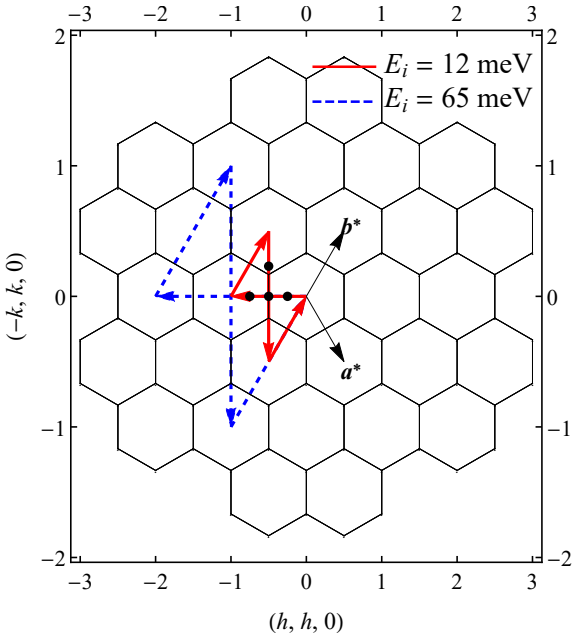

Figure 3.G.2: The high-symmetry path used in the GSWT fitting and the convention of reciprocal lattice vectors. The out-of-plane paths are indicated by black dots.

Table 3.G.1: The best GSWT fitting parameters of inelastic neutron-scattering data.

	$J_1^{\pm}$	$J_1^{\pm\pm}$	$J_1^{z\pm}$	$J_2^{\pm}$	$J_3^{\pm}$	$J_0^{'\pm}$	$J_1^{'\pm}$	$J_{2a}^{'\pm}$
Mean	-2.770	-2.019	-3.017	0.272	1.953	0.334	0.17	0.719
SD	0.019	0.010	0.006	0.017	0.013	0.010	0.004	0.008

	D	scale	damping
Mean	25.729	0.760	0.128
SD	0.020	0.006	0.004

	J_1^{zz}	J_2^{zz}	J_3^{zz}	$J_0^{'zz}$	$J_1^{'zz}$	$J_{2a}^{'zz}$	E_{SIBS}
Mean	-2.461	0.719	4.720	0.000	0.000	0.143	2.822
SD	0.895	0.993	0.990	-	-	0.396	0.001

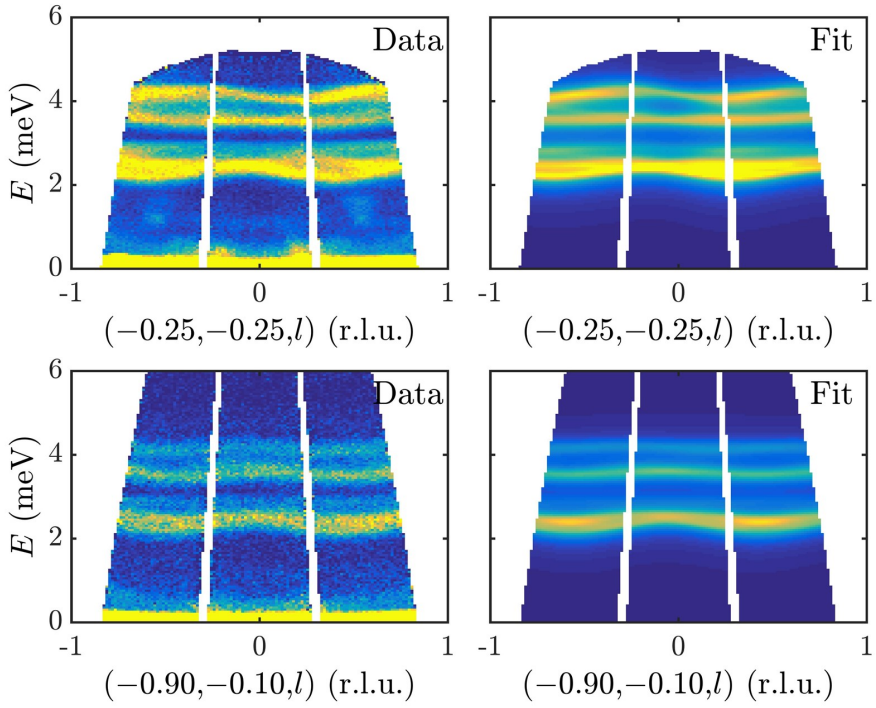

Figure 3.G.3: The comparison between the data and GSWT fitting for cuts in the out-of-plane direction.

3.H Symmetry analysis of exchange Hamiltonian

The maximally symmetry-allowed exchange interaction on a certain bond can be obtained from SpinW [10]. It is still useful to understand how the symmetry analysis works and double-check the result from SpinW. Here we present two examples to illustrate some of the details. Under a generic symmetry operation $\mathbf{R}$, spins and atomic positions transform as axial and polar vectors

$$\mathbf{S}(\mathbf{r}_{i'}) = \det(\mathbf{U})\mathbf{U}\cdot\mathbf{S}(\mathbf{r}_i)\,, \quad \mathbf{r}_{i'} = \mathbf{U}\cdot\mathbf{r}_i + \mathbf{t} \tag{3.23}$$

The energy of a bond is a scalar, therefore invariant under this operation

$$\mathbf{S}(\mathbf{r}_{i'})^T\cdot\mathbf{J}_{i'j'}\cdot\mathbf{S}(\mathbf{r}_{j'}) = \mathbf{S}(\mathbf{r}_i)^T\cdot\mathbf{J}_{ij}\cdot\mathbf{S}(\mathbf{r}_j)\,, \tag{3.24}$$

leading to a transformation of the exchange matrix

$$\mathbf{J}_{i'j'} = \mathbf{U}\cdot\mathbf{J}_{ij}\cdot\mathbf{U}^T\,. \tag{3.25}$$

Let's take a J_1 bond between atom i at $(0,0,0)$ and atom j at $(1,0,0)$. The first step is to find the point group at the center of the bond $(1/2,0,0)$. This information is tabulated on Bilbao crystallographic server under "Wyckoff Positions". There are three symmetry operations besides the identity. First, let's look at inversion operation $(-x+1,-y,-z)$ which simply switches $(0,0,0)$ and $(1,0,0)$, therefore we have

$$\mathbf{J}_{ji} = \mathbf{J}_{ij}^T = \mathbf{U}\cdot\mathbf{J}_{ij}\cdot\mathbf{U}^T = \mathbf{J}_{ij}\,, \quad \mathbf{U} = \mathbf{M}\cdot\begin{pmatrix}-1&0&0\\0&-1&0\\0&0&-1\end{pmatrix}\cdot\mathbf{M}^{-1} = \begin{pmatrix}-1&0&0\\0&-1&0\\0&0&-1\end{pmatrix}. \tag{3.26}$$

We can deduce that $\mathbf{J}_{ij}$ has to be symmetric, namely, for a bond with inversion center the antisymmetric Dzyaloshinskii–Moriya interaction is absent. The matrix $\mathbf{M}$ transforms group elements from the fractional coordinate to the global Cartesian coordinate in the convention where $\mathbf{x}//\mathbf{a}$, $\mathbf{y}//(\mathbf{a}\times\mathbf{b})\times\mathbf{x}$ and $\mathbf{z}//(\mathbf{a}\times\mathbf{b})$, given by

$$\mathbf{M}=\begin{pmatrix} a & b\cos(\gamma) & c\cos(\beta) \\ 0 & b\sin(\gamma) & c(\cos(\alpha)-\cos(\beta)\cos(\gamma))\csc(\gamma) \\ 0 & 0 & \frac{V\csc(\gamma)}{ab} \end{pmatrix}. \tag{3.27}$$

The next symmetry element $(x-y,-y,-z)$ leaves atom i and j invariant,

$$\mathbf{J}_{ij}=\mathbf{U}\cdot\mathbf{J}_{ij}\cdot\mathbf{U}^{T},\quad \mathbf{U}=\mathbf{M}\cdot\begin{pmatrix} 1 & -1 & 0 \\ 0 & -1 & 0 \\ 0 & 0 & -1 \end{pmatrix}\cdot\mathbf{M}^{-1}=\begin{pmatrix} 1 & 0 & 0 \\ 0 & -1 & 0 \\ 0 & 0 & -1 \end{pmatrix}, \tag{3.28}$$

where the action $\mathbf{M}$ is non-trivial. The resulting exchange matrix is

$$\mathbf{J}_{ij}=\begin{pmatrix} J_{xx} & 0 & 0 \\ 0 & J_{yy} & J_{yz} \\ 0 & J_{yz} & J_{zz} \end{pmatrix}. \tag{3.29}$$

The last symmetry operation does not provide further reduction. To obtain the exchange matrix for the other J_1 bonds, we just need to act corresponding symmetry operation on Eq. 3.29. As a second example, it is instructive to look at a $J_1^{'}$ bond between atom i at $(0,0,0)$ and atom j at $(0,0,1)$. Only the symmetry operation $(-x+1,-y+1,-z)$ maps this bond onto itself up to a lattice translation, leading to $\mathbf{J}_{ij}=\mathbf{J}_{ij}^{T}$. The other two operations map it to other $J_1^{'}$ bonds, therefore does not place further restriction on the exchange matrix, leaving six symmetry-allowed parameters for this bond. This result agrees with calculation from SpinW.

CHAPTER 4
SPIN DYNAMICS SIMULATIONS

4.1 Introduction

A spin liquid state is, in simple terms, a disordered spin state with short-range correlations. It can be divided into two categories, classical spin liquids and quantum spin liquids, according to the nature of the fluctuation that keeps spins from forming an ordered state. The former is ubiquitous. Any magnetic material above the long-range ordered transition is in a spin liquid state, where persistent thermal fluctuations dominate. The latter is much more exotic, in which spins are binding and breaking as entanglement pairs due to strong quantum fluctuations, only known to exist in quasi-1D materials so far. These two classes might overlap or coexist in materials generally called "frustrated magnets". The word "frustration" refers to the fact that not all interactions in the Hamiltonian can be simultaneously satisfied. This could come from geometrical constraints, such as antiferromagnetic nearest neighbor interaction on a triangular lattice, or from incompatible interactions, for instance, antiferromagnetic nearest neighbor and ferromagnetic next nearest neighbor interactions on a square lattice. One of the important consequence of frustration is that the extensive degeneracy of the ground state. Such systems remain in spin liquid states at temperatures much lower than the ordering temperature inferred from its interaction strength. Moreover, the excitations shows broad continua in contrast to that of an ordered state. These broad features could be of similar origin to the fractional excitations in quasi-1D materials which is purely quantum effect, or the continuum from magnon decay due to scattering among magnons. Generic quantum simulations are not readily accessible for modeling bulk 3D materials. I introduce semi-classical spin dynamics simulation of spin liquid systems in this chapter. Comparison with experiments is the key to discern possible quantum effects.

4.2 Methods

The classical spin dynamics is given by Bloch equations

$$\frac{d\mathbf{S}_k}{dt} = \frac{d\mathcal{H}}{d\mathbf{S}_k} \times \mathbf{S}_k. \tag{4.1}$$

which is a set of coupled non-linear differential equations describing the precession of each spin with respect to the local magnetic field generated by its neighbors. The total energy and magnetization are conserved in the dynamcs. This set of equations can be viewed as a classical version of the Heisenberg equation, where $\mathbf{S}_k$ is not quantum mechanical operators, but a classical vector. For the cross product to be defined, spin vectors have to be three-dimensional – Heisenberg spins. Ising or XY spins do not possess dynamics given by Bloch equations. The interaction can be practically of any form, such as anisotropic Heisenberg model, long-range dipolar interaction, biquadratic interactions and more [96]. Bloch equations can be used to study the dynamics from any classical spin configurations in thermal equilibrium or far-from-equilibrium. For an ordered state, the simulation gives the same result as the linear spin-wave theory. For spin liquid states, it is able to capture low lying excitations and scatterings among spin-waves. The pioneer work is dated back to Keren [97, 98]. Chalker et al adopted this approach in studying frustrated pyrochlore lattice [99, 100, 101, 12]. Landau et al developed a dynamic finite-size scaling theory for the dynamical structure factor at critical point and used it to extract the dynamic critical exponent [102, 103, 104, 105, 106].

Special numerical schemes that incorporate conservation laws are developed in [107, 108, 109, 110, 111, 112, 113, 114], which requires adaptation for each specific problem. Instead, I will use the 4th order Runge-Kutta method (RK4) and the predictor-corrector method which can be easily implimented for arbitrary interations. For a comparison of performance among different methods, see [96]. The problem that I need to solve is written

in general as

$$\dot{y} = f(t, y), \quad y(0) = y_0 \tag{4.2}$$

where y is to be understood as a vector. To get the system configuration at next time step $t + \delta t$, RK4 only requires the present configuration,

$$y(t + \delta t) = y(t) + \frac{\delta t}{6}\left(k_1 + 2k_2 + 2k_3 + k_4\right) \tag{4.3}$$

$$k_1 = f(t, y(t)) \tag{4.4}$$

$$k_2 = f(t + \frac{\delta t}{2}, y(t) + \frac{\delta t}{2}k_1) \tag{4.5}$$

$$k_3 = f(t + \frac{\delta t}{2}, y(t) + \frac{\delta t}{2}k_2) \tag{4.6}$$

$$k_4 = f(t + \delta t, y(t) + \delta t k_3)\,. \tag{4.7}$$

This method alone is not enough to contain the propagation of the numerical error given the total integration time. Following D.P. Landau [96], I only use this method to generate the first three time steps and initiate the predictor-corrector method which is used for subsequent calculation. The predictor-corrector method consists of two steps: the explicit Adams-Bashforth four-step method

$$y(t + \delta t) = y(t) + \frac{\delta t}{24}\left(55f(y(t)) - 59f(y(t - \delta t)) + 37f(y(t - 2\delta t)) - 9f(y(t - 3\delta t))\right) \tag{4.8}$$

and typically one iteration of the implicit Adams-Moulton three-step method

$$y(t + \delta t) = y(t) + \frac{\delta t}{24}\left(9f(y(t + \delta t)) + 19f(y(t)) - 5f(y(t - \delta t)) + f(y(t - 2\delta t))\right)\,. \tag{4.9}$$

For the purpose of modeling neutrons scattering data, equilibrium spin configurations

from classical Monte Carlo simulations are appropriate initial conditions in solving Bloch equations. One can also study the time evolution of non-equilibrium states, such as states following a temperature quench or solitonic states like skyrmions. After the solution is acquired, I perform the Fourier transform of spin-spin correlation in space and time to obtain the dynamical structure factor

$$\mathcal{S}^{\alpha\beta}(\mathbf{Q},\omega) = \langle S^{\alpha}(\mathbf{Q},\omega) S^{\beta}(\mathbf{Q},\omega)^{\star} \rangle \tag{4.10}$$

The spin structure factor is given by

$$S^{\alpha}(\mathbf{Q},\omega) = \sum_{i=1}^{N} \sum_{\mu=1}^{n} e^{-i\mathbf{Q}\cdot(\mathbf{R}_i+\mathbf{r}_\mu)} \int_{-\infty}^{+\infty} e^{-i\omega t} S_i^{\mu,\alpha}(t)\, dt \tag{4.11}$$

$$\approx \sum_{\mu=1}^{n} e^{-i\mathbf{Q}\cdot\mathbf{r}_\mu} \delta t \left(\sum_{h=1}^{N_1} \sum_{k=1}^{N_2} \sum_{l=1}^{N_3} e^{-i\mathbf{Q}\cdot((h-1)\mathbf{a}+(k-1)\mathbf{b}+(l-1)\mathbf{c})} \sum_{g=1}^{M} e^{-i\omega M \delta t (g-1)/M} S_{h,k,l,g}^{\mu,\alpha} \right) \tag{4.12}$$

where M is the number of time steps, $\mathbf{R}_i$ is the position of the unit cell, $\mathbf{r}_\mu$ is the position of atoms inside the unit cell and the total number of atoms is $N_1 \times N_2 \times N_3 \times n$. Comparing the expression inside the parenthesis with the FFT convention in Mathematica,

$$\tilde{S}_{h,k,l,g}^{\mu,\alpha} = \sum_{h=1}^{N_1} \sum_{k=1}^{N_2} \sum_{l=1}^{N_3} \sum_{g=1}^{M} e^{-2\pi i((h^\star-1)(h-1)/N_1+(k^\star-1)(k-1)/N_2+(l^\star-1)(l-1)/N_3+(g^\star-1)(g-1)/M)} S_{h,k,l,g}^{\mu,\alpha} \tag{4.13}$$

I identify

$$\omega = 2\pi \frac{(g^\star-1)}{M\delta t}, \quad \mathbf{Q} = 2\pi \frac{(h^\star-1)}{N_1}\mathbf{a}^\star + 2\pi \frac{(k^\star-1)}{N_2}\mathbf{b}^\star + 2\pi \frac{(l^\star-1)}{N_3}\mathbf{c}^\star \tag{4.14}$$

$$(h^\star, k^\star, l^\star, g^\star) = (1,1,1,1)...(N_1, N_2, N_3, M)\,, \tag{4.15}$$

and the `FourierParameters` $\rightarrow \{1, -1\}$ in Mathematica. Basically, I need to FFT each sublattice, multiply appropriate phase factor and sum over all sublattices. The time step in the simulation is given by a fraction of the inverse interaction strength, typically $0.01/J$ to $0.02/J$. If the spin length is not 1, the interaction strength has to be multiplied by the spin length. This can be seen from the Block equation, where the left hand side is linear in $\mathbf{S}_i$ and the right hand side is quadratic.

4.3 Benchmark

As a benchmark calculation, spin dynamics simulations are performed for systems of Heisenberg spins with NN ferromagnetic XY interactions on a simple cubic lattice. This is to compare with D.P. Landau's calculation in [115] and satisfactory agreement is reached. Another calculation on NN antiferromagnetic Heisenberg interactions on a diamond-lattice is given in the Appendix A, where results on different temperatures are presented.

First of all, some confusion about the term "XY model" must be clarified. Typically, the classical "XY model" refers to the $O(2)$ model or the rotor model, where spin vectors have only two components $\mathbf{S}_i = (\cos(\theta_i), \sin(\theta_j))$. The Hamiltonian often is written in terms of the angle variables

$$\mathcal{H} = \frac{1}{2} J \sum_{ij} \mathbf{S}_i \cdot \mathbf{S}_j = \frac{1}{2} J \sum_{ij} \cos(\theta_i - \theta_j) \tag{4.16}$$

The classical dynamics of such models, namely the time evolution of the spin vectors, were studied by adding a kinetic term to the Hamiltonian [116, 117]. The XY model that D.P. Landau studied in [115] is an anisotropic Heisenberg in the limit where the z-components of spins do not couple at all, which he calls "the planar Heisenberg variant of the XY model",

$$\mathcal{H} = \frac{1}{2} J \sum_{ij} S_i^x S_j^x + S_i^y S_j^y \,, \tag{4.17}$$

in the global frame. He has shown that it belongs to the same static XY universality class. To avoid confusion, I will call this Heisenberg-spin XY model. Below I summarize a few bullet points about the simulation.

- The exchange constant is set to 1K. 400 independent runs of Monte Carlo simulation were performed from 5K to 1K with 0.9 cooling rate. Different random number seed is used to start each run. I only collected one data point after thermalization at each

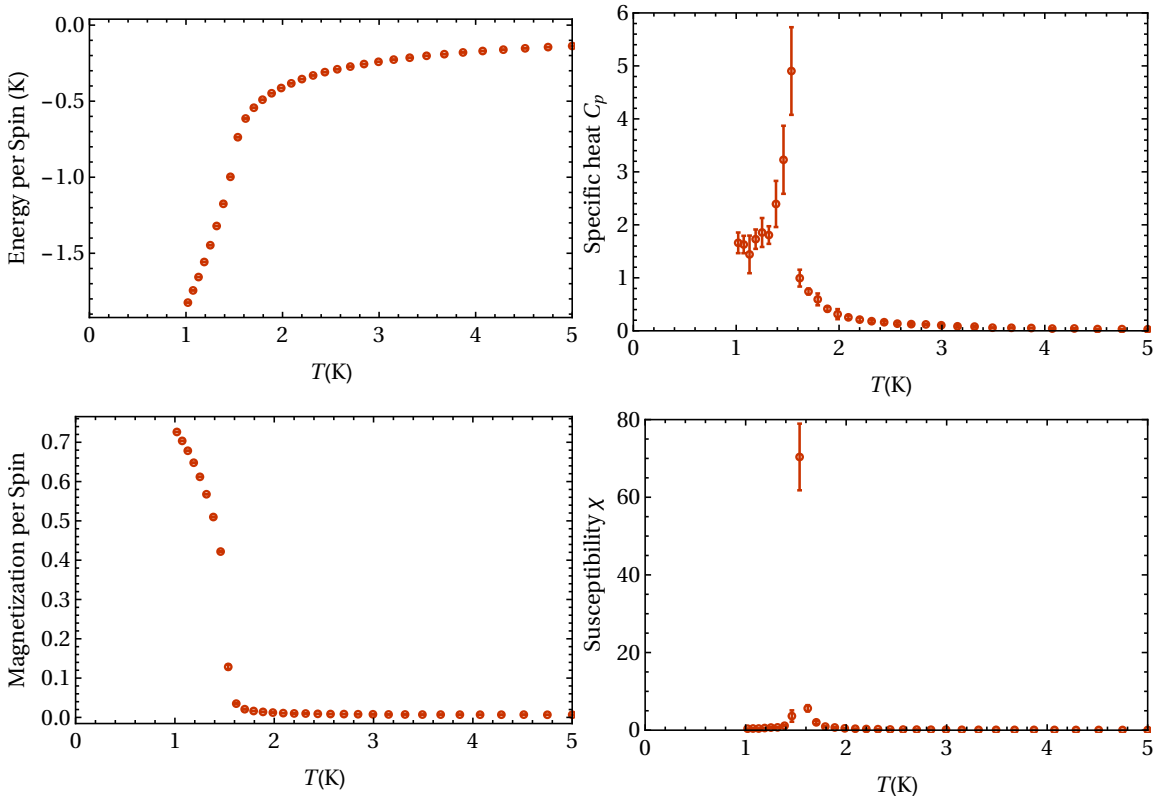

Figure 4.1: Thermodynamic properties of the Heisenberg-spin XY model.

temperature for every run. The goal is to ensure the statistical independence of all the data points. The error-bar is obtained by grouping data into five sets and compute the standard deviation of the averages.

- The thermalization is determined by if the correlation between spin configurations before and after a sweep is smaller than zero. Every sweep contains N single-spin flips and N over-relaxation moves. Minimum of 10 sweep is performed at every temperature regardless if correlation criteria is satisfied. Maximum number of sweeps is set to be 1000 even if correlation criteria is not satisfied, which happens during and after the phase transition.

- The critical temperature is estimated to be 1.5368K (the peak of heat capacity), close to 1.5528K obtained by D.P. Landau.

- The spin dynamicss simulations were performed with $\delta t = 0.02/J$ and 16000 time steps. $\mathcal{S}_{xx}$ and $\mathcal{S}_{yy}$ were symmetrized and averaged together to improve the stats. $\mathcal{S}_{zz}$ was symmetrized separately.

- The white lines in the all color plots are from the linear spin-wave theory. The temperature "renormalization" effect is evident. This can be compared to D.P. Landau's Figure 6.

- The line cuts in Figure 2 agrees with D.P. Landau's Figure 5, although the peaks seems to be a bit less sharp.

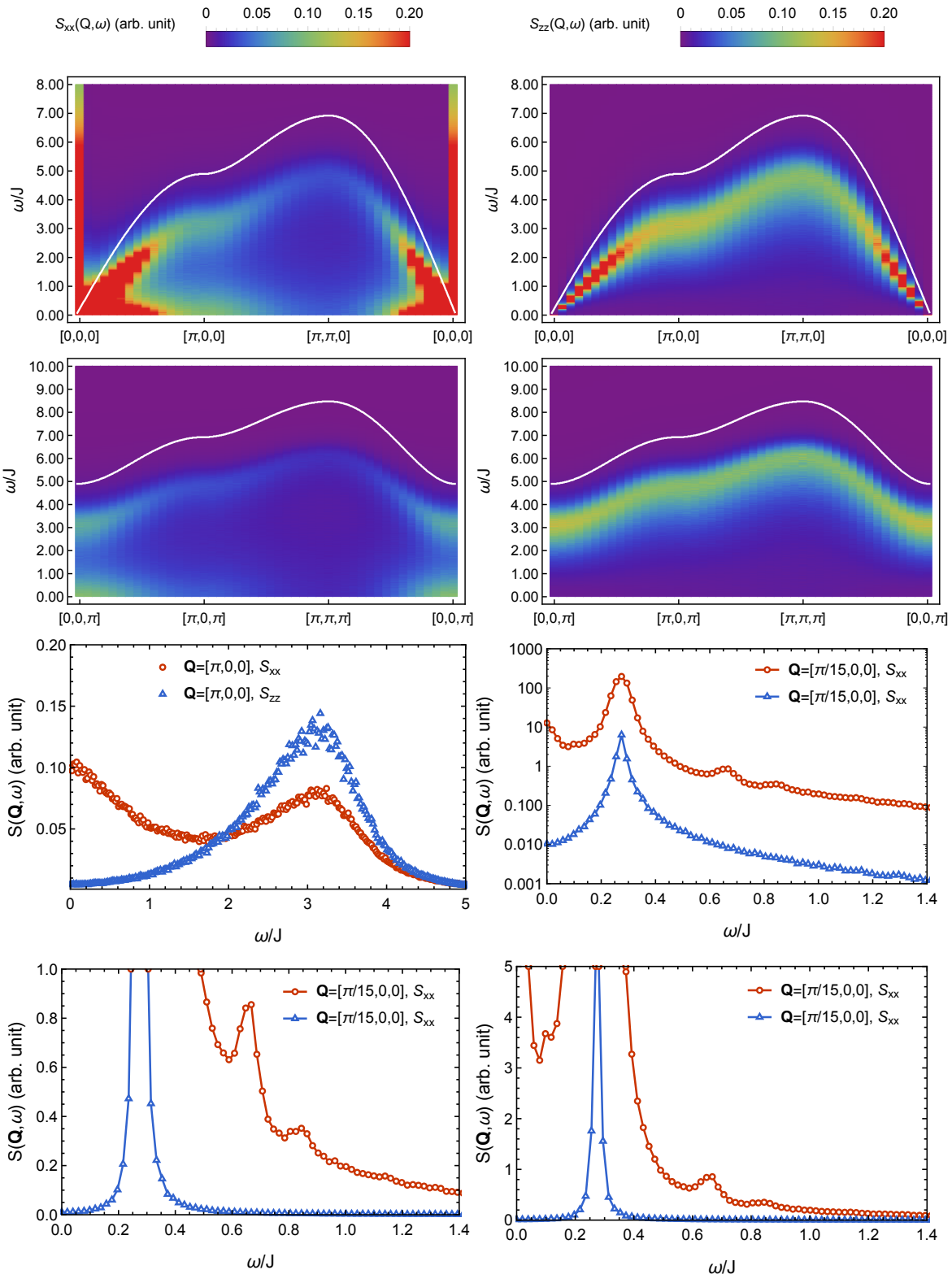

Figure 4.2: The dynamical structure factor of Heisenberg-spin XY model at 1.386K ($0.9T_c$), averaged over 200 initial conditions.

4.4 Application

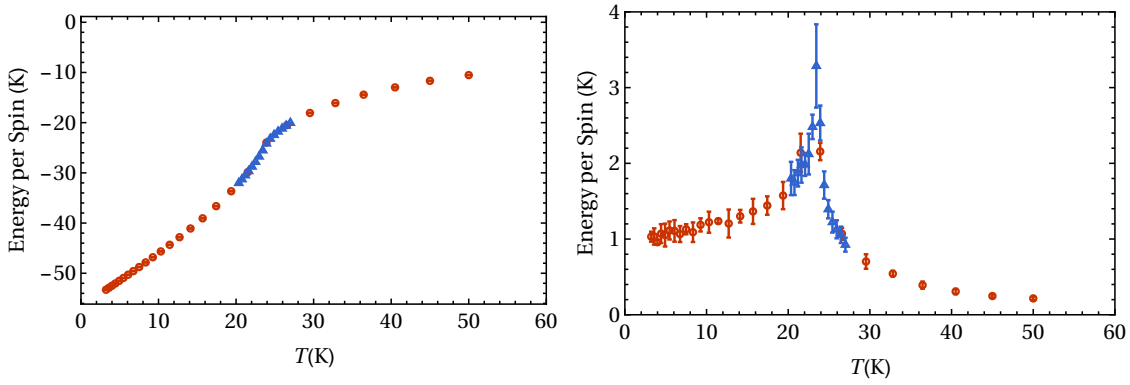

Figure 4.3: Thermodynamic properties of NN antiferromagneic Heisenberg model on a diamond-lattice.

In this section, I apply spin dynamics simulations to study the excitation spectrum of a NN antiferromagnetic Heisenberg model on a diamond-lattice. The exchange constant is set to 28.28K ($0.65 \times 11.602 \times S(S+1)$ with $S = 3/2$) to make comparison with the real system of $CoRh_2O_4$ [118]. 1000 independent runs of Monte Carlo simulation (red points in Figure 4.3) were performed from 50K to 1K with 0.9 cooling rate. 2000 separate runs (blue points) were performed from 27K to 20K with 0.98 cooling rate. The thermalization protocol is the same as before. The critical temperature is estimated to be 23.44K (the peak of heat capacity), a bit off from experimentally value of 25.68K. The spin dynamicss simulations were performed with $\delta t = 0.02/J$ and 16000 time steps at 4K, 20K, 24K and 30K, Figure 4.4∼4.7. Since the system is Heisenberg, $\mathcal{S}_{xx}$, $\mathcal{S}_{yy}$ and $\mathcal{S}_{zz}$ were symmetrized and averaged together to improve the stats for each temperature. The white lines in all color plots are from the linear spin-wave theory. There seems to some small side peaks as well, presumably from higher order harmonics of spin-waves. The stats is not high enough to resolve them clearly.

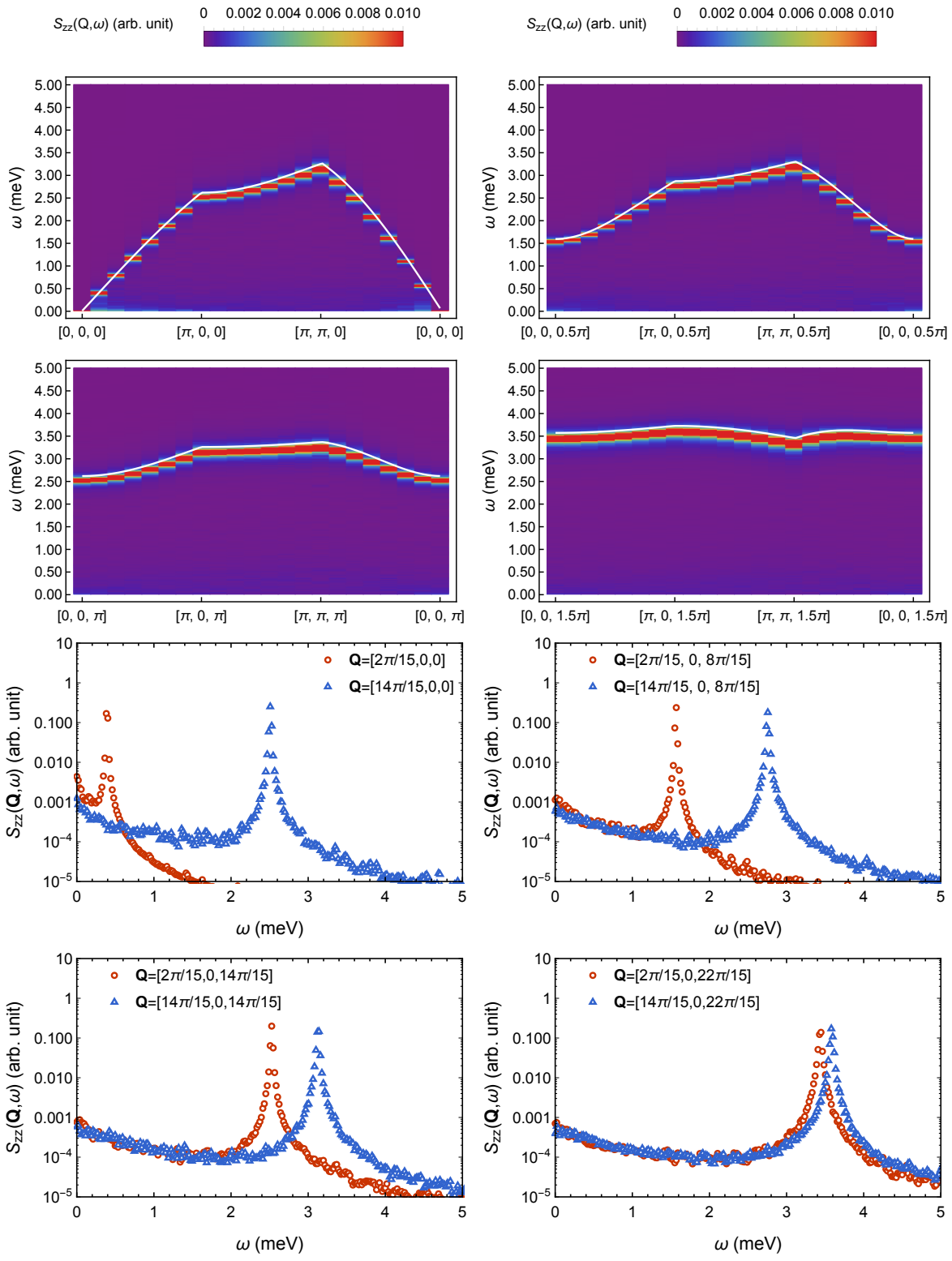

Figure 4.4: The dynamical structure factor of the diamond-lattice system at 4K.

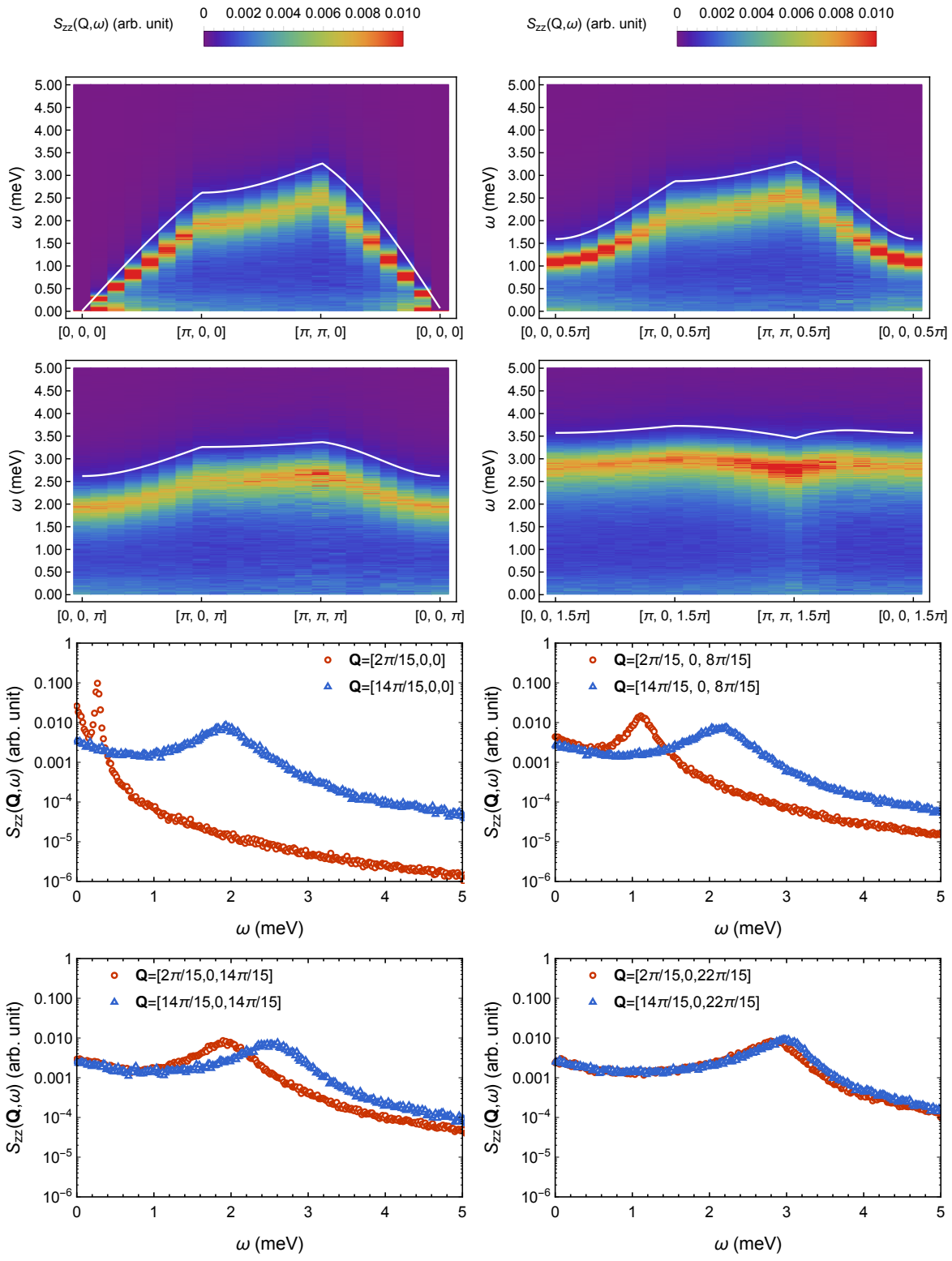

Figure 4.5: The dynamical structure factor of the diamond-lattice system at 20K.

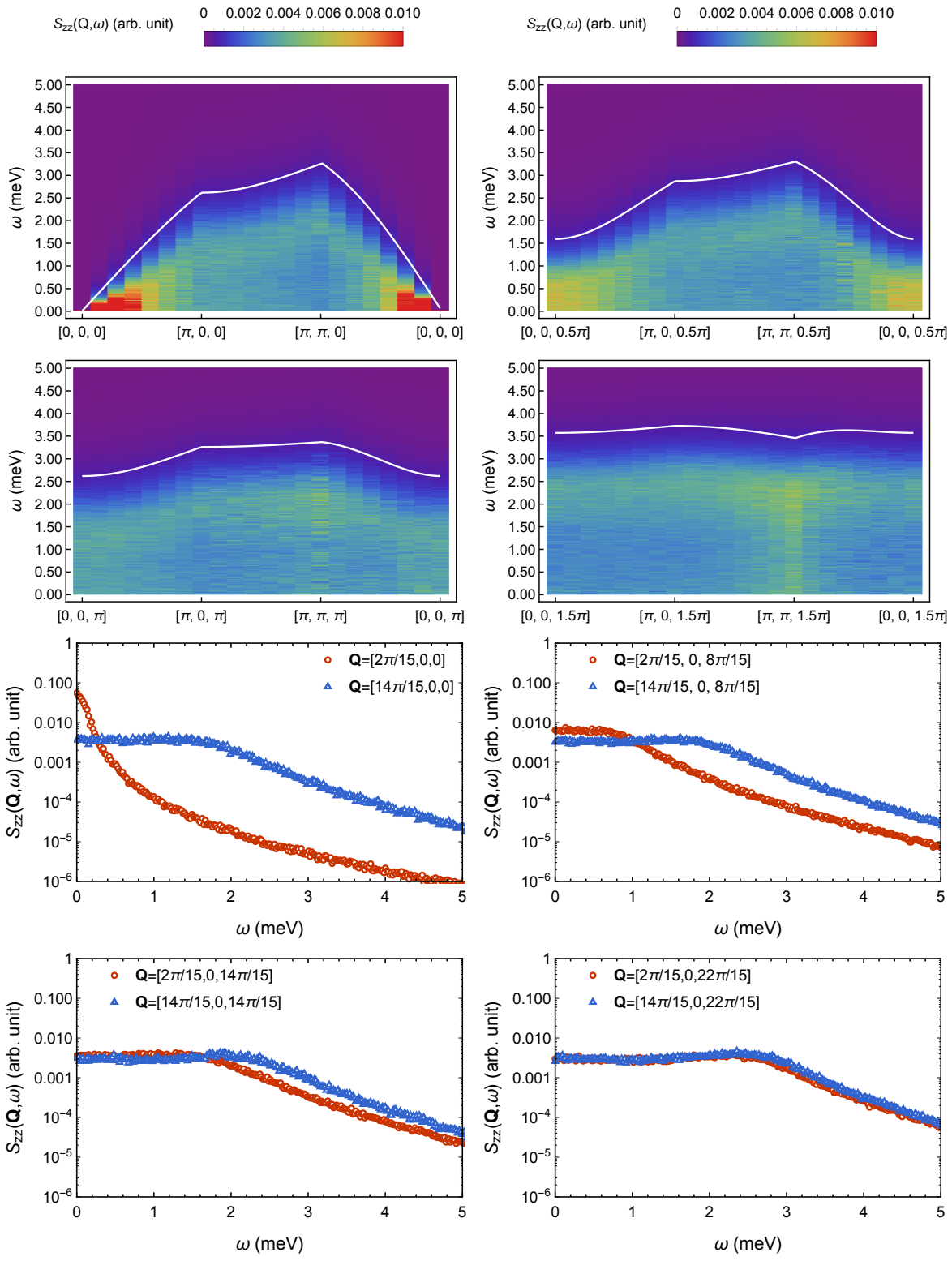

Figure 4.6: The dynamical structure factor of the diamond-lattice system at 24K.

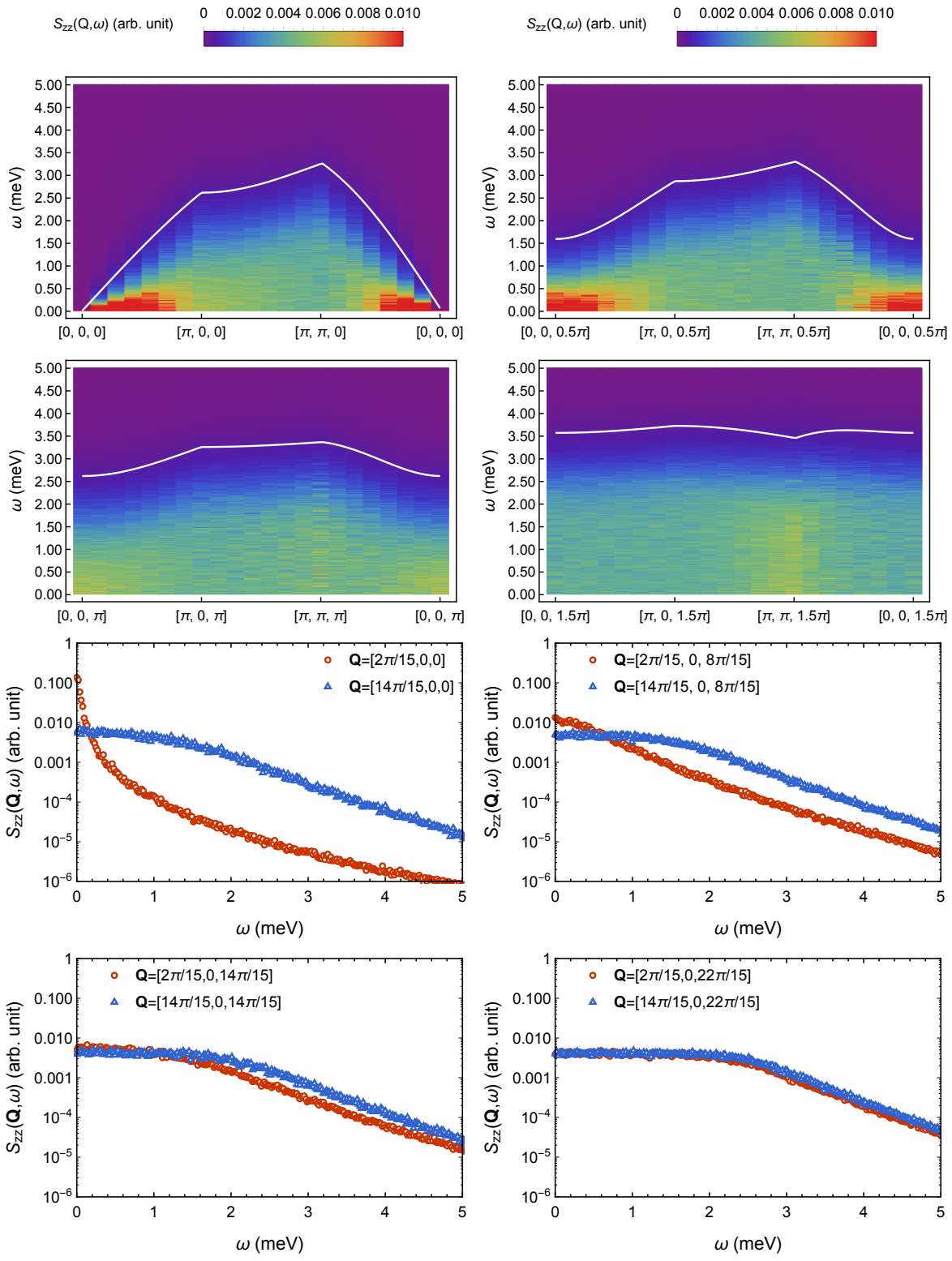

Figure 4.7: The dynamical structure factor of the diamond-lattec system at 30K.

CHAPTER 5

OUTLOOK

In this thesis, I present detailed single-crystal inelastic neutron-scattering studies of two important materials, the canonical frustrated pyrochlore-lattice compound $MgCr_2O_4$ and the triangular-lattice Ising magnet FeI_2. In $MgCr_2O_4$, we understood the nature of the continuous excitations in the cooperative paramagnetic regime. The next topic that I hope to study is the excitation in the low-temperature ordered state. Due to spin-lattice coupling, $MgCr_2O_4$ undergoes a structural distortion around 12 K and one multi-k or multiple single-k magnetic structures are selected from the degenerate manifold. The spectral weight is lifted from zero to finite energy. Multiple overlapping spin-wave bands clump in a small bandwidth, which leads people to consider a series of elaborate phenomenological spin-cluster models [26]. I hope to improve our understanding of the complex spectra by build a microscopic model. This will certainly be a very challenging task, since both the crystal and magnetic structure in the ordered phase are not fully determined. However, with our accurate paramagnetic model, we might be able to provide some unique insight into this issue. In FeI_2, we understood the nature of the "quadrupolar" excitation band. The next topic that I plan to study is the effect of magnetic field. Our theory collaborators predict based on our anisotropic exchange model that there will be new magnon decay channels involving the single-ion magnon bound state, appearing at low field. Early neutron diffraction work reveals four distinct phases emerging under medium and high fields [77]. These phases are result of delicate balance of exchange and applied field. We have planed two neutron-scattering experiments to thoroughly investigate all of these aspects in the near future.

The next new topic that I would like to study is excitations in honeycomb-lattice compound $NaMnCl_3$. The 2D honeycomb ferromagnets has attracted a lot of attention for

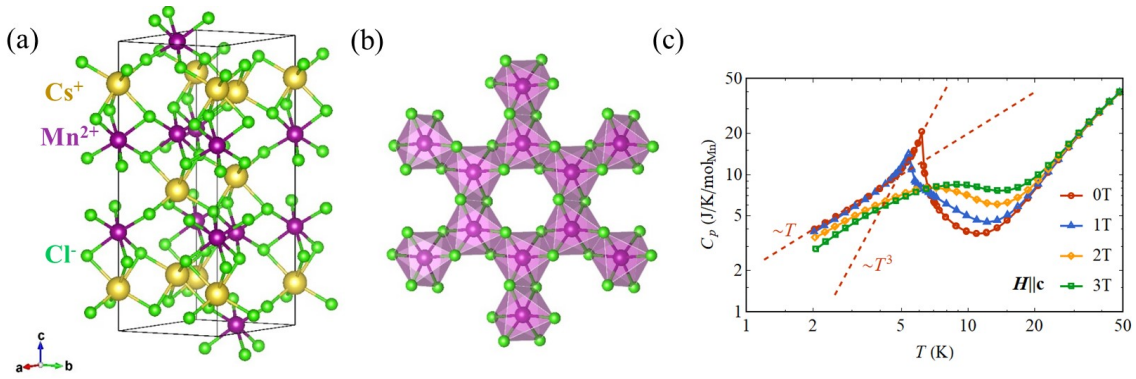

Figure 5.1: (a) The crystal structure of $NaMnCl_3$. (b) Honeycomb layer of Mn^{2+} (purple spheres) mediated through chloride atoms (green spheres). (c) Temperature dependence of heat capacity at selected fields. The dashed lines indicate possible scaling behaviors of the heat capacity data.

its potential of realizing magnon bands with non-trivial topology [119]. A recent theory work [120] shows spin-wave interactions give rise to a different renormalization behavior to the bare magnon band near Dirac crossing comparing to the fermionic counterpart, qualitatively account for the anomalies in neutron scattering data of honeycomb ferromagnet $CrBr_3$ from 1970s [121]. Below 6.5 K, $NaMnCl_3$ realizes a ferromagnetic ordering in the honeycomb plane with moments lying in the plane and a $\mathbf{k} = (0, 0, 3/2)$ stacking pattern along c-axis [122], in contrast to $CrBr_3$, CrI_3 [123] and $CrSiTe_3$ [124] where a simple ferromagnetic ordering along c-axis occurs. The complex magnetic ordering of $NaMnCl_3$ brings interesting behavior of heat capacity after the transition as shown in Figure 5.1, where a 2D ferromagnetic T-linear behavior [125] quickly supersedes 3D antiferro T-cubic scaling as temperature is lowered. It is very interesting to ask what microscopic interactions create the easy-plane anisotropy in the ordered phase and stabilize the complex 3D stacking.

REFERENCES

[1] P. W. Anderson, "More is different", Science **177**, 393–396 (1972).

[2] S. R. White, "Density matrix formulation for quantum renormalization groups", Physical review letters **69**, 2863 (1992).

[3] S. R. White, "Density-matrix algorithms for quantum renormalization groups", Physical Review B **48**, 10345 (1993).

[4] A. Belsky, M. Hellenbrandt, V. L. Karen, and P. Luksch, "New developments in the inorganic crystal structure database (icsd): accessibility in support of materials research and design", Acta Crystallographica Section B: Structural Science **58**, 364–369 (2002).

[5] S. Koohpayeh, D Fort, A Bradshaw, and J. Abell, "Thermal characterization of an optical floating zone furnace: a direct link with controllable growth parameters", Journal of Crystal Growth **311**, 2513–2518 (2009).

[6] J. Rodríguez-Carvajal, "Recent advances in magnetic structure determination by neutron powder diffraction", Physica B: Condensed Matter **192**, 55–69 (1993).

[7] M. Enderle, "Neutrons and magnetism", École thématique de la Société Française de la Neutronique **13**, 01002 (2014).

[8] M Enderle, M Kenzelmann, and W. Buyers, "Early experimental evidence of a topological quantum state: the signature of the haldane ground state revealed by scattered neutrons", arXiv preprint arXiv:1711.03862 (2017).

[9] J. Luttinger and L Tisza, "Theory of dipole interaction in crystals", Physical Review **70**, 954 (1946).

[10] S Toth and B Lake, "Linear spin wave theory for single-q incommensurate magnetic structures", Journal of Physics: Condensed Matter **27**, 166002 (2015).

[11] J. A. M. Paddison and A. L. Goodwin, "Empirical magnetic structure solution of frustrated spin systems", Phys. Rev. Lett. **108**, 017204 (2012).

[12] P. Conlon and J. Chalker, "Absent pinch points and emergent clusters: further neighbor interactions in the pyrochlore heisenberg antiferromagnet", Physical Review B **81**, 224413 (2010).

[13] J. N. Reimers, "Absence of long-range order in a three-dimensional geometrically frustrated antiferromagnet", Phys. Rev. B **45**, 7287–7294 (1992).

[14] R. Moessner and J. T. Chalker, "Properties of a classical spin liquid: the heisenberg pyrochlore antiferromagnet", Phys. Rev. Lett. **80**, 2929–2932 (1998).

[15] C. L. Henley, "The "coulomb phase" in frustrated systems", Annu. Rev. Condens. Matter Phys. **1**, 179–210 (2010).

[16] S. T. Bramwell and M. J. P. Gingras, "Spin ice state in frustrated magnetic pyrochlore materials", Science **294**, 1495–1501 (2001).

[17] T. Fennell, P. P. Deen, A. R. Wildes, K. Schmalzl, D. Prabhakaran, A. T. Boothroyd, R. J. Aldus, D. F. McMorrow, and S. T. Bramwell, "Magnetic coulomb phase in the spin ice ho2ti2o7", Science **326**, 415–417 (2009).

[18] D. J. P. Morris, D. A. Tennant, S. A. Grigera, B. Klemke, C. Castelnovo, R. Moessner, C. Czternasty, M. Meissner, K. C. Rule, J.-U. Hoffmann, K. Kiefer, S. Gerischer, D. Slobinsky, and R. S. Perry, "Dirac strings and magnetic monopoles in the spin ice dy2ti2o7", Science **326**, 411–414 (2009).

[19] J. W. Krizan and R. J. Cava, "Nacaco2f7: a single-crystal high-temperature pyrochlore antiferromagnet", Phys. Rev. B **89**, 214401 (2014).

[20] K. A. Ross, J. W. Krizan, J. A. Rodriguez-Rivera, R. J. Cava, and C. L. Broholm, "Static and dynamic xy-like short-range order in a frustrated magnet with exchange disorder", Phys. Rev. B **93**, 014433 (2016).

[21] K. W. Plumb, H. J. Changlani, A. Scheie, S. Zhang, J. W. Krizan, J. A. Rodriguez-Rivera, Y. Qiu, B. Winn, R. J. Cava, and C. L. Broholm, "Continuum of quantum fluctuations in a three-dimensional s = 1 heisenberg magnet", Nature Physics **15**, 54–59 (2019).

[22] J. H. Chung, M. Matsuda, S. H. Lee, K. Kakurai, H. Ueda, T. J. Sato, H. Takagi, K. P. Hong, and S. Park, "Statics and dynamics of incommensurate spin order in a geometrically frustrated antiferromagnet CdCr2O4", Phys. Rev. Letters **95**, 247204 (2005).

[23] S. H. Lee, C. Broholm, W. Ratcliff, G. Gasparovic, Q. Huang, T. H. Kim, and S. W. Cheong, "Emergent excitations in a geometrically frustrated magnet", Nature **418**, 856–858 (2002).

[24] H. Suzuki and Y. Tsunoda, "Spinel-type frustrated system MgCr2O4 studied by neutron scattering and magnetization measurements", J. Phys. Chem. Solids **68**, 2060–2063 (2007).

[25] K. Tomiyasu, H. Suzuki, M. Toki, S. Itoh, M. Matsuura, N. Aso, and K. Yamada, "Molecular spin resonance in the geometrically frustrated magnet mgcr2o4 by inelastic neutron scattering", Phys. Rev. Lett. **101**, 177401 (2008).

[26] K. Tomiyasu, T. Yokobori, Y. Kousaka, R. I. Bewley, T. Guidi, T. Watanabe, J. Akimitsu, and K. Yamada, "Emergence of highly degenerate excited states in the frustrated magnet mgcr2o4", Phys. Rev. Lett. **110**, 077205 (2013).

[27] G Blasse and J. Fast, "Néel temperatures of some antiferromagnetic oxides with spinel structure", Philips Research Reports **18**, 393–399 (1963).

[28] T Rudolf, C. Kant, F Mayr, J Hemberger, V Tsurkan, and A Loidl, "Spin-phonon coupling in antiferromagnetic chromium spinels", New J. Phys. **9**, 76 (2007).

[29] S. E. Dutton, Q. Huang, O. Tchernyshyov, C. L. Broholm, and R. J. Cava, "Sensitivity of the magnetic properties of the zncr2o4 and mgcr2o4 spinels to nonstoichiometry", Phys. Rev. B **83**, 064407 (2011).

[30] S. Koohpayeh, J.-J. Wen, M. Mourigal, S. Dutton, R. Cava, C. Broholm, and T. McQueen, "Optical floating zone crystal growth and magnetic properties of mgcr2o4", J. Cryst. Growth **384**, 39 –43 (2013).

[31] R. Moessner and A. J. Berlinsky, "Magnetic susceptibility of diluted pyrochlore and srcr(9-9x)ga(3+9x)o19 antiferromagnets", Phys. Rev. Lett. **83**, 3293–3296 (1999).

[32] S. Gao, K. Guratinder, U. Stuhr, J. S. White, M. Mansson, B. Roessli, T. Fennell, V. Tsurkan, A. Loidl, M. Ciomaga Hatnean, G. Balakrishnan, S. Raymond, L. Chapon, V. O. Garlea, A. T. Savici, A. Cervellino, A. Bombardi, D. Chernyshov, C. Rüegg, J. T. Haraldsen, and O. Zaharko, "Manifolds of magnetic ordered states and excitations in the almost heisenberg pyrochlore antiferromagnet mgcr2o4", Phys. Rev. B **97**, 134430 (2018).

[33] S. Klemme, H. S. C. O'Neill, W. Schnelle, and E. Gmelin, "The heat capacity of mgcr2o4, fecr2o4, and cr2o3 at low temperatures and derived thermodynamic properties", Am. Mineral. **85**, 1686–1693 (2000).

[34] H. Ehrenberg, M. Knapp, C. Baehtz, and S. Klemme, "Tetragonal low-temperature phase of MgCr[sub 2]O[sub 4]", Powder Diffr. **17**, 230 (2002).

[35] L Ortega-San-Martín, A. J. Williams, C. D. Gordon, S Klemme, and J. P. Attfield, "Low temperature neutron diffraction study of MgCr ₂ O ₄ spinel", J. Phys.: Condens. Matter **20**, 104238 (2008).

[36] M. C. Kemei, P. T. Barton, S. L. Moffitt, M. W. Gaultois, J. A. Kurzman, R. Seshadri, M. R. Suchomel, and Y.-I. Kim, "Crystal structures of spin-jahn–teller-

ordered mgcr2o4 and zncr2o4", Journal of Physics: Condensed Matter **25**, 326001 (2013).

[37] H. J. Xiang, E. J. Kan, S.-H. Wei, M.-H. Whangbo, and X. G. Gong, "Predicting the spin-lattice order of frustrated systems from first principles", Phys. Rev. B **84**, 224429 (2011).

[38] O. Tchernyshyov, R. Moessner, and S. L. Sondhi, "Order by distortion and string modes in pyrochlore antiferromagnets", Phys. Rev. Lett. **88**, 067203 (2002).

[39] G. J. Nilsen, Y. Okamoto, T. Masuda, J. Rodriguez-Carvajal, H. Mutka, T. Hansen, and Z. Hiroi, "Complex magnetostructural order in the frustrated spinel liincr4o8", Phys. Rev. B **91**, 174435 (2015).

[40] H. Shaked, J. M. Hastings, and L. M. Corliss, "Magnetic structure of magnesium chromite", Phys. Rev. B **1**, 3116–3124 (1970).

[41] G. E. Granroth, A. I. Kolesnikov, T. E. Sherline, J. P. Clancy, K. A. Ross, J. P. C. Ruff, B. D. Gaulin, and S. E. Nagler, "Sequoia: a newly operating chopper spectrometer at the sns", J. Phys.: Conf. Series **251**, 012058 (2010).

[42] M. B. Stone, J. L. Niedziela, D. L. Abernathy, L. DeBeer-Schmitt, G. Ehlers, O. Garlea, G. E. Granroth, M. Graves-Brook, A. I. Kolesnikov, A. Podlesnyak, and B. Winn, "A comparison of four direct geometry time-of-flight spectrometers at the spallation neutron source", Rev. Sci. Instrum. **85**, 045113, – (2014).

[43] O. Arnold, J.-C. Bilheux, J. Borreguero, A. Buts, S. I. Campbell, L Chapon, M. Doucet, N Draper, R. F. Leal, M. Gigg, et al., "Mantid—data analysis and visualization package for neutron scattering and mu-sr experiments", Nucl. Instrum. Methods Phys. Res. A **764**, 156–166 (2014).

[44] R. Ewings, A Buts, M. Le, J van Duijn, I Bustinduy, and T. Perring, "Horace: software for the analysis of data from single crystal spectroscopy experiments at time-of-flight neutron instruments", Nucl. Instrum. Methods Phys. Res. A **834**, 132–142 (2016).

[45] G. Xu, Z. Xu, and J. M. Tranquada, "Absolute cross-section normalization of magnetic neutron scattering data", Rev. Sci. Instrum. **84**, 083906, 083906 (2013).

[46] R. L. McGreevy and L. Pusztai, "Reverse monte carlo simulation: a new technique for the determination of disordered structures", Mol. Simul. **1**, 359–367 (1988).

[47] J. A. M. Paddison, M. J. Gutmann, J. R. Stewart, M. G. Tucker, M. T. Dove, D. A. Keen, and A. L. Goodwin, "Magnetic structure of paramagnetic mno", Phys. Rev. B **97**, 014429 (2018).

[48] P. C. Hohenberg and W. F. Brinkman, "Sum rules for the frequency spectrum of linear magnetic chains", Phys. Rev. B **10**, 128–131 (1974).

[49] M. B. Stone, I. Zaliznyak, D. H. Reich, and C. Broholm, "Frustration-induced two-dimensional quantum disordered phase in piperazinium hexachlorodicuprate", Phys. Rev. B **64**, 144405 (2001).

[50] P. H. Conlon and J. T. Chalker, "Absent pinch points and emergent clusters: further neighbor interactions in the pyrochlore heisenberg antiferromagnet", Phys. Rev. B **81**, 224413 (2010).

[51] G.-W. Chern, R Moessner, and O Tchernyshyov, "Partial order from disorder in a classical pyrochlore antiferromagnet", Phys. Rev. B **78**, 144418 (2008).

[52] A. Yaresko, "Electronic band structure and exchange coupling constants in a cr 2 x 4 spinels (a= zn, cd, hg; x= o, s, se)", Phys. Rev. B **77**, 115106 (2008).

[53] P. H. Conlon and J. T. Chalker, "Spin dynamics in pyrochlore heisenberg antiferromagnets", Phys. Rev. Lett. **102**, 237206 (2009).

[54] D. Bergman, J. Alicea, E. Gull, S. Trebst, and L. Balents, "Order-by-disorder and spiral spin-liquid in frustrated diamond-lattice antiferromagnets", Nat. Phys. **3**, 487–491 (2007).

[55] S. Gao, O. Zaharko, V. Tsurkan, Y. Su, J. S. White, G. Tucker, B. Roessli, F. Bourdarot, R. Sibille, D. Chernyshov, T. Fennell, A. Loidl, and C. Rüegg, "Spiral spin-liquid and the emergence of a vortex-like state in mnsc2s4", Nat. Phys. **13**, 157–161 (2016).

[56] J. A. M. Paddison, M. Daum, Z. Dun, G. Ehlers, Y. Liu, M. B. Stone, H. Zhou, and M. Mourigal, "Continuous excitations of the triangular-lattice quantum spin liquid ybmggao4", Nat. Phys. **13**, 117–122 (2017).

[57] L. R. Walker and R. E. Walstedt, "Computer model of metallic spin-glasses", Phys. Rev. Lett. **38**, 514–518 (1977).

[58] L. R. Walker and R. E. Walstedt, "Computer model of metallic spin-glasses", Phys. Rev. B **22**, 3816–3842 (1980).

[59] D Petitgrand and P Meyer, "Far infrared antiferromagnetic resonance in fecl2, febr2 and fei2", Journal de Physique **37**, 1417–1422 (1976).

[60] A. Fert, D Bertrand, J Leotin, J. Ousset, J Magariño, and J Tuchendler, "Excitation of two spin deviations by far infrared absorption in fei2", Solid State Communications **26**, 693–696 (1978).

[61] D Petitgrand, A Brun, and P Meyer, "Magnetic field dependence of spin waves and two magnon bound states in fei2", Journal of Magnetism and Magnetic Materials **15**, 381–382 (1980).

[62] R. Silberglitt and J. B. Torrance Jr, "Effect of single-ion anisotropy on two-spin-wave bound state in a heisenberg ferromagnet", Physical Review B **2**, 772 (1970).

[63] I. Ono, S. Mikado, and T. Oguchi, "Two-magnon bound states in a linear heisenberg chain with nearest and next nearest neighbor interactions", Journal of the Physical Society of Japan **30**, 358–366 (1971).

[64] T. Oguchi, "Theory of two-magnon bound states in the heisenberg ferro-and antiferromagnet", Journal of the Physical Society of Japan **31**, 394–402 (1971).

[65] D Petitgrand, B Hennion, and C Escribe, "Neutron inelastic scattering from magnetic excitations of fei2", Journal of Magnetism and Magnetic Materials **14**, 275–276 (1979).

[66] K Katsumata, M Hagiwara, M Tokunaga, and H Yamaguchi, "Observation of single-ion magnon bound states in the metamagnet fei2", Journal of Applied Physics **87**, 5085–5087 (2000).

[67] K Katsumata, H Yamaguchi, M Hagiwara, M Tokunaga, H.-J. Mikeska, P Goy, and M Gross, "Single-ion magnon bound states in an antiferromagnet with strong uniaxial anisotropy", Physical Review B **61**, 11632 (2000).

[68] D. Lockwood, G Mischler, and A Zwick, "Raman scattering from magnons, electronic excitations and phonons in antiferromagnetic fei2", Journal of Physics: Condensed Matter **6**, 6515 (1994).

[69] T. Fujita, A. Ito, and K. Ôno, "The mössbauer study of the ferrous ion in fei2", Journal of the Physical Society of Japan **21**, 1734–1736 (1966).

[70] U Balucani and A Stasch, "Hybrid excitations in layered iron halides", Physical Review B **32**, 182 (1985).

[71] Y. Bertrand, A. Fert, and J Gelard, "Susceptibilité magnétique des halogénures ferreux fecl2, febr2, fel2", Journal de Physique **35**, 385–391 (1974).

[72] C. Coleman and E Yamada, "Optimization of the vapor reaction growth of single crystal fei2", Journal of crystal growth **132**, 129–133 (1993).

[73] G. Granroth, A. Kolesnikov, T. Sherline, J. Clancy, K. Ross, J. Ruff, B. Gaulin, and S. Nagler, "Sequoia: a newly operating chopper spectrometer at the sns", in Journal of physics: conference series, Vol. 251, 1 (IOP Publishing, 2010), p. 012058.

[74] M. B. Stone, J. L. Niedziela, D. L. Abernathy, L DeBeer-Schmitt, G Ehlers, O Garlea, G. Granroth, M Graves-Brook, A. I. Kolesnikov, A Podlesnyak, et al., "A comparison of four direct geometry time-of-flight spectrometers at the spallation neutron source", Review of Scientific Instruments **85**, 045113 (2014).

[75] J. Trooster and W de Valk, "Spin ordering in febr2 and fei2. evidence for first order phase transition in fei2", Hyperfine Interactions **4**, 457–459 (1978).

[76] J Gelard, A. Fert, P Meriel, and Y Allain, "Magnetic structure of fei2 by neutron diffraction experiments", Solid State Communications **14**, 187–189 (1974).

[77] A Wiedenmann, L. Regnault, P Burlet, J Rossat-Mignod, O Koundé, and D Billerey, "A neutron scattering investigation of the magnetic phase diagram of fei2", Journal of magnetism and magnetic materials **74**, 7–21 (1988).

[78] J. Friedt, J. Sanchez, and G. Shenoy, "Electronic and magnetic properties of metal diiodides mi2 (m= v, cr, mn, fe, co, ni, and cd) from 129i mössbauer spectroscopy", The Journal of Chemical Physics **65**, 5093–5102 (1976).

[79] E. Wollan, W. Koehler, and M. Wilkinson, "Neutron diffraction study of the magnetic properties of mnbr2", Physical Review **110**, 638 (1958).

[80] A. Fert, J Gelard, and P Carrara, "Phase transitions of fel2 in high magnetic field parallel to the spin direction, static field up to 150 koe, pulsed field up to 250 koe", Solid State Communications **13**, 1219–1223 (1973).

[81] A Wiedenmann, L. Regnault, P Burlet, J Rossat-Mignod, O Kounde, and D Billerey, "Magnetic phase diagram of fei2", Physica B: Condensed Matter **156**, 305–307 (1989).

[82] Y. Tanaka and N. Uryû, "Ground state spin configurations of the triangular ising net with the nearest and next nearest neighbor interactions", Journal of the Physical Society of Japan **39**, 825–826 (1975).

[83] X Bai, J. Paddison, E Kapit, S. Koohpayeh, J.-J. Wen, S. Dutton, A. Savici, A. Kolesnikov, G. Granroth, C. Broholm, et al., "Magnetic excitations of the classical spin liquid mgcr 2 o 4", Physical review letters **122**, 097201 (2019).

[84] X. Wu, Y. Cai, Q. Xie, H. Weng, H. Fan, and J. Hu, "Magnetic ordering and multiferroicity in MnI 2", Physical Review B **86**, 1–9 (2012).

[85] R. A. Muniz, Y. Kato, and C. D. Batista, "Generalized spin-wave theory: application to the bilinear–biquadratic model", Progress of Theoretical and Experimental Physics **2014** (2014).

[86] J. A. Paddison, M. Daum, Z. Dun, G. Ehlers, Y. Liu, M. B. Stone, H. Zhou, and M. Mourigal, "Continuous excitations of the triangular-lattice quantum spin liquid ybmggao 4", Nature Physics **13**, 117 (2017).

[87] H. Yoshizawa, W. Kozukue, and K. Hirakawa, "Neutron scattering study of magnetic excitations in pseudo-one-dimensional singlet ground state ferromagnets csfecl3 and rbfecl3", Journal of the Physical Society of Japan **49**, 144–153 (1980).

[88] S. Hayashida, M. Matsumoto, M. Hagihala, N. Kurita, H. Tanaka, S. Itoh, T. Hong, M. Soda, Y. Uwatoko, and T. Masuda, "Novel excitations near quantum criticality in geometrically frustrated antiferromagnet csfecl3", arXiv preprint arXiv:1908.08403 (2019).

[89] K Penc, J Romhányi, T Rõõm, U Nagel, Á Antal, T Fehér, A Jánossy, H Engelkamp, H Murakawa, Y Tokura, et al., "Spin-stretching modes in anisotropic magnets: spin-wave excitations in the multiferroic ba2coge2o7", Physical review letters **108**, 257203 (2012).

[90] M. Akaki, D. Yoshizawa, A. Okutani, T. Kida, J. Romhányi, K. Penc, and M. Hagiwara, "Direct observation of spin-quadrupolar excitations in sr2coge2o7 by high-field electron spin resonance", Physical Review B **96**, 214406 (2017).

[91] S. Zvyagin, C. Batista, J Krzystek, V. Zapf, M Jaime, A Paduan-Filho, and J Wosnitza, "Observation of two-magnon bound states in the spin-1 anisotropic heisenberg antiferromagnetic chain system nicl2-4sc(nh2)2", Physica B: Condensed Matter **403**, 1497–1499 (2008).

[92] M. I. Aroyo, J. Perez-Mato, D Orobengoa, E Tasci, G De La Flor, and A Kirov, "Crystallography online: bilbao crystallographic server", Bulg. Chem. Commun **43**, 183–197 (2011).

[93] K. Plumb, H. J. Changlani, A Scheie, S. Zhang, J. Krizan, J. Rodriguez-Rivera, Y. Qiu, B Winn, R. J. Cava, and C. Broholm, "Continuum of quantum fluctuations in a three-dimensional s= 1 heisenberg magnet", Nature Physics **15**, 54 (2019).

[94] S. G. Johnson, *The nlopt nonlinear-optimization package*, 2008–2019.

[95] J. A. Nelder and R. Mead, "A simplex method for function minimization", The computer journal **7**, 308–313 (1965).

[96] M. Krech, A. Bunker, and D. Landau, "Fast spin dynamics algorithms for classical spin systems", Computer Physics Communications **111**, 1–13 (1998).

[97] A. Keren, "Dynamical simulation of spins on kagomé and square lattices", Physical review letters **72**, 3254 (1994).

[98] A. Keren, "Simulation of spin dynamics on kagomé and square lattices", Journal of magnetism and magnetic materials **140**, 1493–1494 (1995).

[99] R Moessner and J. Chalker, "Properties of a classical spin liquid: the heisenberg pyrochlore antiferromagnet", Physical review letters **80**, 2929 (1998).

[100] R Moessner and J. Chalker, "Low-temperature properties of classical geometrically frustrated antiferromagnets", Physical Review B **58**, 12049 (1998).

[101] P. Conlon and J. Chalker, "Spin dynamics in pyrochlore heisenberg antiferromagnets", Physical review letters **102**, 237206 (2009).

[102] K. Chen and D. Landau, "Spin-dynamics study of the dynamic critical behavior of the three-dimensional classical heisenberg ferromagnet", Physical Review B **49**, 3266 (1994).

[103] A. Bunker, K. Chen, and D. Landau, "Critical dynamics of the body-centered-cubic classical heisenberg antiferromagnet", Physical Review B **54**, 9259 (1996).

[104] H. G. Evertz and D. Landau, "Critical dynamics in the two-dimensional classical xy model: a spin-dynamics study", Physical Review B **54**, 12302 (1996).

[105] D. Rapaport and D. Landau, "Critical dynamics of a dynamical version of the classical heisenberg model", Physical Review E **53**, 4696 (1996).

[106] B. Costa, J. Costa, and D. Landau, "Monte carlo and spin dynamics study of the anisotropic heisenberg model in two dimensions", Journal of applied physics **81**, 5746–5748 (1997).

[107] J. Frank, W. Huang, and B. Leimkuhler, "Geometric integrators for classical spin systems", Journal of Computational Physics **133**, 160–172 (1997).

[108] M. Sofroniou and W. Oevel, "Sympletic runge–kutta shemes i: order conditions", SIAM journal on numerical analysis **34**, 2063–2086 (1997).

[109] A. Dullweber, B. Leimkuhler, and R. McLachlan, "Symplectic splitting methods for rigid body molecular dynamics", The Journal of chemical physics **107**, 5840–5851 (1997).

[110] I. P. Omelyan, "Algorithm for numerical integration of the rigid-body equations of motion", Physical Review E **58**, 1169 (1998).

[111] I. Omelyan, I. Mryglod, and R Folk, "Conservation-laws-preserving algorithms for spin dynamics simulations", EPL (Europhysics Letters) **52**, 603 (2000).

[112] I. Omelyan, I. Mryglod, and R Folk, "Algorithm for molecular dynamics simulations of spin liquids", Physical review letters **86**, 898 (2001).

[113] I. Omelyan, I. Mryglod, and R. Folk, "Optimized forest–ruth-and suzuki-like algorithms for integration of motion in many-body systems", Computer Physics Communications **146**, 188–202 (2002).

[114] R. Steinigeweg and H.-J. Schmidt, "Symplectic integrators for classical spin systems", Computer physics communications **174**, 853–861 (2006).

[115] M. Krech and D. Landau, "Spin-dynamics simulations of the three-dimensional XY model: Structure factor and transport properties", Physical Review B **60**, 3375–3387 (1999).

[116] X. Leoncini, A. D. Verga, and S. Ruffo, "Hamiltonian Dynamics and the Phase Transition of the XY Model", Physical Review E **57**, 6377 (1998).

[117] R. Loft and T. DeGrand, "Numerical simulation of dynamics in the XY model", Physical Review B **35**, 8528–8541 (1987).

[118] L Ge, J Flynn, J. A. Paddison, M. B. Stone, S Calder, M. Subramanian, A. Ramirez, and M Mourigal, "Spin order and dynamics in the diamond-lattice heisenberg antiferromagnets curh 2 o 4 and corh 2 o 4", Physical Review B **96**, 064413 (2017).

[119] S. Owerre, "A first theoretical realization of honeycomb topological magnon insulator", Journal of Physics: Condensed Matter **28**, 386001 (2016).

[120] S. S. Pershoguba, S. Banerjee, J. Lashley, J. Park, H. Ågren, G. Aeppli, and A. V. Balatsky, "Dirac magnons in honeycomb ferromagnets", Physical Review X **8**, 011010 (2018).

[121] W. Yelon and R. Silberglitt, "Renormalization of large-wave-vector magnons in ferromagnetic cr br 3 studied by inelastic neutron scattering: spin-wave correlation effects", Physical Review B **4**, 2280 (1971).

[122] N Fedoseeva, I Spevakova, G Petrakovskii, V Chuev, and S Petrov, "Magnetic structure and magnetic field behaviour of namncl3", Journal of Magnetism and Magnetic Materials **15**, 539–541 (1980).

[123] L. Chen, J.-H. Chung, B. Gao, T. Chen, M. B. Stone, A. I. Kolesnikov, Q. Huang, and P. Dai, "Topological spin excitations in honeycomb ferromagnet cri 3", Physical Review X **8**, 041028 (2018).

[124] T. J. Williams, A. A. Aczel, M. D. Lumsden, S. E. Nagler, M. B. Stone, J.-Q. Yan, and D. Mandrus, "Magnetic correlations in the quasi-two-dimensional semiconducting ferromagnet crsite 3", Physical Review B **92**, 144404 (2015).

[125] A. Cracknell and A. Tooke, "The specific heats of magnetically-ordered materials", Contemporary Physics **20**, 55–82 (1979).